SEMICONDUCTOR HYPERBOLIC METAMATERIALS

FOR THE INFRARED

by

Dongxia Wei

A dissertation submitted to the Faculty of the University of Delaware in partial fulfillment of the requirements for the degree of Doctor of Philosophy in Materials Science and Engineering

Fall 2019

SEMICONDUCTOR HYPERBOLIC METAMATERIALS

FOR THE INFRARED

by

Dongxia Wei

Approved: _____
Darrin Pochan, Ph.D.
Chair of the Department of Materials Science and Engineering

Approved: _____
Levi Thompson, Ph.D.
Dean of the College of Engineering

Approved: _____
Douglas J. Doren, Ph.D.
Interim Vice Provost for Graduate and Professional Education and Dean of the Graduate College

I certify that I have read this dissertation and that in my opinion it meets the academic and professional standard required by the University as a dissertation for the degree of Doctor of Philosophy.

Signed: _____

Stephanie Law, Ph.D.
Professor in charge of dissertation

I certify that I have read this dissertation and that in my opinion it meets the academic and professional standard required by the University as a dissertation for the degree of Doctor of Philosophy.

Signed: _____

Joshua Zide, Ph.D.
Member of dissertation committee

I certify that I have read this dissertation and that in my opinion it meets the academic and professional standard required by the University as a dissertation for the degree of Doctor of Philosophy.

Signed: _____

Matthew Doty, Ph.D.
Member of dissertation committee

I certify that I have read this dissertation and that in my opinion it meets the academic and professional standard required by the University as a dissertation for the degree of Doctor of Philosophy.

Signed: _____

Tingyi Gu, Ph.D.
Member of dissertation committee

ACKNOWLEDGMENTS

First, and most of all, I would like to express my sincere gratitude to my advisor Professor Stephanie Law for the continuous support of my Ph.D. research and dissertation. Professor Law is knowledgeable, diligent, dedicated and responsive. She is always happy to answer our questions and give us help in time. I learned a lot from Professor Law about how to tackle a scientific problem, which is invaluable for my future career development. I am so glad that I got the chance to work in her group.

I would like to extend my gratitude to the rest of my thesis committee: Professor Joshua M. O. Zide, Professor Matthew F. Doty, and Professor Tingyi Gu. They provided insightful suggestions and comments for my research project and dissertation.

I would like to thank all my collaborators: Christian Harris, Stephanie Tomasulo, and Michael Yakes. Without you, I wouldn't have been able to complete these amazing projects.

I am deeply grateful to the help of my colleagues who worked on MBE system with me: Patrick Sohr, Yuejing Wang, Lauren McCabe, James Bork, Jing Zhang, Cory Bomberger, and Pernell Dongmo. Together as a team, we overcame many difficulties in maintaining and repairing the MBE systems. I had such a wonderful time working with all of you.

I would also like to thank the other Law group members: Theresa Ginley, Yong Wang, ZhengTianYe Wang, Vishnu Mambakkam, Greeshma Chandan, Saadia

Nasir, Md Nazmul Alam, and Desalegn Debu. In the past few years, you gave me lots of help and valuable suggestions.

Besides research, I made lots of friends at the University of Delaware through different activities. We have lots of enjoyable memories together. I will never forget the happiness and encouragement you brought to me.

Finally, and most importantly, huge thanks to my parents and my dog who gave me spirit support for the last five years.

TABLE OF CONTENTS

LIST OF TABLES

LIST OF FIGURES

ABSTRACT

Light is one of the most important media to transport information. Optical metamaterials are artificial materials that are fabricated on the subwavelength scale so people can manipulate light-matter interactions in a fascinating way that conventional materials are not able to. Optical metamaterials have unique optical properties and may find applications in subwavelength imaging, novel waveguiding, thermal emission engineering, and biosensing,

Multilayer hyperbolic metamaterial (HMM) is one kind of optical metamaterials that are composed of alternating metal/dielectric layers. They are easy to fabricate and have designer properties. Though there are extensive studies about HMM in the visible range, the potential of HMM in the infrared remains to be fully discovered. To move HMM study to the infrared, we first need to choose suitable materials. III-V semiconductors, such as InAs, have been proven to be promising plasmonic materials for the infrared.

This dissertation demonstrates semiconductor HMMs created from various material classes: Si:InAs/InAs, Si:InGaAs/InAlAs, and Si:InAs/AlSb. Discontinuity of the Brewster angle and negative refraction, two hallmarks of HMM, were observed in our materials. Also, the properties of semiconductor HMM are designer by adjusting the structure parameters.

This dissertation also explores the volume plasmon polariton (VPP) modes in semiconductor HMMs. VPP modes are modes with large wavevectors and are usually not supported by conventional materials. They are the foundation of many proposed

applications based on HMMs. Up to five VPP modes were observed in our materials, and we found that Si:InAs/AlSb HMM exhibits the best VPP modes among all other semiconductor HMMs.

We also investigated the optimization of the growth of highly Si-doped InAs by using bismuth surfactant. We show that the optical properties, electrical properties and surface morphology of Si:InAs were significantly improved. The growth window of Si:InAs is broadened, making it easier to integrate Si:InAs with other III-V semiconductors.

In the future, III-V semiconductor HMMs will be integrated with other semiconductor structures, including quantum wells, quantum dot, and quantum cascade laser. Such compound structures will lead to new physical phenomena and novel optoelectronic devices with higher efficiency.

Chapter 1

BACKGROUND OF SEMICONDUCTOR HYPERBOLIC METAMATERIALS

1.1 Introduction to Optical Metamaterials

In recent years, optical metamaterials, a kind of newly emerging artificial materials, have attracted significant attention due to their huge potentials in manipulating light-matter interaction [1–5]. Potential applications of optical metamaterials include negative refraction [4,6–10], novel waveguiding [11–13], subwavelength imaging [14–17], nanoscale light confinement [18,19], spontaneous emission enhancement [20–24], and biosensing [25–27].

Optical metamaterials are electromagnetic metamaterials with engineered subwavelength building blocks so people can control the behavior of light, an important medium used to transport information. In conventional materials, the response to the electromagnetic waves depends on the atoms and the bonds in the materials. However, for optical metamaterials, the response is also determined by the subwavelength periodic structures (so-called “meta-atom”, Figure 1.1) [2]. The size and spacing of these “meta-atoms” are much smaller than the wavelength of the incident light, therefore the incident waves can not sense the microscopic structure of materials. Instead, the incident light responds to the average properties of the structure. Thus, optical metamaterials can have fascinating properties that usually would not be

observed in constituent material, providing us with unlimited routes to manipulate the light in theory [2,3,28–33].

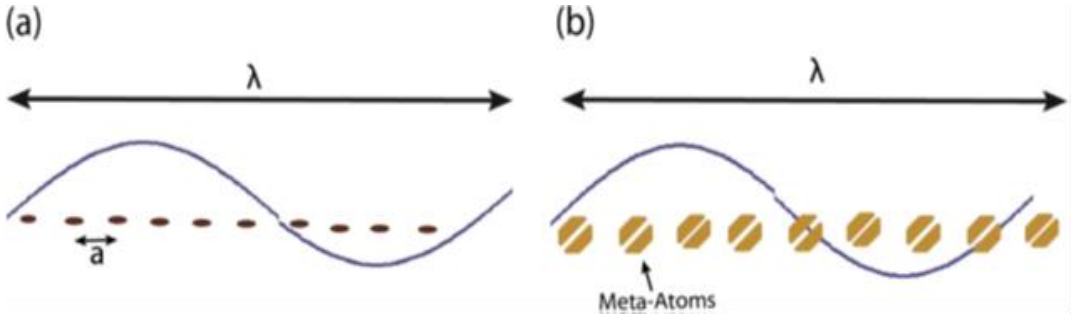

Figure 1.1: (a) A periodic array of atoms with the radius and inter-atomic spacing of each atom being much less than the wavelength of radiation. (b) Metamaterials are composed of nano-inclusions called meta-atoms with critical dimensions much less than the wavelength of radiation. The artificial meta-atoms provide unique electromagnetic responses not seen with natural structures [2]. Reprint permission obtained from Nano Convergence.

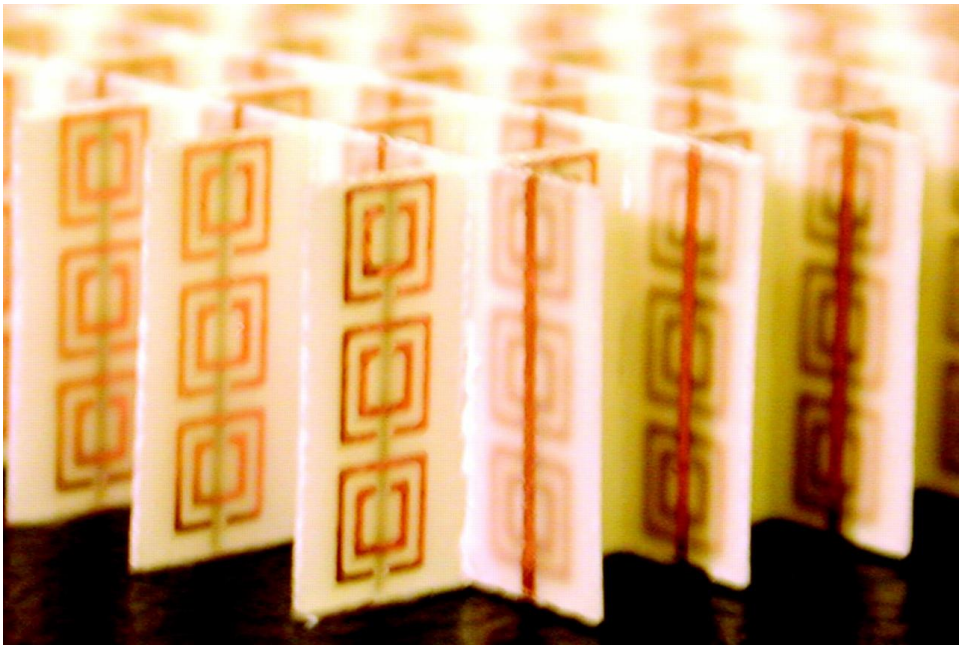

Figure 1.2: Photograph of the left-handed metamaterial (LHM) sample. The LHM sample consists of square copper split-ring resonators and copper wire strips on fiber glass circuit board material. The rings and wires are on opposite sides of the boards, and the boards have been cut and assembled into an interlocking lattice [34]. Reprint permission obtained from The American Association for the Advancement of Science.

Among the many exciting properties of optical metamaterials, negative refraction index attracts most attention due to its high potential for applications in sub-diffraction imaging, optical sensing, cloaking, superlens, and novel waveguiding. To realize the negative refraction index, the material is required to have simultaneously negative permittivity and permeability. Although the existence of such materials was first predicted by Veselago in the 1960s [35], it had been a long time for the realization of such materials with both negative permittivity, ε, and permeability, μ, in the same wavelength ranges. It is relatively easier to find materials with $\varepsilon < 0$ (for example, silver and gold in the infrared and visible range), so the critical challenge is to find materials

with $\mu < 0$ in the range we are interested in. However, the materials with negative refractive index have not been observed in nature due to the limitation imposed by natural materials' unit cells——atom or molecules. Fortunately, the advanced fabrication technologies today enable us to construct human-made "meta-atoms" which could display magnetic effects different from natural materials. By deliberately designing the unit cell (or so-called "meta-atom") of metamaterials, we can control the values of its permittivity, ε, and permeability, μ, to achieve negative refraction index. One of the important structures to attain magnetic response is split-ring resonators (SRRs) which were first suggested by J.B. Pendry et al. in 1999 [36]. In 2000, D.R. Smith et al. first demonstrated such material experimentally [37]. Such structures have been used to fabricate optical metamaterials in the microwave, THz, and near-infrared range [34,37–44] (see Figure 1.2).

1.2 Hyperbolic Metamaterials

The structures described above achieve negative refraction through the overlapping of electric and magnetic resonances, resulting in a material with simultaneously negative permittivity and permeability. However, such double resonances are accompanied by high losses inside the structures which can limit their practical applications. Also, it is challenging for existing fabrication technologies to scale down the feature size of such devices to achieve shorter wavelength ranges. It requires sub-100nm resolution when we deal with optical metamaterials working in infrared or visible ranges. To overcome these limitations, hyperbolic metamaterials(HMM) were proposed [45,46]. HMMs are subwavelength structures that have hyperbolic dispersion. They are easy to fabricate using existing nanofabrication technique. HMMs are nonmagnetic (μ=1) and thus do not require

double resonances to achieve negative refraction. Instead, HMM creates negative refraction through another important optical property: anisotropy (Figure 1.3). As a result, HMMs have a low optical loss due to single resonance [2,47,48].

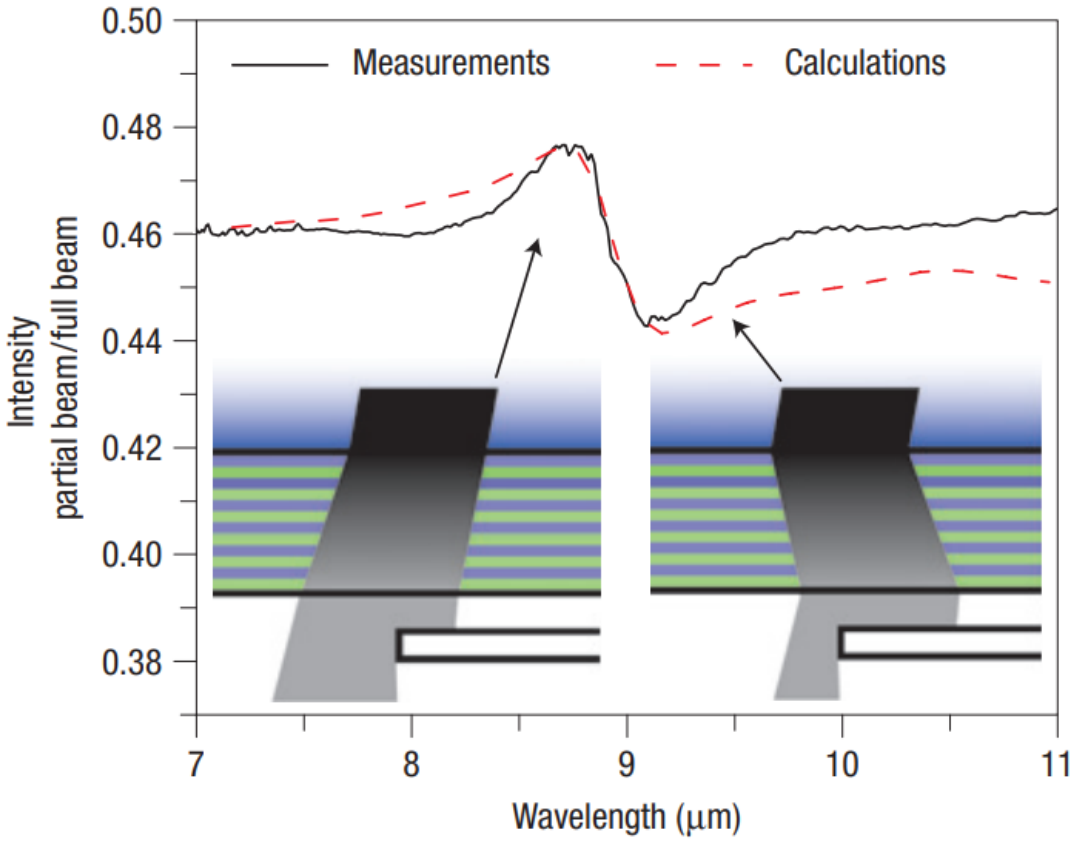

Figure 1.3: Experiment demonstration of negative refraction in HMM [7]. Reprint permission obtained from Springer Nature.

1.2.1 Principle of Hyperbolic Metamaterials

HMMs are uniaxial materials with extreme anisotropy. The permittivity tensors of HMM can be described by the following equation:

$$\hat{\varepsilon} = \begin{pmatrix} \varepsilon_{\parallel} & 0 & 0 \\ 0 & \varepsilon_{\parallel} & 0 \\ 0 & 0 & \varepsilon_{\perp} \end{pmatrix} \qquad \text{(Equation 1.1)}$$

here $\varepsilon_{\parallel}$ is dielectric constant normal to the anisotropic axis and $\varepsilon_{\perp}$ is parallel to the anisotropic axis. For HMM, $\varepsilon_{\parallel}$ and $\varepsilon_{\perp}$ satisfy $\varepsilon_{\parallel} \times \varepsilon_{\parallel} < 0$. For ordinary waves, the electric field is in the (y,z) plane (see Figure 1.4). Thus, the propagation of such waves will not be affected by anisotropy. The propagation of extraordinary waves with a magnetic field in the (y,z) plane will be affected by both $\varepsilon_{\perp}$ and $\varepsilon_{\parallel}$.

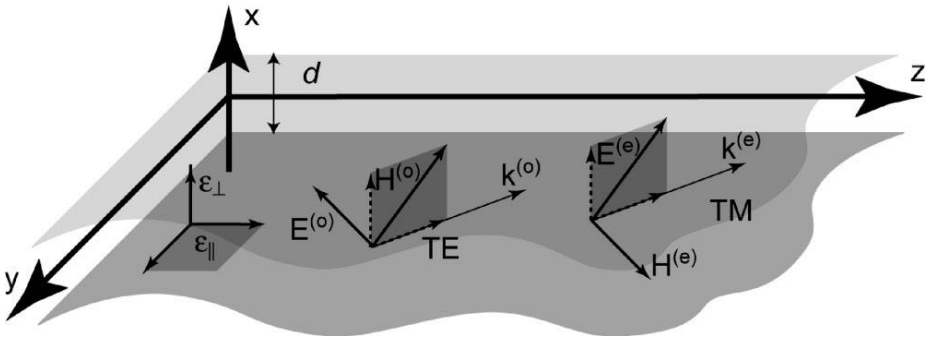

Figure 1.4: The extraordinary TM and ordinary TE waves propagating in a planar waveguide with an anisotropic core [46]. Reprint permission obtained from Physical Review B.

If the signs of $\varepsilon_{\perp}$ and $\varepsilon_{\parallel}$ are in opposition to each other, the isofrequency surface of extraordinary waves (TM waves) has a hyperbolic dispersion:

$$\frac{k_x^2+k_y^2}{\varepsilon_{\parallel}} + \frac{k_z^2}{\varepsilon_{\perp}} = \left(\frac{\omega}{c}\right)^2 \qquad \text{(Equation 1.2)}$$

Here k_x, k_y and k_z are wavevector components, ω is the wave frequency and c is the speed of light in free space. There are two types of metamaterials: type I metamaterials with $\varepsilon_{\perp} < 0$ and $\varepsilon_{\parallel} > 0$ and type II metamaterials with $\varepsilon_{\perp} > 0$ and $\varepsilon_{\parallel} < 0$. Figure

1.5 plots the isofrequency surface of normal isotropic material, type I HMMs and type II HMMs.

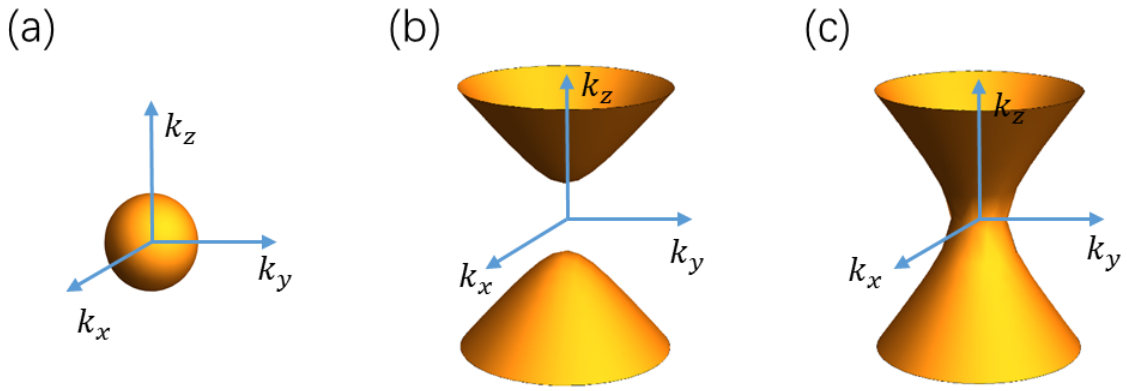

Figure 1.5: (a) Normal isotropic materials; (b) Type I HMMs: $\varepsilon_{\perp} < 0, \varepsilon_{\parallel} > 0$; (c) Type II HMMs: $\varepsilon_{\perp} > 0, \varepsilon_{\parallel} < 0$.

Compared to the closed spherical isofrequency surfaces of isotropic media, the unbounded isofrequency surface of HMMs results in the propagation of high-k waves which would decay exponentially in isotropic media. These high-k waves are important because they carry essential information on the subwavelength structure (see Chapter 4 for more details). This property enables the application of HMMs in many areas, such as enhanced sensitivity detection, optical sensing, thermal emission engineering, and subwavelength imaging. Also, the energy flow exhibits negative refraction when light is incident from normal materials to an HMM since energy flow has to be normal to the isofrequency surface (see Section 3.6 for more details). Thus, the HMM could realize negative refraction with only nonmagnetic materials. In

addition, hyperbolic dispersion also leads to a high photonic density of states, which can be used for radiative decay engineering.

1.2.2 Realization of Hyperbolic Metamaterials

1.2.2.1 Natural Hyperbolic Metamaterials

Some natural materials exhibit hyperbolic dispersion in their original forms [49–53]. In [54], Leonid V. Alekseyev *et al.* discuss the realization of negative refraction in the THz and far-infrared domains using sapphire, bismuth, and triglycine sulfate. Lisa V. Brown demonstrated hyperbolic modes in hexagonal boron nitride [53]. Moritz Esslinger *et al.* found hyperbolic behavior in Be_2Se_3 and Be_2Te_3 in the near-infrared to visible spectrum [55]. However, these natural materials have fixed properties and only exhibit hyperbolic dispersion for a particular spectrum [49,50]. Also, the bandwidth of natural HMMs is narrow. For practical applications, we need HMMs with a more flexible and broader operational wavelength.

1.2.2.2 Artificial Hyperbolic Metamaterials

To obtain a hyperbolic dispersion, the permittivity needs to be negative in one or two directions while positive in other directions. A structure with a combination of metal and dielectric could be the right candidate since metals have negative permittivity below plasma frequency and dielectrics have positive permittivity. There are two common ways to create artificial HMMs: multilayered metal/dielectric HMMs (Figure 1.6 (a)) and nanowire HMMs with metal rods embedded in a dielectric matrix (Figure 1.6 (b)). This dissertation will only focus on multilayer HMMs, which are easy

to grow using techniques like molecular beam epitaxy and require no additional fabrication process except initial growth.

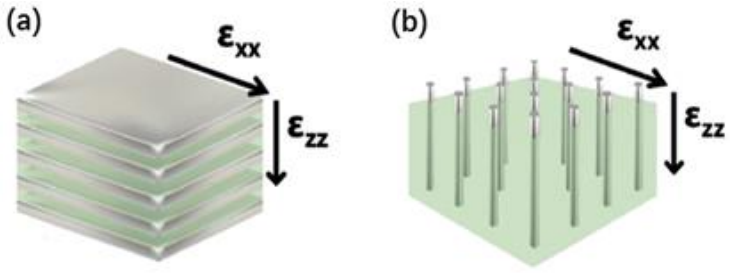

Figure 1.6: (a) Multilayer structure consisting of alternating metallic and dielectric layers forming a metal-dielectric superlattice. (b) Nanowire structure consisting of metallic nanorods embedded in a dielectric host. In both (a) and (b) the constituent components are subwavelength allowing characterization with effective medium theory [2]. Reprint permission obtained from Nano Convergence.

We can use the transfer matrix method combined with the effective medium theory (EMT) to calculate the permittivity of a multilayer structure [56–59]. The idea of EMT is using a single value to describe the macroscopic properties of composite materials [60–62]. According to EMT, we can use an effective $\varepsilon_{\parallel}$ and an effective $\varepsilon_{\perp}$ to describe the properties of a multilayer structure when the subwavelength structure is much smaller than the incident light (see Figure 3.1). The equations for $\varepsilon_{\parallel}$ and $\varepsilon_{\perp}$ are given by:

$$\varepsilon_{\parallel} = \frac{\varepsilon_m + \eta\varepsilon_d}{1+\eta} \qquad \text{(Equation 1.3)}$$

$$\varepsilon_{\perp} = \frac{1+\eta}{\frac{1}{\varepsilon_m} + \frac{1}{\varepsilon_d}} \qquad \text{(Equation 1.4)}$$

where ε_m and ε_d are the dielectric constants of the metal and the dielectric, respectively. η is the ratio of their thicknesses (η=t_d/t_m).

Equation 1.3 and 1.4 can be derived from the boundary conditions: the tangential components of the electric field ($E_\parallel$) and the normal components of the electric displacement ($D_\perp$) must be continuous:

$$E_{\parallel,m} = E_{\parallel,d} \quad \text{(Equation 1.5)}$$

$$D_{\perp,m} = D_{\perp,d} \quad \text{(Equation 1.6)}$$

In the parallel direction,

$$D_{\parallel,m} = \varepsilon_m E_{\parallel,m} \quad \text{(Equation 1.7)}$$

$$D_{\parallel,d} = \varepsilon_d E_{\parallel,d} \quad \text{(Equation 1.8)}$$

$$E_{\parallel,m} = E_{\parallel,d} \quad \text{(Equation 1.9)}$$

The average electric displacement is:

$$\begin{aligned} D_\parallel &= \rho D_{\parallel,m} + (1-\rho) D_{\parallel,d} \\ &= \rho \varepsilon_m E_{\parallel,m} + (1-\rho) \varepsilon_d E_{\parallel,d} \\ &= (\rho \varepsilon_m + (1-\rho)\, \varepsilon_d) E_\parallel \end{aligned} \quad \text{(Equation 1.10)}$$

Where ρ = t_m / (t_m+t_d) = 1 / (η+1). The effective parallel permittivity is:

$$\varepsilon_\parallel = \rho \varepsilon_m + (1-\rho) \varepsilon_d \quad \text{(Equation 1.11)}$$

In the perpendicular direction,

$$D_{\perp,m} = \varepsilon_m E_{\perp,m} \quad \text{(Equation 1.12)}$$

$$D_{\perp,d} = \varepsilon_d E_{\perp,d} \quad \text{(Equation 1.13)}$$

$$D_{\perp,m} = D_{\perp,d} \quad \text{(Equation 1.14)}$$

The average electric field is

$$E_\perp = \rho E_{\perp,m} + (1-\rho) E_{\perp,d} \quad \text{(Equation 1.15)}$$

$$= \rho \frac{D_{\perp,m}}{\varepsilon_m} + (1-\rho) \frac{D_{\perp,d}}{\varepsilon_d} \qquad \text{(Equation 1.16)}$$

The effective perpendicular permittivity is

$$\varepsilon_\perp = \frac{\rho}{\varepsilon_m} + \frac{1-\rho}{\varepsilon_d} \qquad \text{(Equation 1.17)}$$

Replacing ρ with $\frac{1}{\eta+1}$, we arrive at the Equation 1.4.

From equation 1.3 and 1.4 we can see that by adjusting the η and choosing the appropriate materials, we can create HMMs working on a wide range of wavelengths. At the high-frequency region, traditional metals like silver, gold, and dielectrics like SiO_2 are good choices due to their low optical losses. However, when we move to infrared, these materials are not suitable because of the extremely large negative permittivity of the metals and strong absorption resonances of traditional dielectrics. Better alternative materials are doped semiconductors (see Section 1.3).

1.2.3 Applications of Hyperbolic Metamaterials

HMMs feature unique optical properties and a high photonic density of states. These characteristics enable many applications based on HMMs.

A critical application of HMM is subwavelength imaging [63]. Traditional optical microscopes are limited by the diffraction limit, resulting in a resolution around half wavelength of the incident light. This is due to the decay of large wavevectors that carry fine structural information of objects. As a result, only small wavevectors contribute to the final images.

HMMs surmount the diffraction limit by supporting the propagation of large wavevectors. Figure 1.7 (a) and (b) explain the design for using HMM for subwavelength imaging. When an object is brought to the near-field of the HMMs, the evanescent waves can propagate across the HMM and transmit subwavelength information to the other side of HMM. However, in this design, the evanescent waves

will still decay outside the HMM (Figure 1.7 (a)). Hyperlens overcome this drawback by curving the HMM into a cylindrical structure (Figure 1.7 (b)) [15]. Due to the conservation of angular momentum:

$$m = k_\theta r \qquad \text{(Equation 1.18)}$$

the wavevector (k_θ) will decrease in magnitude when the light travels towards the edge of the cylinder, since the increase of radii (r). Zhaowei Liu and Hyesog Lee *et al.* realized this design experimentally in [64].

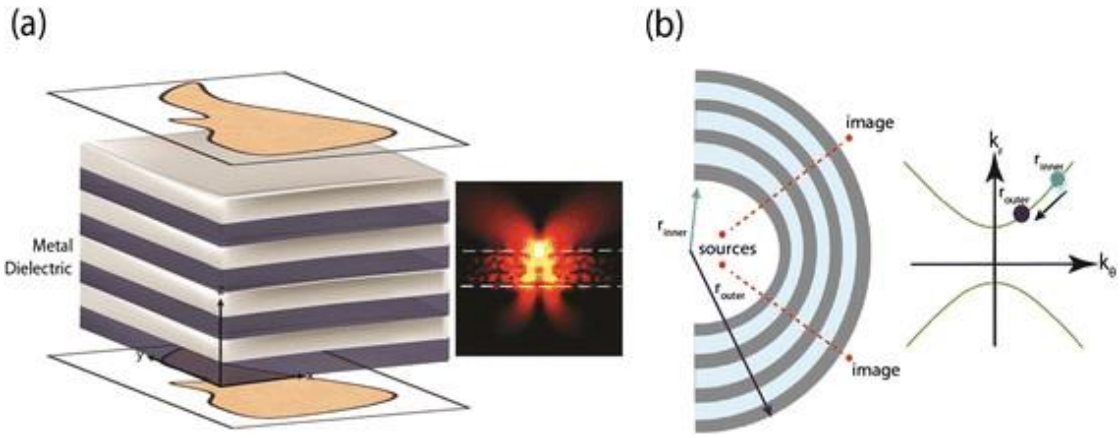

Figure 1.7: Subwavelength imaging with HMMs. (a) Multilayer HMM in the near field of an object allows normally evanescent waves to propagate and carry subwavelength features across the length of the structure. Inset: Point dipole placed in the near field of Type I HMM. The dipole radiates into sub-diffraction resonance cones in the HMM structure. The high-k waves are still evanescent outside of the multilayer HMM. (b) Hyperlens: Cylindrical HMM geometry allows for the tangential component of the wavevector times the radius to remain constant. The wavevectors decrease in magnitude as the high-k waves move to the edge of the structure. If the wavevector magnitudes are reduced sufficiently to allow propagation in vacuum, the hyperlens can carry subwavelength features to the far-field [2]. Reprint permission obtained from Nano Convergence

Another popular application of HMM is spontaneous emission enhancement. Spontaneous emission is a quantum effect. When an atom or a molecule is excited to a higher energy level state, it may spontaneously return to the ground state or other lower states, releasing a photon with energy determined by the difference between energy levels. The spontaneous emission rate can be modified by the surrounding environment. The Purcell factor describes the ratio between modified and free-space emission rates:

$$F_p = \frac{F_{mod}}{F_0} = \frac{3Q\lambda^3}{4\pi^2 V_0} \qquad \text{(Equation 1.19)}$$

where Q is the quality factor, λ is the incident light, and V_0 is the effective mode volume [65]. The above equation shows that the emission rate could be increased by confining light in a small volume (decrease V_0) [2]. Compared to other photonic structures, such as photonic crystals cavities that people used to achieve mode in a small volume, HMMs could realize enhanced spontaneous emission in a broader spectrum due to its high optical density of states in a continuous spectrum. As shown in Figure 1.8 (d), the calculated Purcell enhancement on a Ag-Si HMM is around six times of that on a Ag film at 600nm. The Purcell enhancement could also be engineered by changing the metal filling ratio (Figure 1.8 (e)), demonstrating the designer properties of HMM [22]. The Purcell effect enhancement has also been experimentally demonstrated in many other papers [22,66,67]. The enhancement of the Purcell factor could lead to applications in biosensing and efficient emitter devices.

Other applications of HMM such as negative refraction, strong coupling, and broadband absorption will be discussed in later chapters (Section 3.6, Section 4.1 and Section 6.2).

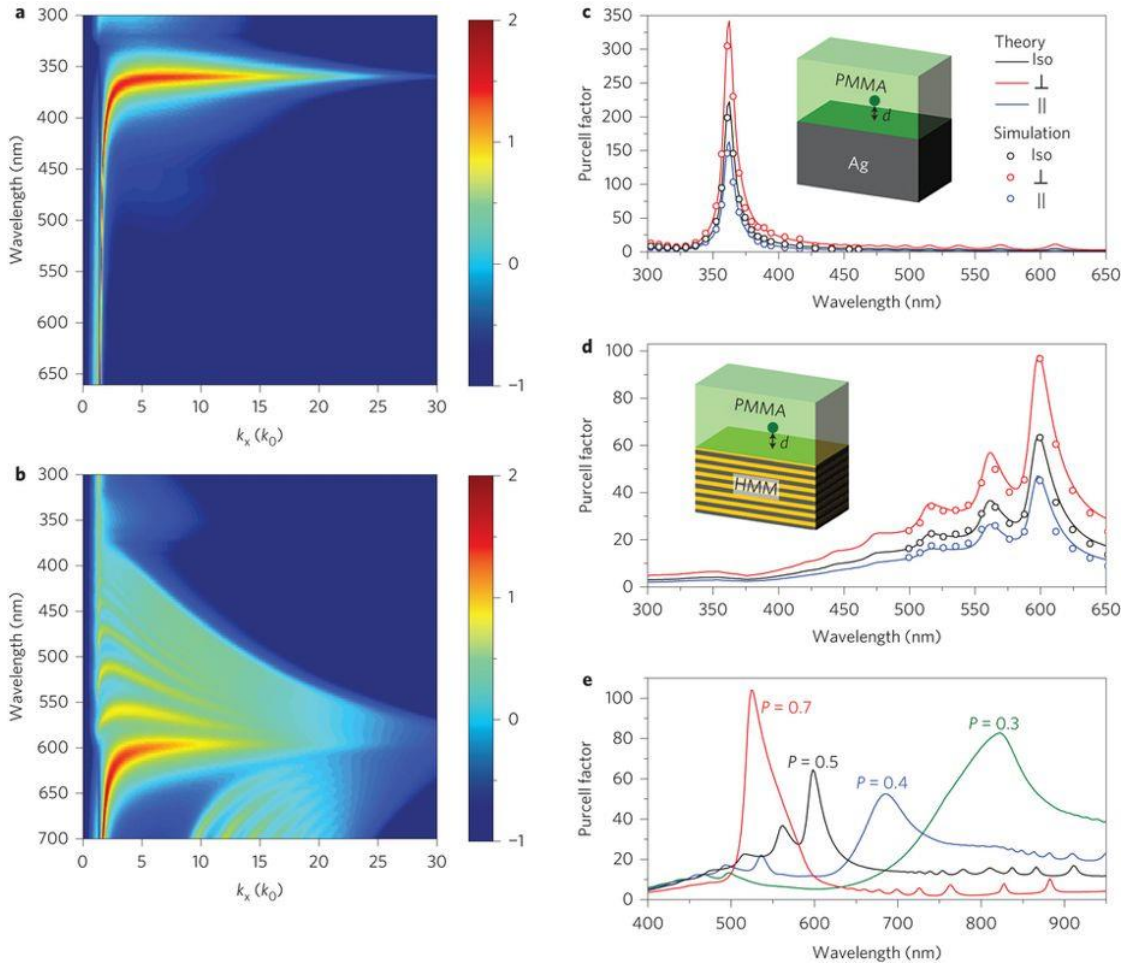

Figure 1.8: a,b, Normalized dissipated power spectra (intensity on a logarithmic scale) for a dipole perpendicular to and at a distance of d = 10 nm above a uniform Ag single layer (a) and a Ag–Si multilayer HMM (b), each with the same total thickness of 305 nm. The multilayer has 15 pairs of Ag and Si layers (each layer thickness, 10 nm). The color scales indicate normalized dissipated power. c,d, Purcell factor for a dipole located d = 10 nm above the uniform Ag single layer (c) and the Ag–Si multilayer HMM (d), as depicted in the insets. The Purcell factor for isotropic dipoles (iso, black lines) is averaged from that for the dipoles perpendicular (⊥, red lines) and parallel (‖, blue lines) to the surface. Corresponding three-dimensional full-wave simulations (open circles) agree with theoretical calculations. e, Tunable Purcell enhancement across the visible spectra for isotropic dipoles located d = 10 nm above the uniform Ag–Si HMMs by adjusting the volumetric filling ratio of the metal, P [22]. Reprint permission obtained from Nature Nanotechnology.

1.3 Highly Doped Semiconductors as Plasmonic Materials for the Infrared

1.3.1 Background of Infrared

Infrared is a technologically important wavelength range for many applications such as thermal imaging and optical sensing. The spectral range of infrared varies between disciplines and applications. This dissertation will focus on the wavelength range between 5μm to 30μm.

Infrared is home to vibrational absorption spectrums of many molecules. Each molecule has a unique absorption spectrum in the infrared, acting as a fingerprint to identify these molecules. Infrared spectroscopy is a widely used method to identify organic compounds and polymers. The ability to accurately detect these molecules makes infrared spectroscopy a powerful tool for various medical, environmental, biological, and industrial applications [68,69].

Thermal radiation from any finite temperature objects also belongs to infrared. There are extensive uses of thermal radiation in military and civilian applications. One of the most common applications is thermal imaging, which is widely used in security surveillance, building flaw detection, equipment maintenance, and crop health tracking. There are fundamental advantages of thermal imaging over traditional visible imaging solutions. First, they perform well in low-visibility situations. This is especially useful for security surveillance where equipment is frequently required to work in a dark environment. Second, thermal imaging can detect temperature differences. This is important for avoiding catastrophic equipment failure [70,71].

Significant efforts have been made to build efficient infrared devices. Unfortunately, devices for infrared so far are either of low efficiency or much more expensive than those for visible. As discussed in Section 1.2, HMMs provide unprecedented opportunities to create new efficient devices due to their unique properties. However, to take advantage of HMMs in infrared, we first need to find suitable materials.

Conventional materials such as gold, silver, Si and SiO_2, which are used to create HMM for visible, are not suitable for infrared. Gold and silver have large permittivities in infrared, and it is difficult to find dielectrics with comparable permittivities. Si and SiO_2 are not ideal either since they have strong absorptions in infrared [2]. In addition, the fixed properties of these materials limit their applications. In the next section, a new class of materials for infrared will be discussed.

1.3.2 Highly Doped Semiconductors as Plasmonic Materials

People have been using traditional metals and dielectrics to create HMMs for visible range and have achieved a lot of success [72–75]. In recent years, there is an increasing demand to move HMM research into the infrared. Unfortunately, traditional metals and dielectrics are not suitable for infrared as stated in Section 1.3.1.

It has been demonstrated that III-V semiconductors, including InAs and InSb, can be used as plasmonic materials for the infrared [76–81]. These materials have small effective mass, high mobilities, and low optical loss. Also, the plasma wavelength is designer by changing the doping density. We can use the Drude model to describe the optical properties of highly doped semiconductors [78,82]:

$$\varepsilon(\omega) = \varepsilon_s\left(1 - \frac{\omega_p^2}{\omega^2 + i\omega\Gamma}\right) \qquad \text{(Equation 1.20)}$$

$$\omega_p^2 = \frac{ne^2}{\varepsilon_s \varepsilon_0 m^*} \qquad \text{(Equation 1.21)}$$

where ε_s is the permittivity at high frequency, ε_0 is the permittivity of free space, ω_p is the plasma frequency, Γ is the scattering rate, m^* is the effective mass, n is the free carrier concentration. Below the plasma frequency, these semiconductors have negative permittivities and thus are good candidates for creating HMMs for infrared.

There are several advantages of doped III-V semiconductors over traditional metals. First, III-V semiconductors can be epitaxially grown by techniques such as molecular beam epitaxy, which offers high crystallinity, precise layer thickness control, and accurate doping concentration. Second, the plasma wavelength of III-V semiconductors is designer by engineering the doping density. This enables a broader working window compared to traditional materials whose properties are fixed. As shown in Figure 1.9 the shortest experimental plasma wavelength of Si:InAs so far is 5.5μm [9]. Third, doped III-V semiconductors offer potentials to be integrated with other cutting-edge III-V semiconductor electronic and optoelectronic devices including quantum wells, quantum dot, quantum cascade laser, and type-II superlattice infrared photodetectors.

The wavelength flexibility along with other advantages of doped III-V semiconductors make them excellent candidates for plasmonic materials in infrared, opening the door to a wide range of new optical structures including epsilon near zero (ENZ) materials and hyperbolic metamaterials [76–78].

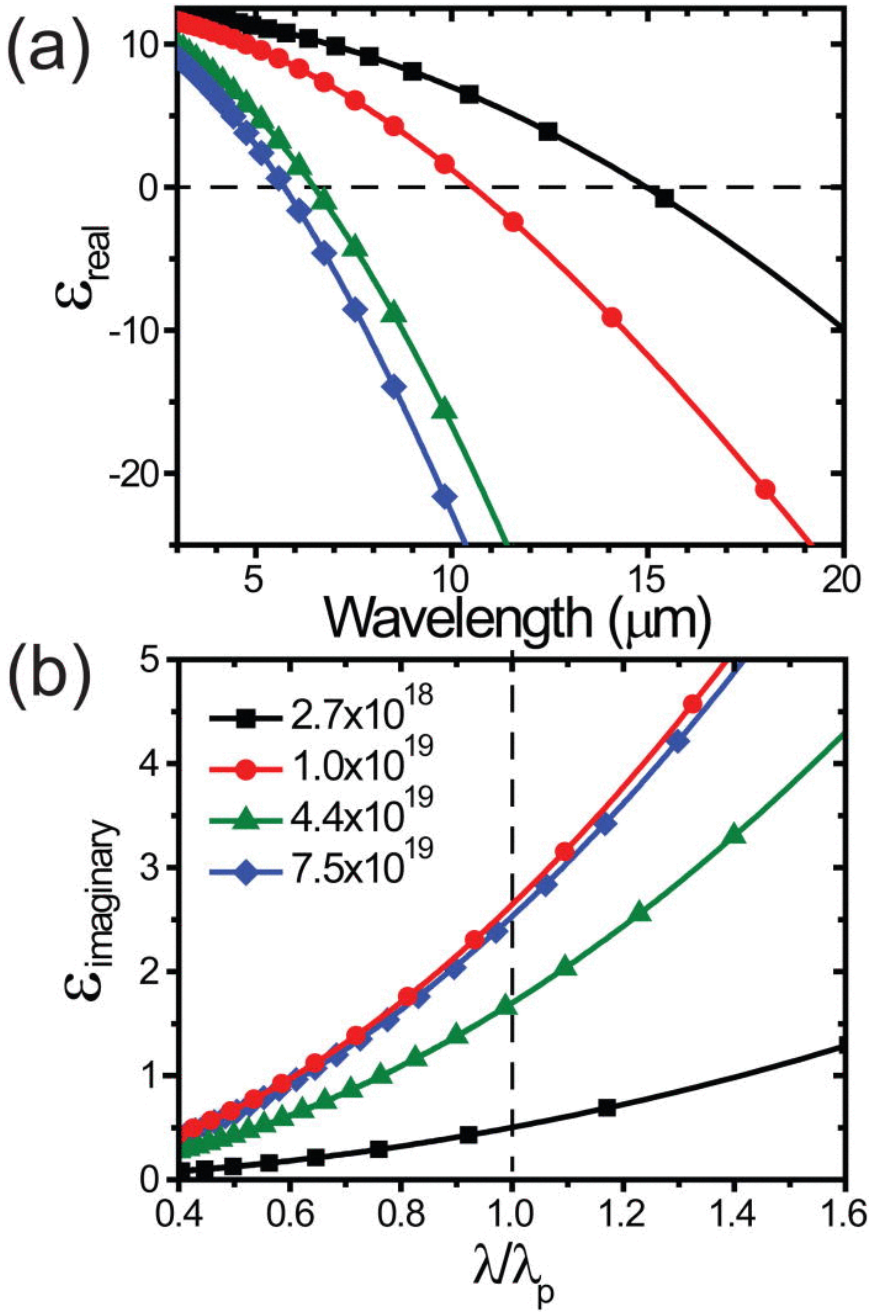

Figure 1.9: (Color online) Real (a) and imaginary (b) parts of the dielectric function for doped InAs films as a function of carrier concentration. All films are grown with no buffer layer, a growth rate of 0.75 μm/h, and a thickness of 1 μm [77]. Reprint permission obtained from AIP Publishing.

1.4 III-V Semiconductor Hyperbolic Metamaterials for Infrared

In Section 1.3, the importance of infrared and the potentials of doped III-V semiconductors for creating HMMs were discussed. Compared to other traditional metal/dielectric HMMs, III-V semiconductor HMM can be fabricated by epitaxial growth, enabling precise control over layer thickness, career density, and interface smoothness. One primary technique for epitaxial growth is molecular beam epitaxy, which allows us to grow semiconductors atomic layer by layer in an ultra-high vacuum environment (See Section 2.1 for more details). III-V semiconductors also have a lower optical loss in the infrared, which makes them ideal materials for creating HMM.

Until now, only a few papers studied the properties of III-V semiconductor HMMs. Here are some of the important ones. Anthony J.Hoffman *et al.* first implemented HMM using $In_{0.53}Ga_{0.47}As$ and $Al_{0.48}In_{0.52}As$ [7]. They demonstrated negative refraction and discontinuity of the Brewster angle, two hallmarks of HMMs. The operational wavelength ranges from 8.8μm to around 13μm. Anthony J.Hoffman's group at Notre Dame University also studied the applications of InGaAs/InAlAs HMMs as infrared resonators [18,83]. Prashant Shekhar and Zubin Jacob theoretically proved the strong coupling between semiconductor hyperbolic metamaterials and embedded quantum wells [84]. These papers present some exciting experimental results and theoretical studies on semiconductor HMMs. However, the potentials of semiconductor HMMs have not been fully discovered compared to other HMMs. A more systematic study about semiconductor HMM created from different materials is necessary. Besides InGaAs, InAs is also a good candidate for plasmonic materials due to its small effective mass and high mobilities (Section 1.3.2). Binary materials are also easier to grow compared to ternary materials. The following

chapters will cover the study of semiconductor HMMs created from different material classes including Si:InAs/InAs, Si:InGaAs/InAlAs and Si:InAs/AlSb.

1.5 Dissertation Outline

In this chapter, the concepts of optical metamaterials and HMMs are reviewed. HMM is a kind of optical metamaterials with novel optical properties and is easy to fabricate. It is important to extend the HMM study to the infrared to create more efficient devices. Doped III-V semiconductors are good candidates to create HMMs for the infrared due to their remarkable optical and electrical properties. The goal of the dissertation is to study the properties of III-V semiconductor HMMs for the infrared.

In Chapter 2, I will briefly introduce the techniques used to grow, fabricate, characterize, and simulate semiconductor HMMs. Molecular beam epitaxy is our major tool to grow samples. Characterization tools include Fourier transform infrared spectroscopy, Hall measurement, scanning electron microscopy, atomic force microscopy, optical microscope. COMSOL and nextnano were used to simulate the optical and electrical properties of samples. In Chapter 3, single material semiconductor HMMs based on InAs will be demonstrated. Reflection and transmission properties of samples with different structure parameters were studied by FTIR. Two hallmarks of HMM, discontinuity of the Brewster angle and negative refraction, were observed in our materials. Chapter 4 focuses on the experimental and theoretical study of volume plasmon polaritons of semiconductor HMMs created from various material classes including Si:InAs/InAs, Si:InGaAs/InAlAs and InAs/AlSb. The properties of VPP were systematically studied and compared between different material classes. Chapter 5 will investigate the optimized growth of Si:InAs using

bismuth surfactant. The optical properties, electrical properties and surface morphology of Si:InAs with various doping concentration and growth conditions will be discussed. Chapter 6 will cover the summary of the dissertation and some possible future work including strong coupling and rainbow trapping.

Chapter 2

GROWTH, FABRICATION, MODELING AND CHARACTERIZATION TECHNIQUES

2.1 Molecular Beam Epitaxy

The samples discussed in this dissertation were all grown by molecular beam epitaxy (MBE), an ultra-high vacuum technique allowing us to grow thin films atomic layer by layer. It provides us with excellent control over layer thickness as well as high crystallinity [85] [86]. MBE is a common technology for the growth of high-quality single-crystal III-V semiconductors including arsenides (InAs, GaAs, AlAs, *etc.*) [87,88], antimonides (GaSb, AlSb, InSb, *etc.*) [89] and nitrides (GaN, AlN, *etc.*) [90–92]. It is also widely used for the growth of group IV materials (Si, Ge) [93], II-VI topological insulators (Bi_2Se_3, Bi_2Te_3, *etc.*) [94], and semiconductor oxides [95,96]. The MBE we used at the University of Delaware is OSEMI NextGEN solid source MBE.

Figure 2.1 is a schematic of an MBE system. Major components of a standard MBE system include the substrate heater, effusion cells, water cooling system, cryopanels, beam flux monitor, reflection high energy electron diffraction (RHEED) system, ion gauges, residual gas analyzer, bandedge thermometry (BET) and pump systems (ion pump, cryopump, turbo pump, *etc.*).

Before the growth, source materials (As, In, Ga, Al, Sb, *etc.*) were heated separately in effusion cells. Depending on the vapor pressure we desire and the

distinct properties of each material, some materials could be heated to the liquid phase, such as In, Ga, Al, and Bi. Other materials, such as Si and As, are usually heated below the melting point for the growth. The As cell has two heating zones. The temperature of the sublimation heating zone controls the vapor pressure of As flux. We usually keep the sublimation heating zone at 400~410 ℃. The temperature of the cracking zone provides either As_2 (cracking zone temperature around 850 ℃) or As_4 (cracking zone temperature around 650 ℃). Throughout this dissertation, the samples were grown using As_2 with cracking zone temperature kept at 850 ℃. Similar to the As cell, the Sb cell also has two heating zones. The cracker zone breaks Sb_4 to Sb_2. We usually keep Sb cracking zone temperature at 910 ℃, 200 ℃ higher than the sublimation heating zone. During the growth, we close or open the shutters of different effusion cells to control the growth. When we open the shutter, the material vapor resides in the corresponding effusion cell will be able to move toward the heated substrate and interact with other elements to form the material we want. The chamber pressure of the MBE during growth is typically in the range between $1 \times 10^{-10} \sim 1 \times 10^{-7}$ Torr. Under such an ultra-high vacuum environment, the mean free path of the evaporated elements is much larger than the size of the chamber. This guarantees that the elements only react with each other to form a film when they reach the substrate.

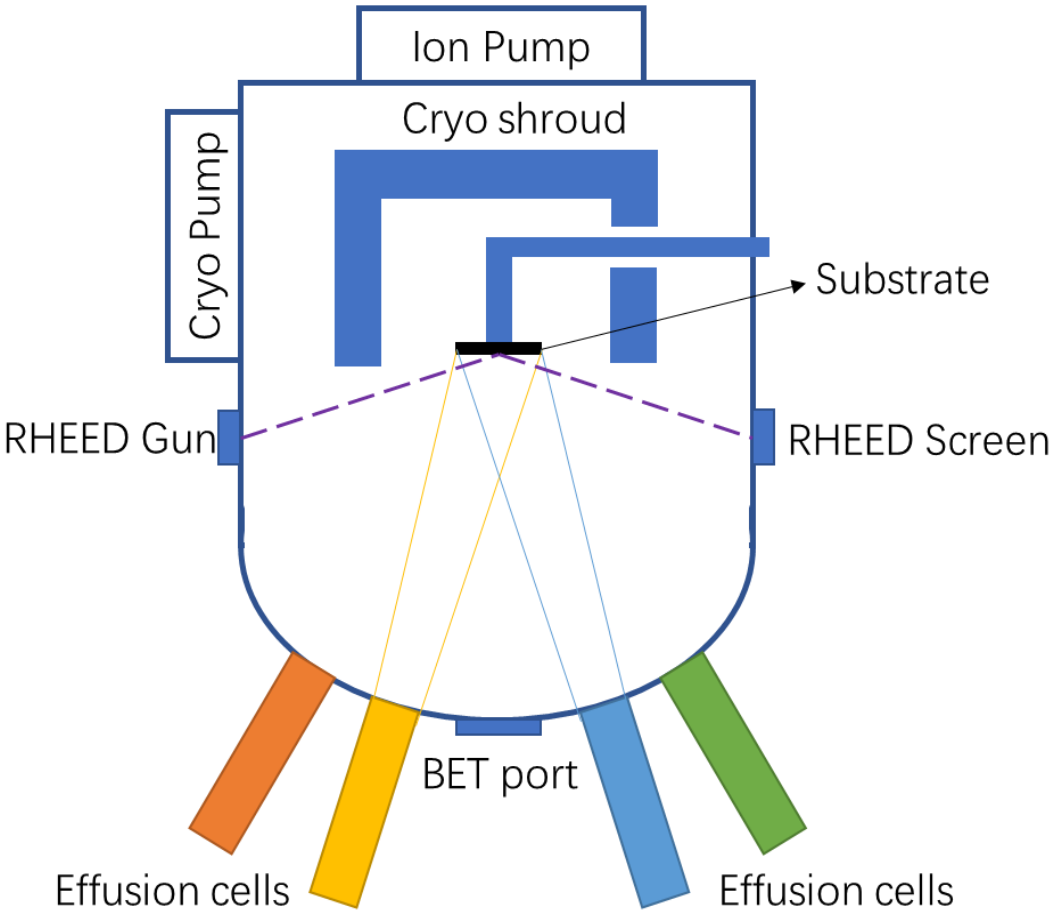

Figure 2.1: Simplified schematic of an MBE system.

We use multiple tools to optimize and control the growth conditions. First, a beam flux monitor (BFM) is used to measure the beam flux of each element. Instead of directly measuring the beam flux, the BFM measures the pressure of each element with an ionization gauge. We call this pressure as beam equivalent pressure (BEP). The BEP helps us control the growth rate since it is linearly proportional to the growth rate. Typically, we will grow a series of calibration films with different flux. Then we measured their thickness by X-ray diffraction, profilometer, or SEM to confirm the

growth rate. For doping elements such as Si and Be, the beam flux is too small to measure, so we calibrate the doping density by the temperature of the effusion cell, which is exponentially proportional to the doping level. To calibrate the Si cell, we grow a series of Si:InAs (or Si:GaAs) at different Si temperatures. Then, the doping density of each sample is measured using the Hall effect measurement assuming a 100% ionization rate.

Second, the growth temperature is monitored by a band edge thermometer (BET) during the growth. The bandgap of a semiconductor is a function of temperature T:

$$E_g(T) = E_g(0) - \frac{\alpha T^2}{T+\beta} \qquad \text{(Equation 2.1)}$$

Where $E_g(0)$, α and β are the fitting parameters. The value of $E_g(0)$, α and β for GaAs are 1.519 (eV), 0.541 (meV/K) and 204 (K), respectively. When the incident light has energy larger than the bandgap of a semiconductor, it is going to be absorbed by the semiconductor. In contrast, when the energy is below the bandgap, the semiconductor is transparent to the incident light, as long as there are no other absorption mechanisms. The band edge or the absorption edge is defined as the transition between the strong absorption at short wavelength (high energy) and the weak absorption at long wavelength (low energy) in the transmission spectrum of a semiconductor. The band edge of a semiconductor decreases with increasing temperature (Equation 2.1). Thus, by measuring the transmission of the semiconductor during the growth, we can monitor the substrate temperature. Since the BET directly measures the change of substrate temperature through the band edge, it is more accurate than the temperature read by the thermocouple placed near the

substrate, where thermocouple measures the temperature of the substrate's nearby environment.

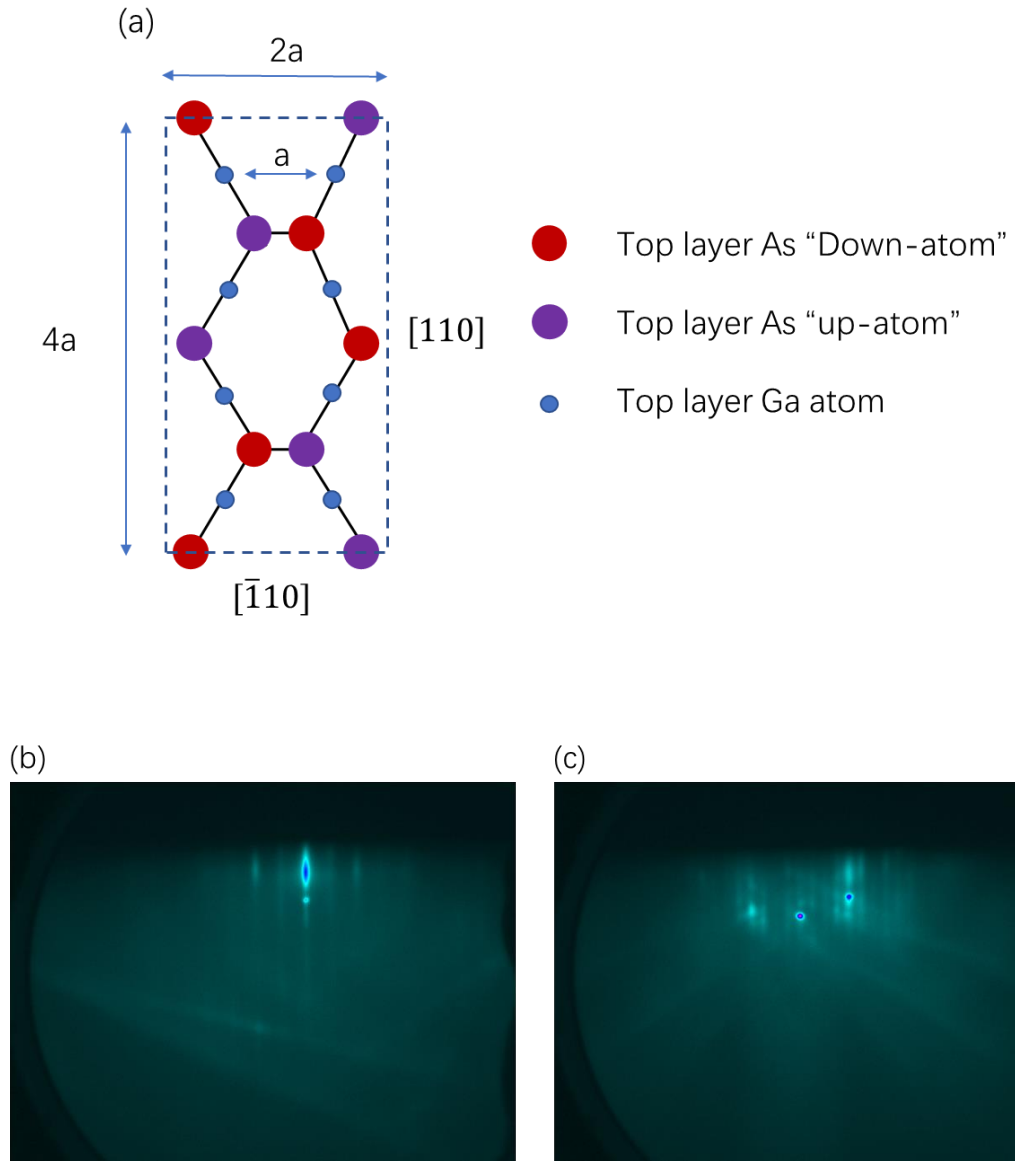

Figure 2.2: (a) Surface reconstruction of GaAs in As-rich environment. Due to the repulsion between two bonded As atoms, they are not going to be on the same surface. Instead, one atom is going to be lower than another, resulting in a 2×4 reconstruction pattern. (b) GaAs 2× patterns. (c) GaAs 4× patterns. (b) and (c) were taken by Patrick Sohr at the University of Delaware.

Third, RHEED is an *in situ* characterization technique for epitaxial growth. An electron gun is used to generate a beam of high energy electrons, which hits the wafer surface at a small angle then diffracts off the surface. The diffracted electron beam will then strike a phosphorescent RHEED screen, forming a diffraction pattern. The high energy electron diffraction pattern, which can be viewed as the reciprocal lattice of surface, provides us with information about the surface structure as well as growth quality. For example, the growth of GaAs is terminated by As layer. All the As atoms are bond to Ga atoms in all directions except the ones on the surface, resulting in some dangling bonds. To lower the surface energy, these surface As atoms choose to bind to each other, which is called surface reconstruction (Figure 2.2 (a)). The bulk crystal structure determines the way they reconstruct because the atoms below restrict their movement. As a result, the surface reconstruction pattern is also a periodic structure and the period is related to the bulk crystal lattice constant. Assuming the period of GaAs surface pattern is a before reconstruction, then due to the reconstruction, the period of the pattern changes to $2a$ along $[\bar{1}10]$ direction and $4a$ in [110], which is called 2×4 reconstruction (see Figure 2.2 (b) and (c)). When the two As atoms bond to each other, the repulsion between them force one to be lower than another, resulting in $4a$ period rather than a. RHEED is also used to detect the growth quality during the growth. As we mentioned before, RHEED patterns can be viewed as the reciprocal lattice of thin surface layers. The lattice point of a thin layer is stretched in reciprocal space due to the shape effect, resulting in streaky lines in RHEED patterns for a smooth surface (Figure 2.3 (a)). For a rough surface with small islands on the surface, electrons will interact with a 3D lattice rather than a thin layer which is close to a 2D plane. In this situation, we will observe spotty patterns on the RHEED screen (Figure

2.3 (b)). Also, the oscillation of RHEED intensity can be used to determine the growth rate. During layer-by-layer growth, one layer is completed before any other atom is added to the next layer, which leads to the periodic change of surface morphology. The RHEED intensity is strongest when a single layer is formed completely. Then the intensity gradually damps due to the formation of small islands. The period of the RHEED intensity oscillation is equal to the time taken to grow a single period of the crystal structure.

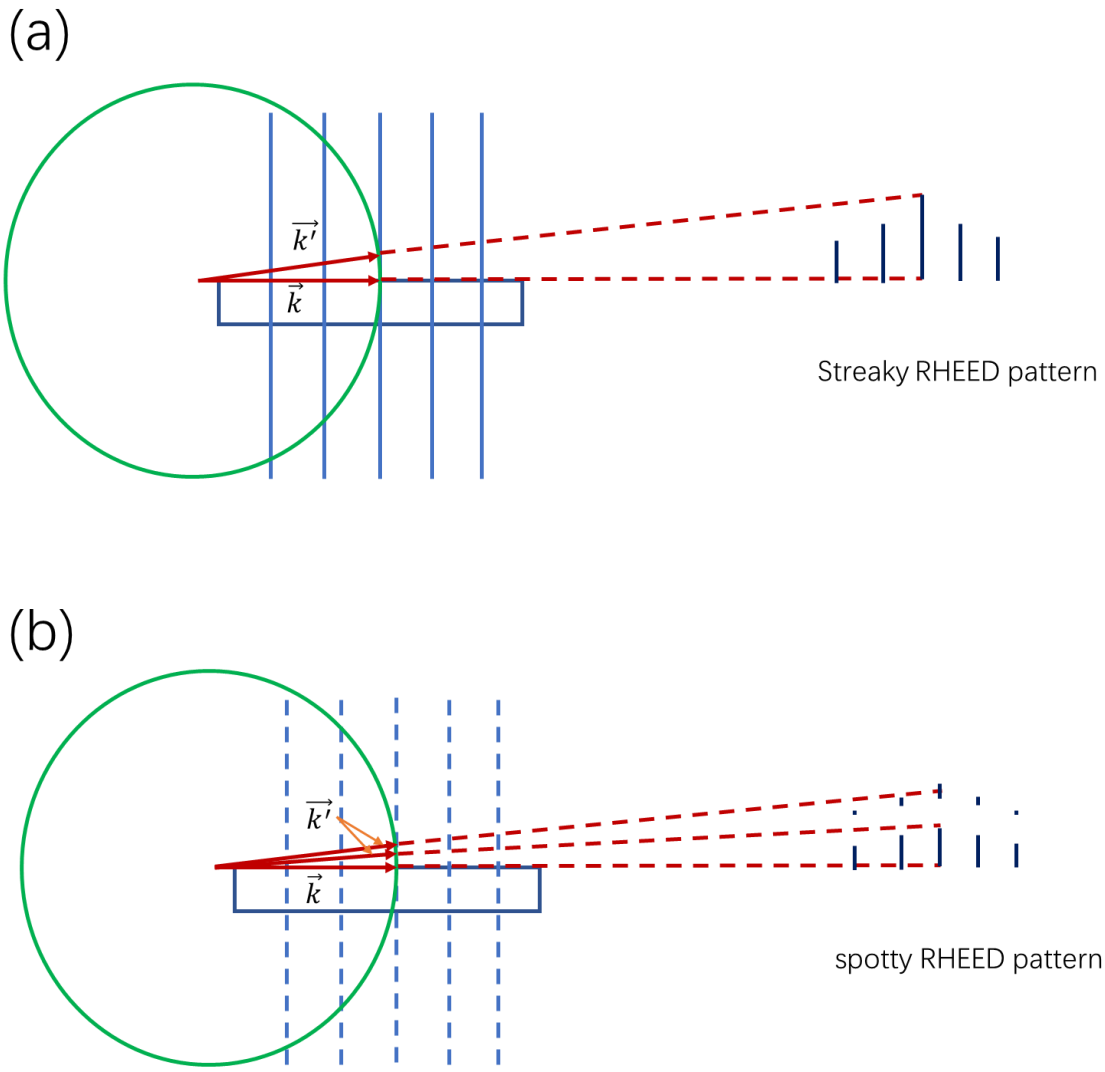

Figure 2.3: (a) Streaky RHEED pattern when the surface is smooth. (b) Spotty RHEED pattern when the surface is rough. The Green circle is the Ewald's sphere used to derive the diffraction condition. $\vec{k}$ is the wavevector of the incident electron beam. $\overrightarrow{k'}$ corresponds to the wavevector that satisfying diffraction condition.

Other key advantages of MBE include a slow growth rate and a low impurity level. The growth rate of MBE varies from a few nanometers per hour to a few

microns per hour, which makes it suitable for the growth of nanoscale structures such as quantum dots and quantum wells. MBE also gives us an atomically sharp interface which is important for many device applications. The ultra-high vacuum character of MBE maintains a low impurity and contaminant level in the chamber, resulting in single-crystal films with high purity.

2.2 Nanofabrication Techniques

We use various nanofabrication techniques to process our samples. I will introduce two primary techniques in this chapter: lithography and e-beam evaporator. We conducted these nanofabrication processes at the University of Delaware Nanofabrication Facility (UDNF).

2.2.1 Photolithography and E-beam Lithography

Lithography is a widely used nanofabrication technique in academic research and industry. It is a process used to create patterns on thin films. The general three steps of lithography include (see Figure 2.4):

1. Photoresist (or e-beam resist) spin coating
2. Exposure
3. Development

Photoresists are some polymers sensitive to UV light or electron. The chemical structure of the photoresist will change when it is exposed to the UV light or electrons, resulting in a structure soluble (positive photoresist) or insoluble (negative photoresist) in a certain developer. Photoresists were spin-coated on the clean surface of wafers at speed from 2000 rpm to 6000 rpm. Different spin-coating speed results in different photoresist thickness. Then the substrate will be baked at a hotplate to move excess

photoresist solvent. The exposure process is different for optical lithography and e-beam lithography. For optical lithography, the intense light will shine through a photomask and interact with the photoresist. Thus the pattern on the photomask will be transferred to the sample surface. For e-beam lithography, we create patterns by some software and the computer will control the movement of the e-beam to write the photoresist. The e-beam writer we used at the University of Delaware is Raith EBPG5200 with minimum feature size at 7nm. Depending on the types of photoresist, a post-exposure bake could be required. Development solutions are usually some alkaline solutions that could dissolve photoresist. After exposure, we immerse the wafer into the development solution for a certain amount of time (usually 30s to 60s). Exposed (unexposed) part of positive (negative) photoresist will dissolve in the solution. Then the lithography process is done. Wafer with photoresist patterns is now ready for the next nanofabrication step, such as metal deposition, wet etch, dry etch, etc.

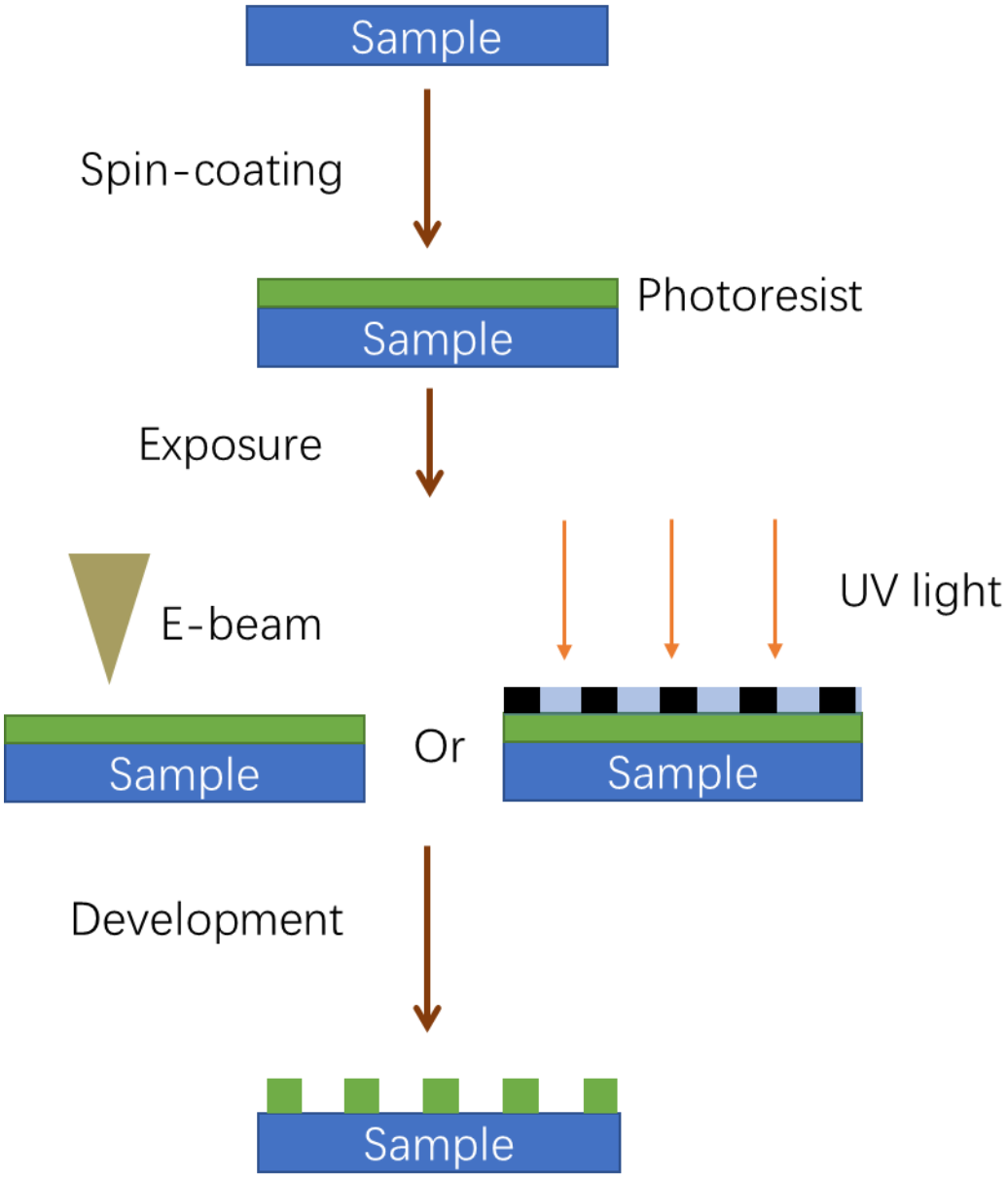

Figure 2.4 Schematic of photolithography and e-beam lithography.

2.2.2 E-beam Evaporation

E-beam evaporation is a physical deposition technique conducted in a high-vacuum environment (1×10^{-8} Torr to 1×10^{-6} Torr). Target metal material is

evaporated upon the bombardment of electrons with high kinetic energy, coating the surface of the wafer as well as the walls of the chamber. The electron beam is generated from a charged tungsten filament through thermionic emission, field electron emission or other methods. The generated electron beam will then be accelerated by a voltage and directed by a magnetic field toward the target material (Figure 2.5). The e-beam evaporator we use at the UDNF is a dual e-beam evaporator with two six-pocket e-beam sources.

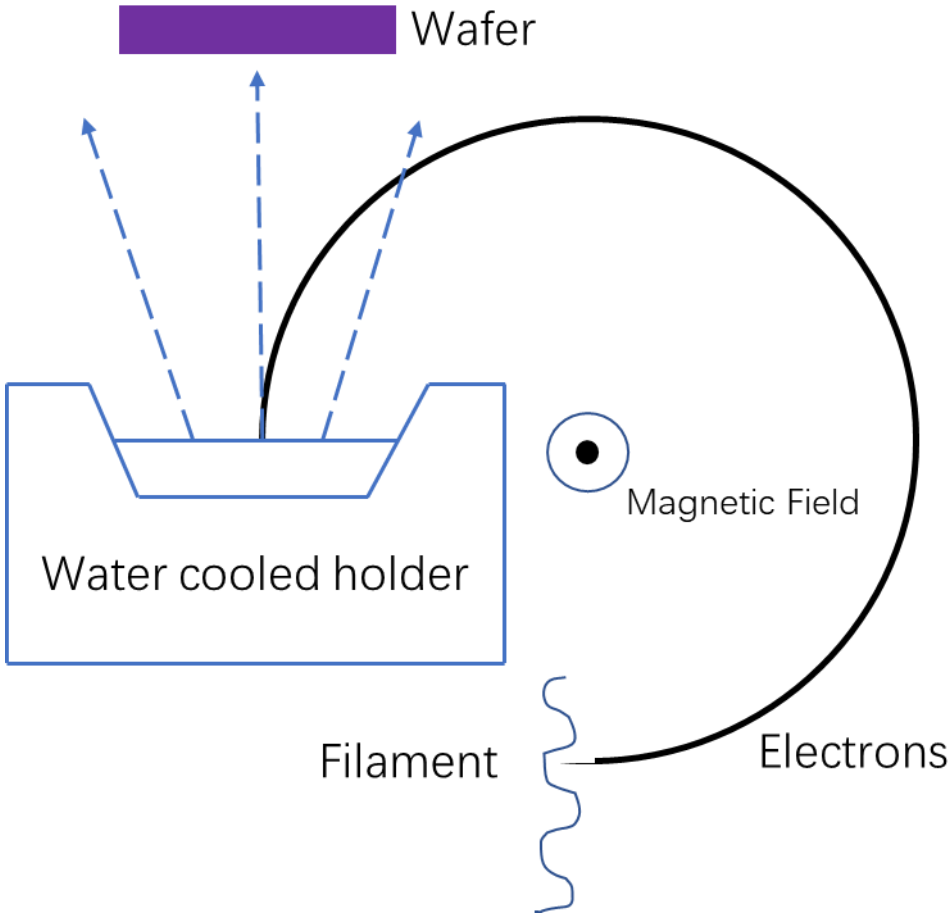

Figure 2.5: Schematic of e-beam evaporation.

We used an e-beam evaporator to deposit Ti (15nm) /Au (100nm) thin films on photoresist patterned wafers (see Chapter 4). After the deposition, wafers were soaked in warm N-Methyl-2-pyrrolidone (NMP) solution to remove excessive photoresist and Ti/Au films that rest on the top of the photoresist.

2.3 Characterization Tools

We use multiple tools to characterize the optical properties, electronic properties and surface morphology of our materials. Fourier transform infrared spectroscopy, which will be discussed in Section 2.3.1, is the most important tool we used to study the optical properties of our films. Other techniques such as Hall measurement, scanning electron microscopy, profilometer, and atomic force microscopy were used to characterize the electrical and surface morphology of the films. They will be briefly introduced in Section 2.3.2.

2.3.1 Fourier Transform Infrared Spectroscopy

We use Fourier transform infrared spectroscopy (FTIR) to collect the reflection and transmission spectrum of our samples. The machine we use is a Bruker Vertex 70V Fourier transform infrared spectrometer. Compared to a dispersive spectrometer, FTIR collects signals from samples over a wide spectral range simultaneously, which significantly reduces the time required for a measurement. The raw signal requires a Fourier transformation to obtain the actual spectrum.

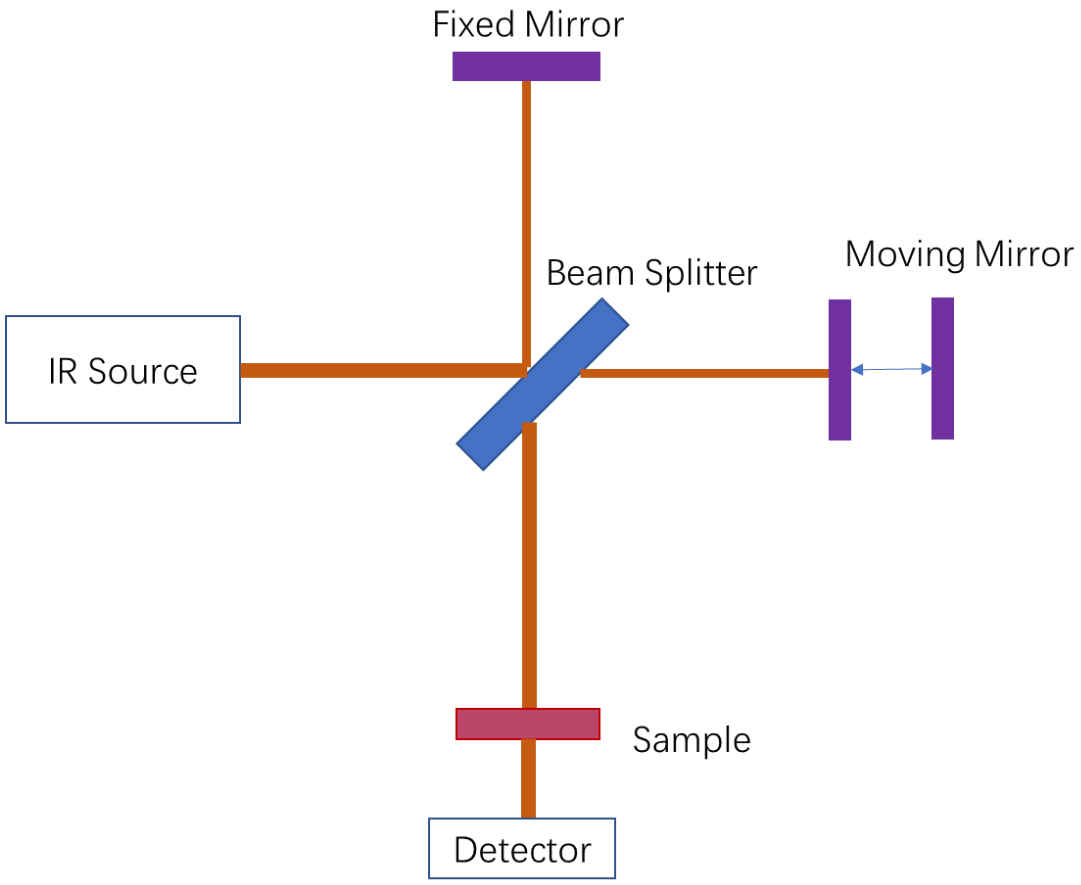

Figure 2.6: Diagram of an FTIR

The major components of an FTIR include an IR source, an interferometer, a beam splitter, and a detector. Figure 2.6 is a simplified diagram of how an FTIR works. When IR light is incident on the beam splitter, it will be separated into two beams. One will be reflected by a stationary mirror, while another will be reflected by a moving mirror. The two reflected beams recombine at the beamsplitter, interfering with each other. Assuming the fixed and movable mirrors are of the same distance from the beamsplitter (zero retardation), then the two beams travel the same distances through the same materials. Since there is no phase difference between the two

reflected beams, they constructively interfere with each other. Therefore, all light from the source reaches the detector with zero retardation, ignoring other losses in the whole optical path. If the moving mirror is at a distance λ/4 further (or shorter) than the fixed mirror, the optical path difference of the two reflected beams is going to be λ/2 (round trip), resulting in destructive interference of the two beams. Similarly, if the moving mirror is displaced by λ/2 further (or shorter) than the fixed mirror, the phase difference of two reflected beam is going to be 2π (optical path difference is λ), now the two beams constructively interfere with each other again. When the moving mirror moves at a constant velocity, the signal arriving at the detector varies sinusoidally in time for a monochromatic source. If the source emits a certain range of wavelengths, we could imagine that the signal intensity is largest at zero retardation since each wavelength has a constructive pattern.

After recombination, the beam will interact with the sample and finally be received by a detector. The detector records the signal intensity as a function of moving mirror position. We call this raw data an interferogram (Figure 2.7 (a)). It is difficult to interpret the interferogram directly, so we transform it into a spectrum as a function of frequency. To do this, we apply a Fourier transform to the interferogram:

$$\tilde{f}(v) = \int_{-x}^{x} f(x) e^{-2i\pi vx} dx \qquad \text{(Equation 2.2)}$$

Where $f(x)$ is the signal recorded by the detector which is a function of the moving mirror position, $\tilde{f}(v)$ is the spectrum which is a function of frequency v. Figure 2.7 shows an interferogram (Figure 2.7 (a)) and its spectrum (Figure 2.7 (b)) after Fourier transformation. From the above equation, we can also deduce that the spectral resolution (cm^{-1}) is determined by the travel length of the moving mirror (cm). A maximal retardation of 0.25cm corresponds to $4\mathrm{cm}^{-1}$ spectral resolution.

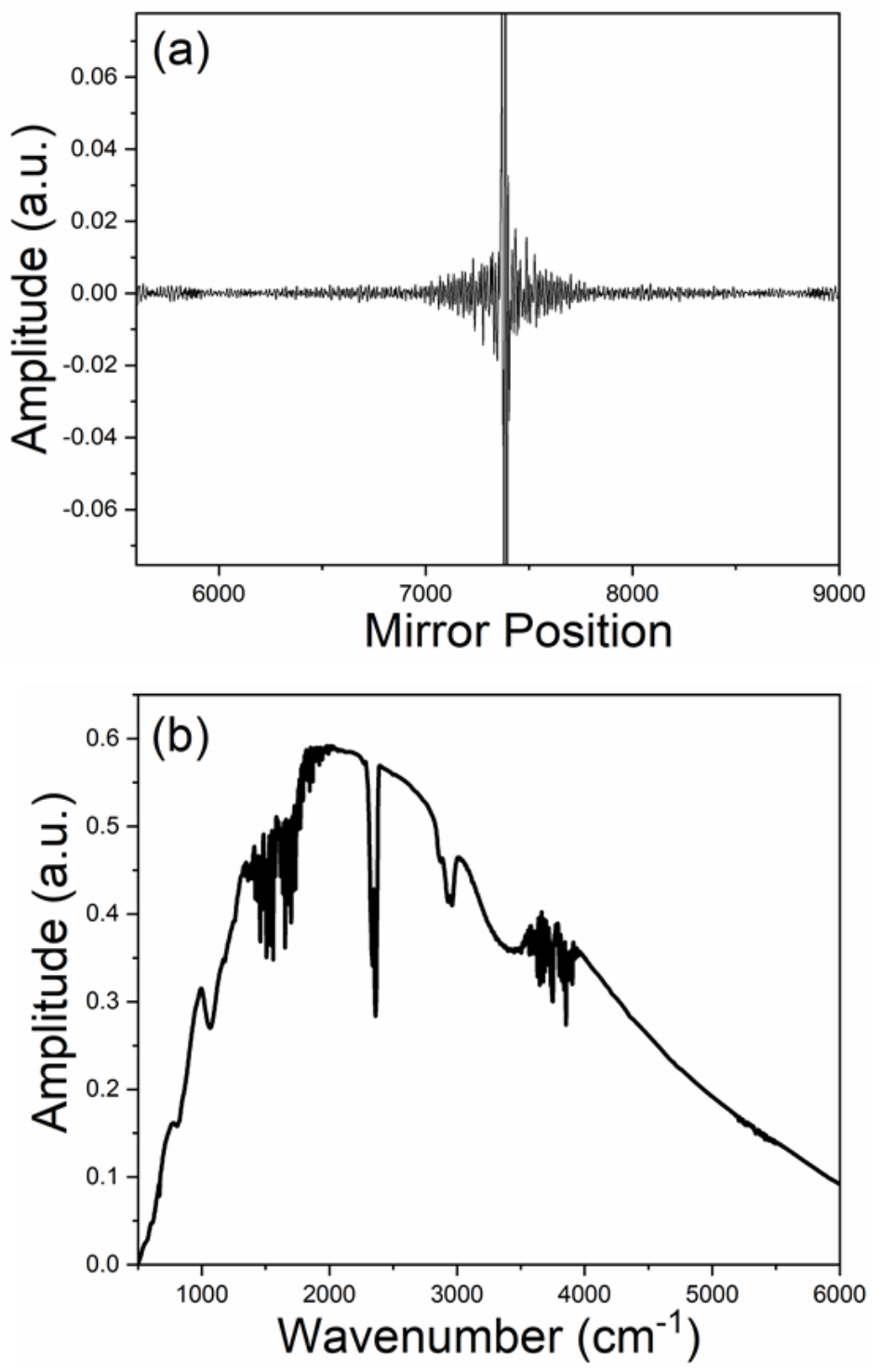

Figure 2.7: (a) Part of an interferogram. (b) Spectrum as a function of wavenumber

2.3.2 Other Measurement tools

2.3.2.1 Hall Measurement

Room temperature Hall measurement is used to characterize the electrical properties of films, providing us with sheet carrier density, mobility, and carrier type. The basic physical principle behind the Hall effect is the Lorentz force. When we apply a magnetic field perpendicular to the direction of electron flow, the electrons will experience a Lorentz force which forces electrons to move to one side of the conductor and results in a Hall voltage (See Figure 2.8).

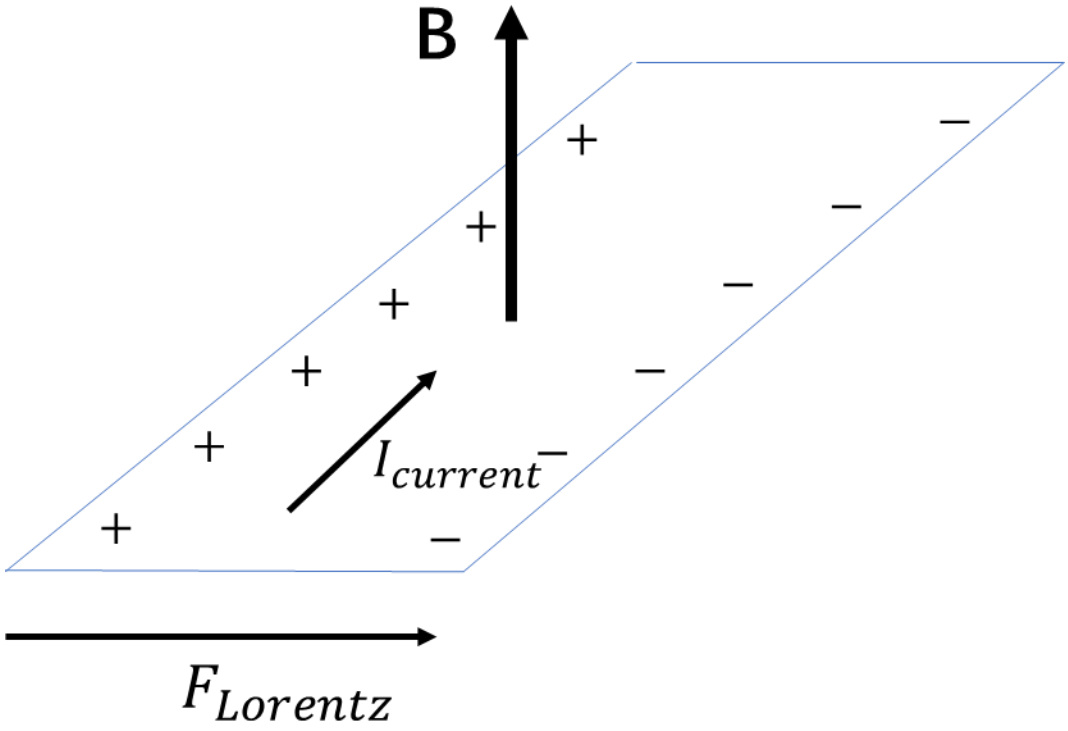

Figure 2.8 Electrons experience Lorentz force induced by the perpendicular magnetic field

We can get the electrical properties of the conductor by measuring the Hall voltage. We use a custom-built Hall effect system at the University of Delaware. The measurements were conducted using the van der Pauw geometry, a common technique used to measure the resistivity and Hall effect (see Figure 2.9). To do the Hall measurement, we first cut the samples into 1cm×1cm square pieces and put a moderate amount of indium metal on the four corners (blue areas in Figure 2.9). Then four probes were placed in contact with the indium on the corners. Before the measurement, we usually run a contact check to make sure the four probes were in good contact with the sample. Resistivity measurements were conducted to determine the sheet resistance R_s. Van der Pauw demonstrated that there are two characteristic resistances R_a and R_b related to the sheet resistance R_s through van der Pauw equations:

$$e^{\frac{-\pi R_A}{R_S}} + e^{\frac{-\pi R_B}{R_S}} = 1 \qquad \text{Equation (2.3)}$$

Here we measure the R_A by running current from probe A to probe B while measuring the voltage between probes C and D. R_A then can be calculated as follows:

$$R_A = \frac{V_{CD}}{I_{AB}} \qquad \text{Equation (2.4)}$$

Similarly, we can derive R_B by applying a current through probe B and D then measure voltage from probe A to C:

$$R_B = \frac{V_{AC}}{I_{BD}} \qquad \text{Equation (2.5)}$$

The sheet resistance R_s then can be solved from Equation 2.1. The bulk resistance is calculated from the following equation:

$$\rho = R_s t \qquad \text{Equation (2.6)}$$

Here, t is the thickness of the sample.

After the resistivity measurement, we can conduct Hall measurement to determine sheet carrier density n_s and mobility μ. The Hall effect measurement first runs a current from probe A to probe B then measures the Hall voltage from probe D and C. During the process, a magnetic field is applied in the direction out of the page. After measuring multiple Hall voltages at multiple magnetic field strengths, the Hall coefficient H_A can be derived by linearly fitting to the equation:

$$H_A = \frac{V_{BC}}{I_{AD}B} \qquad \text{Equation (2.7)}$$

where B is the magnetic field. Similarly, we can derive H_B by applying a current through B and C then measure Hall voltage between A and C:

$$H_B = \frac{V_{AD}}{I_{BC}B} \qquad \text{Equation (2.8)}$$

The sheet concentration can be calculated as follows:

$$n_s = \frac{\frac{-1}{qH_A} + \frac{-1}{qH_B}}{2} \qquad \text{Equation (2.9)}$$

Where q is the elemental charge. A negative n_s indicates that electrons are majority carrier and a positive n_s indicates that holes are majority carrier. The bulk carrier concentration is:

$$\mathrm{n} = \frac{n_s}{t} \qquad \text{Equation (2.10)}$$

where t is the sample thickness. The mobility is calculated using the following equation:

$$\mu = \frac{1}{qn_s\rho} \qquad \text{Equation (2.11)}$$

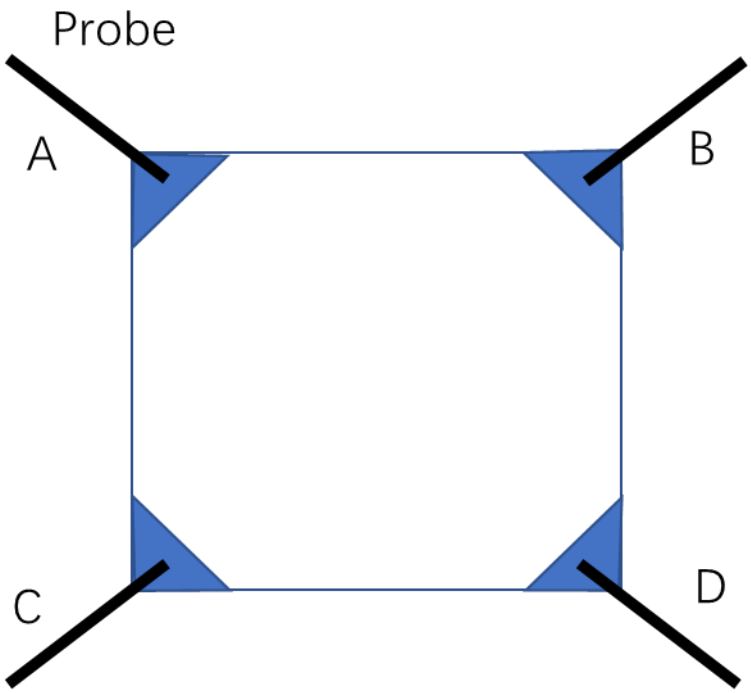

Figure 2.9: Schematic of the van der Pauw geometry used for Hall effect measurement. Blue triangles in the corners represent contact (Indium), while black lines represent the probes.

As mentioned in Section 2.1, we use Hall measurement to calibrate Si cell flux by growing a series of Si:InAs at different Si temperatures and then measure their carrier densities. Hall measurement is also a major technique that we used to study the electrical properties of Si:InAs samples with bismuth surfactant (Chapter 5).

2.3.2.2 Scanning Electron Microscopy

Scanning electron microscopy (SEM) is a type of electron microscope using a finely focused electron beam to scan the sample surface. When the electron beam interacts with the sample, multiple signals are generated. The most common signal we would like to use is the secondary electrons emitted by the atoms. When the beam

electrons interact with the electrons within the sample, they are going to repel with each other since they are all negatively charged. During the repulsion, the beam electrons will be slowed down, and part of the energy will be transferred to the electrons in the sample. The strength of the repulsion could be so great that the specimen electron could be pushed out of the atom and exit the surface if they still have sufficient energy. These electrons are called secondary electron. The generation of the secondary electron is topography sensitive. It reveals the surface morphology of the sample. We use SEM to examine the cross-sectional surface of the multilayer structure (Chapter 4) as well as the sample surface morphology (Chapter 5).

2.3.2.3 Atomic Force Microscopy

Atomic force microscope (AFM) is a type of scanning probe microscope with high-resolution below a nanometer. AFM is widely used for detecting the properties of the sample surface. AFM has a cantilever with a sharp tip with a radius in the order of nanometers. When the sharp tip is in the near-field of the sample surface, the force, determined by Hooke's law, between the tip and sample surface atoms were measured through the deflection of the cantilever. As shown in Figure 2.10, a laser is used to detect the deflection of the cantilever. The laser is reflected off the back of the cantilever and collected by a position detector whose output signal could provide us with the deflection of the cantilever. There are two common modes in AFM: tapping mode and contact mode. In contact mode, the tip is dragged across the sample surface which could cause the surface damage and tip stick to the surface, especially in ambient conditions. Tapping mode solves this problem by having tip touch the surface only for a short time. During the tapping mode, the cantilever is driven to oscillate up

and down near its resonance frequency. We use the tapping mode to study the sample surface features in Chapter 5.

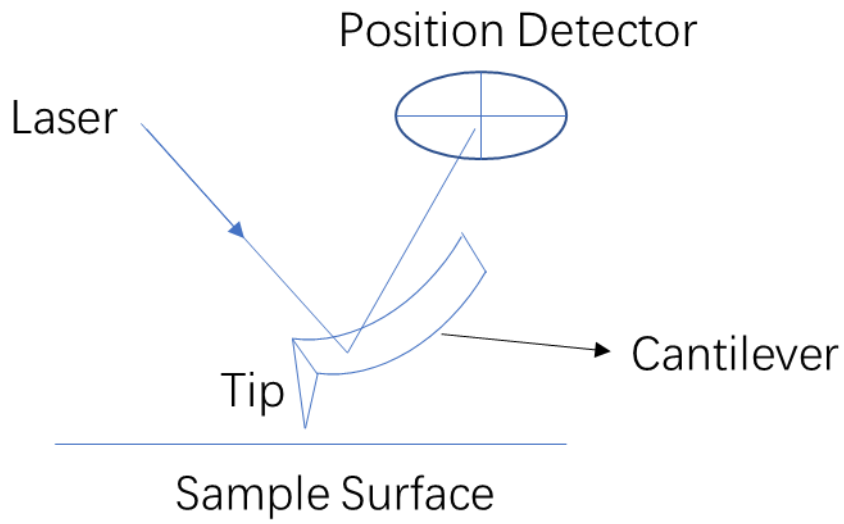

Figure 2.10: Schematic of how an AFM works.

2.4 Simulation Tools

2.4.1 COMSOL Multiphysics

COMSOL Multiphysics is a commercial software using finite element method (FEM) to solve a variety of problems in engineering and physics.

Most processes in engineering and physics can be generalized to partial differential equations with specific boundary conditions. These partial differential equations could be complicated and challenging to achieve accurate analytic results. FEM is a computational method that gives us an approximate solution for these equations. The idea of FEM can be simplified as “Divide and Conquer”. FEM breaks

down a big object into lots of small finite elements. The calculation for each small element is simple. By combining the results from every single element, FEM can predict the behavior of the original object.

We use the wave optics module in COMSOL Multiphysics to study how electromagnetic wave interacts with our samples. The module is based on Maxwell's equations:

$$\nabla \cdot \mathbf{D} = \rho \qquad \text{(Equation 2.12)}$$

$$\nabla \cdot \mathbf{B} = 0 \qquad \text{(Equation 2.13)}$$

$$\nabla \times \mathbf{E} = -\partial_t \mathbf{B} \qquad \text{(Equation 2.14)}$$

$$\nabla \times \mathbf{H} = \mathbf{J} + \partial_t \mathbf{D} \qquad \text{(Equation 2.15)}$$

where **E** is the electric field, ρ is the electric charge density, **D** is the electric displacement field, **B** is the magnetic flux density, **H** is the magnetic field, **J** is the current.

Here is the typical simulation workflow to run a simulation in COMSOL:

1. Set up a model environment.
2. Create Geometric Objects
3. Specify Materials properties
4. Define physics boundary conditions
5. Create the mesh
6. Run simulation
7. Process data

The model environment we used in COMSOL is a 2D wave optics module in the frequency domain. Figure 2.11 (a) shows the geometric object we created for simulating the Si:InAs HMMs. The permittivity of air and intrinsic InAs layers are 1

and 12.3 respectively. The Si:InAs is described by the built-in Drude Lorentz dispersion model, and we need to specify the high-frequency relative permittivity, oscillator strength, and the scattering rate. In the model, we define the two sides as periodic boundaries (Figure 2.11 (b)). We also specify that the light is going to incident from port 1 (Figure 2.11 (b)). Port 2 is used to calculate the transmission. We also need to specify the light properties at each port, such as polarization and incident angle, depending on our needs. The next step is to create the mesh. The mesh size should be smaller than the thickness of a specific layer. But an extremely small mesh size leads to long computation time. The mesh size we used for our model ranging from 5×10^{-10} to 1×10^{-7}m, depending on the thickness of each layer (Figure 2.11 (c)). After we run the simulation, we can output information such as reflection, electromagnetic field distribution, heat loss, *etc.*

We used COMSOL to simulate the reflection of InAs HMM in Chapter 3. In Chapter 4, We used COMSOL to study the properties, including reflection and magnetic field distribution, of volume plasmon polaritons in different HMMs.

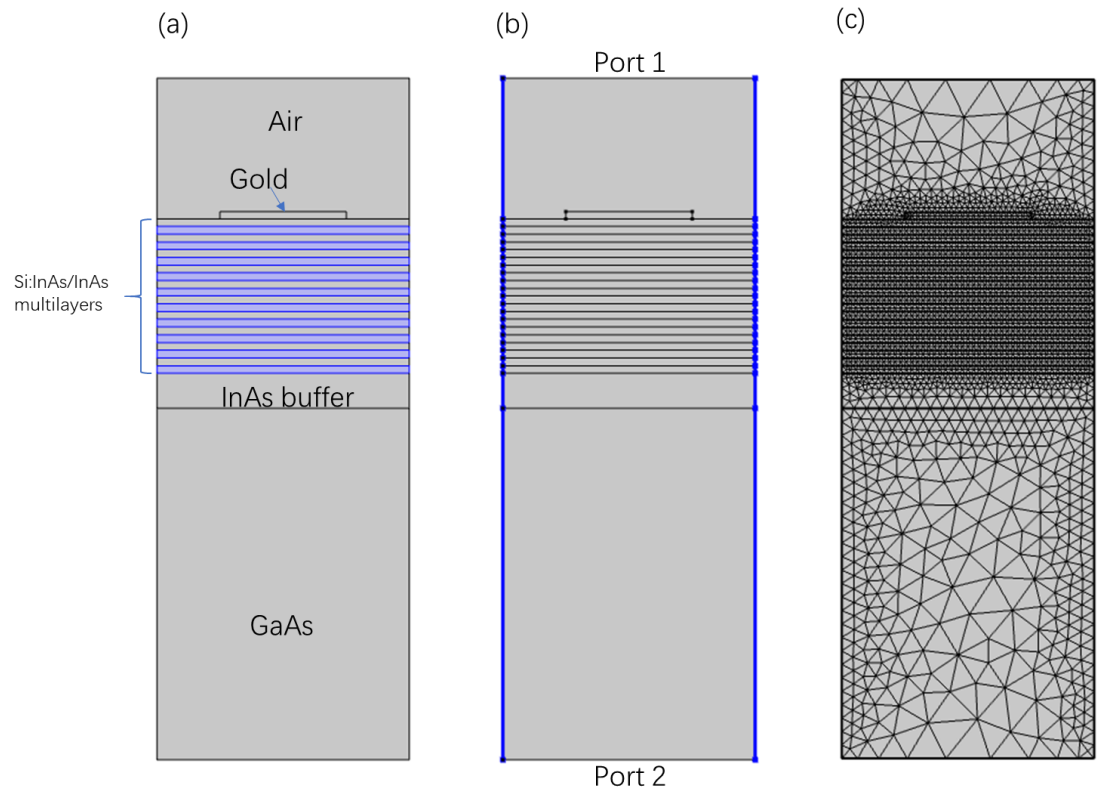

Figure 2.11: (a) Define Geometric model. (b) Define physics boundary conditions. The two sides are periodic boundaries. (c) Create the mesh.

2.4.2 NextNano

NextNano is a software for the simulation of electric and optoelectronic semiconductor nanodevices. It is a powerful tool for the simulation of nanostructures including laser diodes, quantum dots, quantum cascade laser and HEMT where quantum physical effects take place. NextNano uses advanced physical method to simulate the quantum mechanical properties of various nanostructures form by different materials.

We use NextNano to simulate the band structure and electron distribution in our multilayer HMMs (see Section 4.5). To run a simulation, we first specify the

geometric structure. Our layered structures can be viewed as a 1D structure, so we only need to tell the program the thickness of each layer and what substrate did we used. Then we specify the properties of each material. Here, we imported the built-in properties for each material. Similar to COMSOL, we also need to specify the mesh size and the physics we want to use. The mesh size we used is around 0.5nm. The quantum physics model I used is an effective mass model. After running the simulation, we can output results including conduction band, valence band, electron distribution, Fermi level, *etc.* (See Figure 2.10). We used NextNano to model the electron distribution of HMM (Chapter 4) and design the quantum wells (Chapter 6).

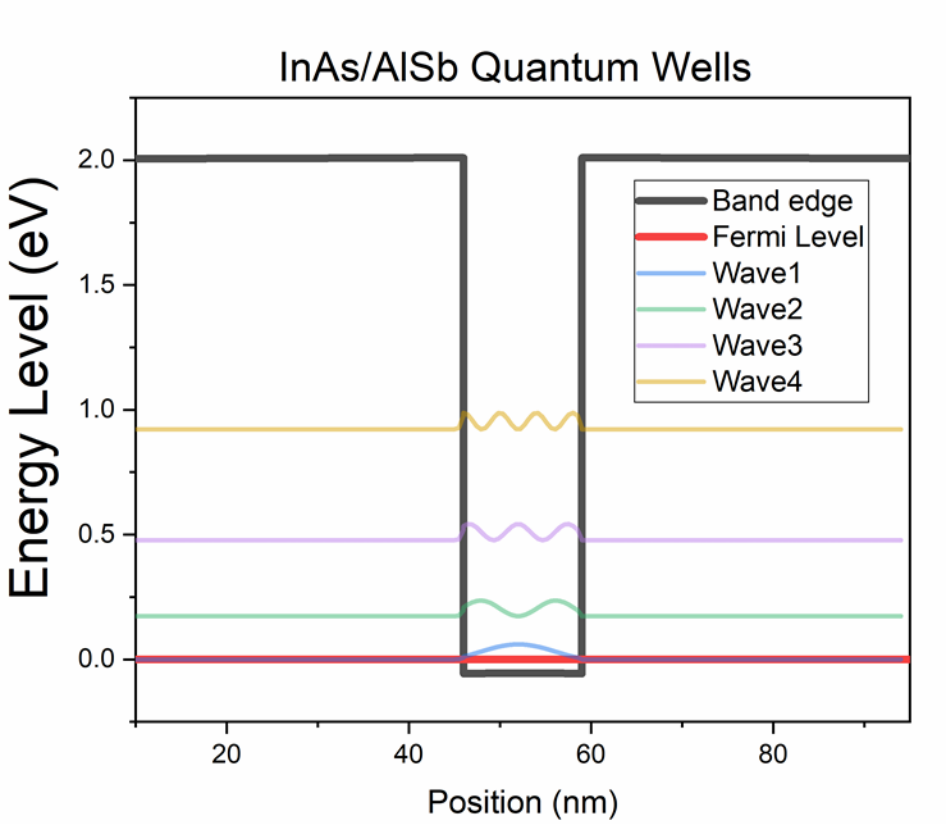

Figure 2.12: Band edge, Fermi level and the first four squared wave functions of InAs/AlSb quantum wells calculated by Nextnano using effective mass model.

Chapter 3

SINGLE MATERIAL HYPERBOLIC METAMATERIALS

3.1 Background of Single Material Hyperbolic Metamaterials

As was discussed in Section 1.3, III/V semiconductors, such as InAs and InGaAs, are designer metals for the infrared. This allows us to use these materials to create layered HMMs for the infrared. In ref [7], Anthony J Hoffman et al. demonstrated a semiconductor HMM composed of alternating Si: InGaAs and InAlAs layers. The thickness of each layer is around 80nm. The smallest plasma wavelength achieved with these structures was 8.8μm. The structures exhibited both discontinuity of the Brewster angle and negative refraction, two hallmarks of HMMs. This is the first demonstration of HMM using III/V semiconductors. However, it was difficult to push the InGaAs plasma wavelength to wavelength smaller than 7μm. In addition, the growth of a latticed match ternary system is relatively complicated compared to a binary system.

Here we developed the idea of creating HMMs using a single material system consisting of Si:InAs and InAs layers (Figure 3.1). As I mentioned in Section 1.3, the plasma wavelength of InAs can be adjusted to 5.5μm, enabling a broader working range than InGaAs HMM. Additionally, the growth of a single material system is straightforward and easy. We don't need to worry about the lattice mismatch between layers except the initial layer. To reduce the effect of lattice mismatch, we grew a thick InAs buffer layer (500nm) between GaAs substrate and active layers. We grew samples with different structure parameters and studied their optical properties by

FTIR. We also set up an optical measurement to demonstrate the negative refraction of our materials.

In this chapter, I will describe the growth procedure and optical setup used to characterize the InAs HMMs (Section 3.2). We systematically studied the reflection and transmission properties of the InAs HMMs with different doping levels and metal:dielectric thickness ratios (Section 3.3). Effective medium theory (EMT) was used to simulate the reflection and transmission of the samples (see Section 1.2.2.2). We also experimentally demonstrated the discontinuity of the Brewster angle (Section 3.4) and negative refraction (Section 3.5), two characteristics of HMMs. The study of single material HMMs lays a solid foundation for understanding the optical behavior of semiconductor HMMs in the infrared. It is a straightforward structure to explore the properties of semiconductor HMMs and the growth is less complicated than that of a ternary system. The conclusions can also be applied to HMM created from other materials. In addition, the study of InAs HMMs demonstrates a structure with designer optical properties across the infrared. It opens up the possibility of HMMs with a simpler design.

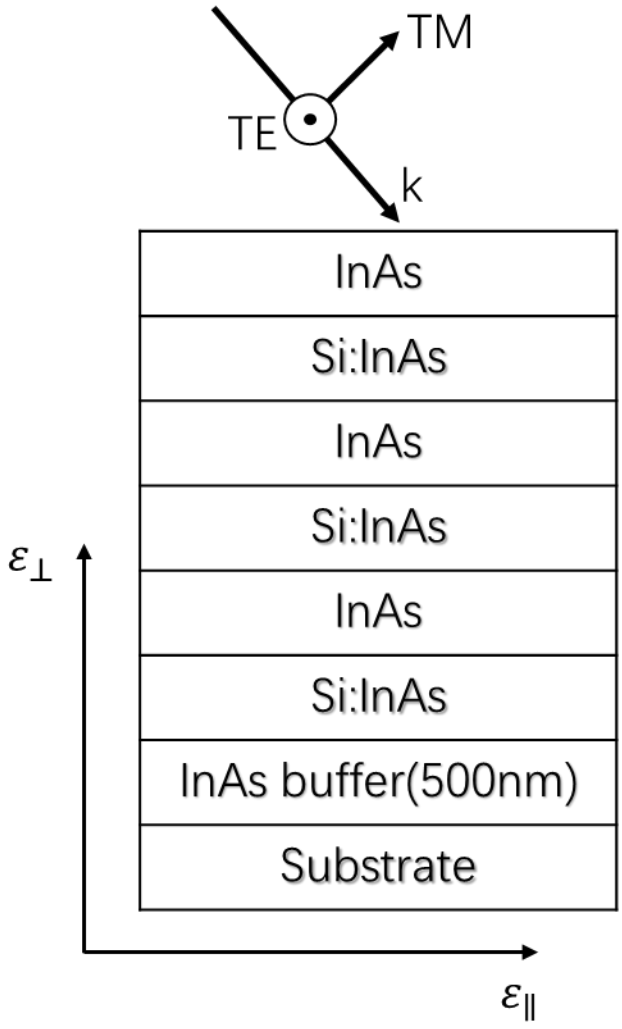

Figure 3.1: Schematic of single material InAs HMMs structure. The figure indicates the directions of parallel and perpendicular permittivity. The figure also indicates the electrical field direction of TM and TE polarized light which will be mentioned in the following sections.

3.2 The Growth of Si:InAs/InAs Hyperbolic Metamaterials

Five Si:InAs/InAs HMM samples were grown by the OSEMI NextGEN solid source MBE with effusion cells for Si, In and a two zoned valved cracker source for As_2. More details about the MBE can be found in Section 2.1. These samples were

grown on single side polished undoped GaAs substrates. The growth and thermal desorption of the oxides of the substrate were monitored by reflection high energy electron diffraction (see Section 2.1). The flux of indium and arsenic were measured by a beam flux monitor. The As_2/In flux ratio was around 7. The growth rate of InAs varied from 1.25~1.85μm/h. The Si flux was confirmed by Hall measurements on several bulk Si:InAs calibration films assuming 100% ionization efficiency. The substrate temperature was monitored by band edge thermometry (BET) and a thermocouple near the substrate. The BET is more accurate than the thermocouple since it directly measures the change in band-edge absorption of the substrate (see Section 2.1). Before the growth, the temperature was increased to 620℃ (BET) for about 10 minutes to remove the oxides on the substrate. Throughout the oxide desorption and growth, the arsenic pressure was kept at 1×10^{-5} Torr. At the start of growth, the temperature was decreased to 450℃ (BET). A 500nm thick InAs was grown as a buffer layer to provide a clean surface and reduce the diffusion of the impurities from the substrate. It could also reduce the effect of the lattice mismatch between GaAs and the active layers. During the growth, the BET usually failed to read the temperature when the InAs layer thickness reached around 600nm due to the absorption by the InAs. InAs has a smaller band gap (~ 0.3 eV) than GaAs (~ 1.424 eV). When the InAs layer becomes too thick, light with energy larger than 0.3 eV will be completely absorbed by InAs and we are not able to detect the band edge change of GaAs. In this situation, we continued our growth by keeping the substrate thermocouple temperature constant. The properties of these five samples were summarized in Table 3.1. The thickness of the sample was confirmed by a profilometer. The HMM thickness, metal thickness (t_m), dielectric thickness (t_d), fill

factor ($\rho = t_m/(t_m + t_d)$), plasma wavelength (λ_p), and scattering rate (Γ) were estimated by fitting the angle-dependent transmission and reflection measurements to an effective medium theory model (see Section 3.3 and Section 3.4). The bandwidth was taken to be the width of Type I region in wavelength, determined by the value of parallel and perpendicular permittivity extracted from the effective medium theory model (the gray area in Figure 3.5 and 3.7). The bandwidth percentage normalizes the bandwidth to the central wavelength of the region. More details about bandwidth will be discussed in Section 3.4.

Table 3.1: Properties of Si:InAs/InAs HMM [97]. Reprint permission obtained from The Optical Society

Sample ID	HMM thickness (μm)	t_m (nm)	t_d (nm)	ρ	λ_p (μm)	Γ (x10^{13} rad/s)	Bandwidth (μm)	Bandwidth percentage (%)
1	2.80	110	110	0.50	5.8	1.9	2.25	32
2	2.80	112	108	0.51	6.7	1.9	2.55	31
3	2.42	87	113	0.44	9.5	1.4	2.70	25
4	2.30	47	153	0.24	9.8	1.5	1.05	10
5	2.33	147	53	0.74	9.2	1.6	1.40	14

3.3 Reflection and Transmission

FTIR was used to collect the polarized angle-dependent reflection and transmission of the samples. A liquid-nitrogen-cooled HgCdTe detector, ZnSe lenses, and a KRS-5 holographic wire grid polarizer were used to set up the measurement as described in Figure 3.2. The spectral resolution and the scan velocity are 4cm^{-1} and 40kHz, respectively. The reflection data was corrected by a gold mirror whose

reflection is assumed to be 100% in the infrared. The transmission data was normalized to the polarized transmission through the undoped GaAs substrate.

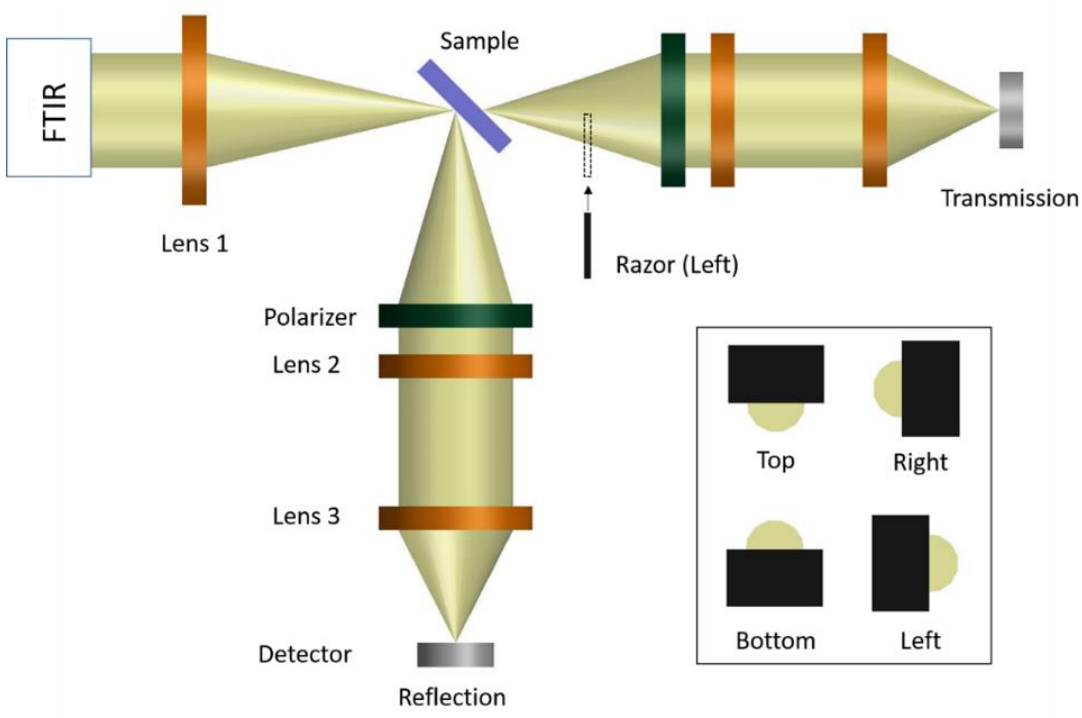

Figure 3.2: Top view schematic of the optical setup for angled transmission and reflection measurements. Inset shows the razor blade position for negative refraction experiments, as seen from the sample position [97]. Reprint permission obtained from The Optical Society.

We first look at the reflection and transmission data of Sample 1. We plot the TE reflection as well as TM and TE transmissions for Sample 1 in Figure 3.3. The direction of the electric field of TM and TE polarized light is indicated in Figure 3.1. TM reflection is plotted in Figure 3.4 (a) and (b) for comparison with other samples. When light travels through a multilayer structure, the reflected and transmitted light

from each interface interferes with each other, resulting in constructive and destructive patterns in the reflection and transmission spectrum. These patterns are called Fabry-Perot interference. Oscillations due to Fabry-Perot interference from the HMM and buffer layer are observed at a short wavelength for both reflection and transmission spectrum. Fabry-Perot interference is determined by the optical path difference of reflected and transmitted light from each layer. When we change the incident angle, the optical path also changes, resulting in a shift of the Fabry-Perot interference patterns. For TE polarized light, the electrical field is parallel to the layers and thus its behavior is only determined by the $\varepsilon_{\parallel}$. TE reflection (Figure 3.3 (a) and (b)) only exhibits Fabry-Perot interference features. The amplitude of the reflection monotonically increases with an increasing reflection angle at all wavelengths. This is significantly different from TM reflection which exhibits a more complicated relationship with varying reflection angles (see Figure 3.4 (a) and (b)). For TM polarized light, the electrical field has components in both parallel and perpendicular directions. Therefore, TM reflection and transmission are affected by $\varepsilon_{\parallel}$ as well as $\varepsilon_{\perp}$. TM reflection will be discussed in detail later. For transmission spectrums, we normalized the data to one for both experimental and simulated data for easier comparison. There is a strong absorption around the plasma wavelength and the strength increases with the angle in TM transmission (Figure 3.3 (c) and (d)) while this feature is not seen for TE polarized light (Figure 3.3 (e) and (f)). This is caused by the resonance when $\varepsilon_{\perp}$ changes from positive to negative. A bigger incident angle leads to a larger electrical field component in the perpendicular direction, resulting in stronger resonance. At longer wavelength, both TM and TE transmission decrease to 0

as reflection approaches 1 indicating a metallic behavior. As we will see in Figure 3.5, this is caused by a negative $\varepsilon_{\|}$ at long wavelength.

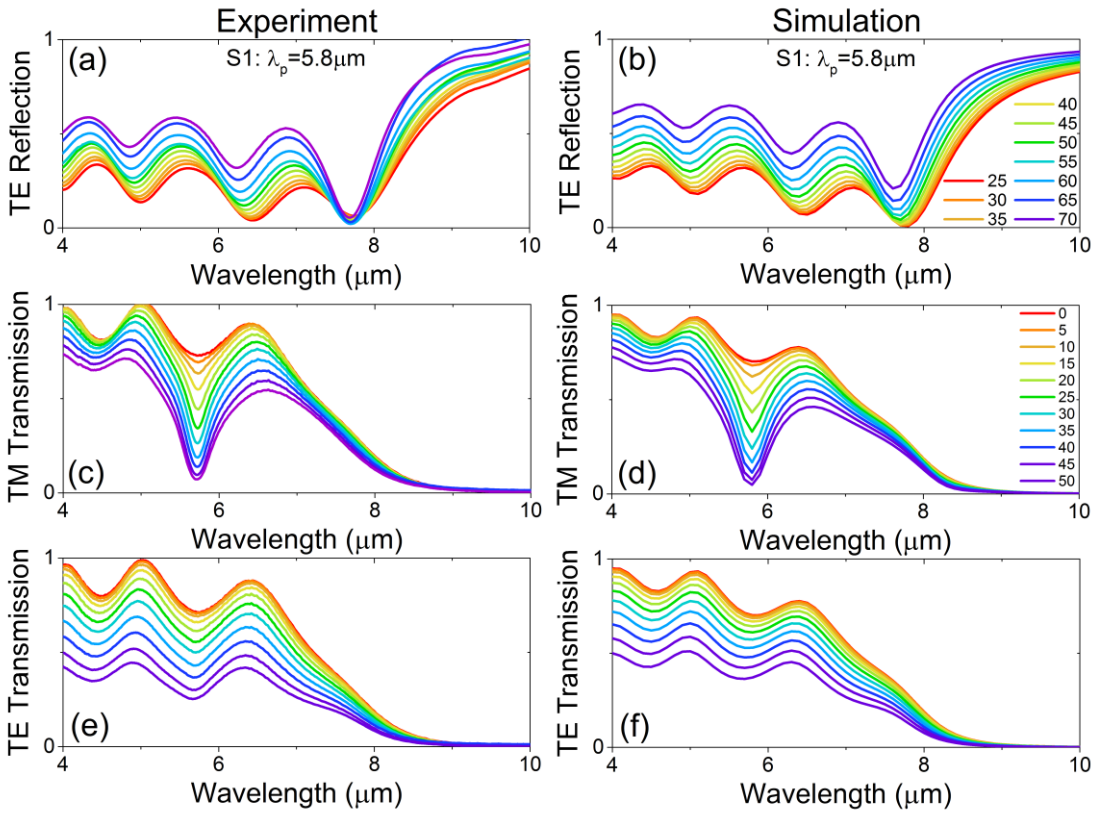

Figure 3.3: Data for Sample 1. Experimental (a) and simulated (b) TE reflection, experimental (c) and simulated (d) TM transmission, and experimental (e) and simulated (f) TE transmission. Other samples look similar. Both experimental and simulated TM and TE transmission data has been normalized to 1 for easier comparison of the relevant features [97]. Reprint permission obtained from The Optical Society.

In Figure 3.4, we compare the angle-dependent TM reflection of three samples with approximately the same fill fraction (around 0.5) but different plasma

wavelength (Sample1: 5.8μm, Sample 2: 6.7μm, Sample 3: 9.5μm). The experimental reflection angle varies from 25 to 70 degrees in 5 degrees increments. In simulated data, we also plot the data higher than 70 degrees (dotted line in Figure 3.4) which are not accessible for experiments due to light loss. All samples have similar scattering rates (1.4~1.9× 10^{13}rad/s) as shown in Table 1. At short wavelengths, the reflection for three samples is around 30% as expected for a semiconductor with a refractive index around 3.3. Fabry-Perot interference patterns are observed for all three samples. Different from TE reflection, we also observe an absorption around the plasma wavelength indicated by the arrow in the figure. This is the onset of Type I HMM region. Sample 1 (Figure 3.4 (a)) has the shortest plasma wavelength of around 5.8μm. The reflection for Sample 1 gradually approaches 1 after 8μm. At short wavelength, the reflection amplitude drops when we increased the reflection angle due to the angle of incidence approaching the Brewster angle (more details about the Brewster angle will be discussed in Section 3.5). Then the reflection amplitude increases after 65 degrees. Sample 2 (Figure 3.4 (c)) has a plasma wavelength around 6.7μm, and the reflection starts to increase after 9μm. The amplitude and Fabry-Perot interference pattern exhibit similar behavior with increasing angle as Sample 1. While for Sample 3 (Figure 3.4 (e)) which has the longest plasma wavelength at 9.5μm, the reflection amplitude stays below 50% for the range we plotted. The simulated TM reflection (Figure 3.4 (b, d, f)) using EMT predicts similar behaviors.

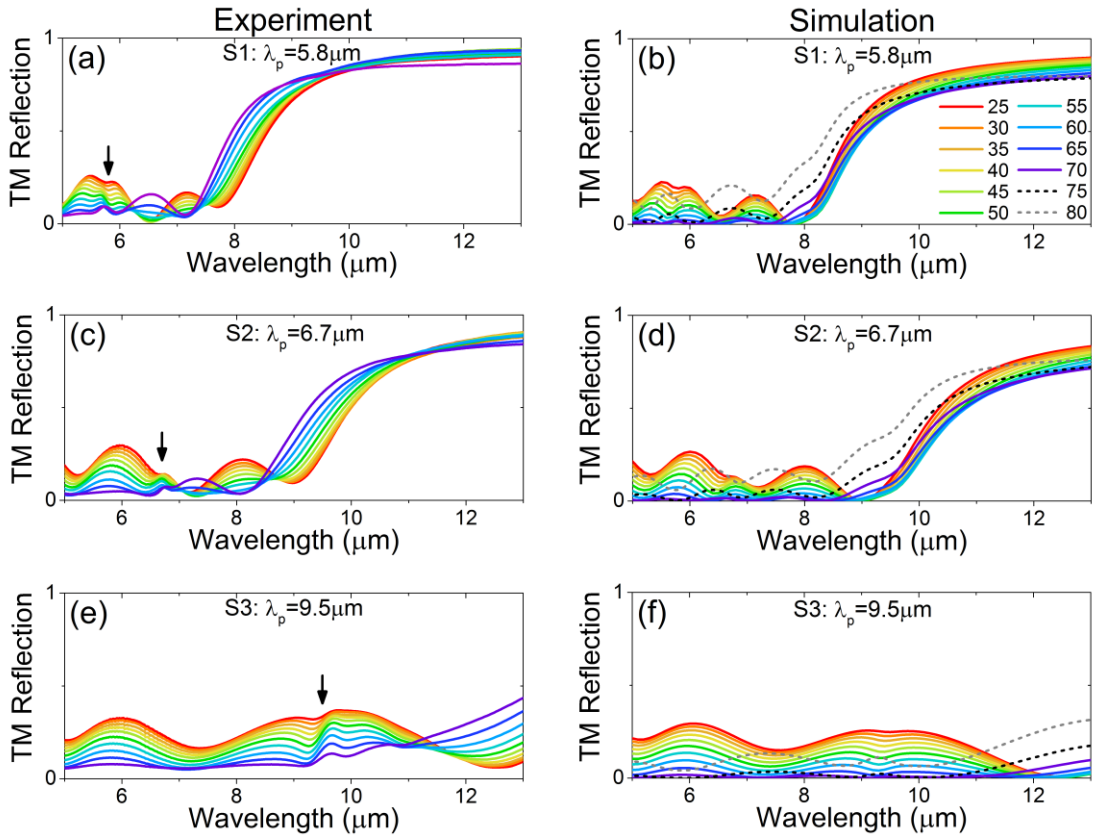

Figure 3.4: Experimental TM reflection for samples with plasma wavelengths 5.8μm (a), 6.7μm (c), and 9.5μm (e) for various angles, as indicated in the legend. For all samples, the fill factor is ~0.5. Simulated TM reflection using EMT for samples with plasma wavelengths 5.8μm (b), 6.7μm (d), and 9.5μm (f). Arrows indicate plasma wavelength. Dotted lines are simulated reflection data that are not shown on the experimental plots due to the inaccessibly high angle [97]. Reprint permission obtained from The Optical Society.

The optical properties of Sample 1, 2, 3 can be explained by looking at the permittivity extracted from the EMT as shown in Figure 3.5. The gray area where $\varepsilon_{\perp} < 0$ while $\varepsilon_{\parallel} > 0$ is the Type I HMM region and it starts at the plasma wavelength where $\varepsilon_{\perp}$ transits from positive to negative. When we move the plasma wavelength to a longer wavelength, the Type I HMM region shifts to longer wavelength accordingly.

This indicates that we can design the HMM working wavelength across the infrared by adjusting the doping level in the metal layer. We extracted the bandwidth in micron of Type I HMM region by measuring the width of the gray area for all samples as shown in Table 1. The bandwidth percentage is calculated by normalizing the bandwidth to the central wavelength. For the samples of similar fill fractions (Sample 1, 2, 3), the bandwidth is close to each other varying from 25% to 30%. At long wavelength, the $\varepsilon_{\perp}$ become positive while $\varepsilon_{\parallel}$ become negative, resulting in a Type II HMM region.

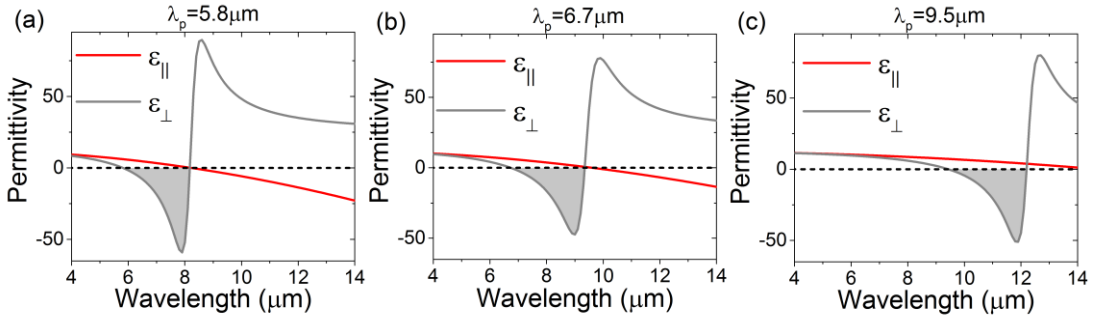

Figure 3.5: Parallel (red) and perpendicular (gray) permittivity for samples with plasma wavelengths 5.8μm (a), 6.7μm (b), and 9.5μm (c). Gray shaded region indicates HMM behavior [97]. Reprint permission obtained from The Optical Society.

We now turn to the samples which have similar plasma wavelength but varying fill fractions (Sample 3: 0.44, Sample 4: 0.24, Sample 5: 0.74). Figure 3.6 shows the experimental and simulated TM reflection of these three samples. Again, an absorption around the plasma wavelength and Fabry-Perot interference are observed for all three samples at a short wavelength range. However, they behave dramatically different at long wavelengths. For Sample 4 (fill fraction=0.24), the reflectivity

continues to be around 30% out to 18μm. For Sample 3 (fill fraction=0.44), the reflectivity gradually reaches 1 after plasma wavelength. For Sample 5 (fill fraction=0.74), there is a sharp increase in the reflection amplitude after the plasma wavelength. We can understand this difference by considering the effective parallel and effective perpendicular components of the permittivity plotted in Figure 3.7. For Sample 4, the bandwidth of Type I hyperbolic metamaterial behavior is only 10%. After this region, both $\varepsilon_{\parallel}$ and $\varepsilon_{\perp}$ are positive indicating a dielectric behavior with reflection amplitude below 50%. Sample 5 also exhibits a narrow bandwidth of 14%. Both components of permittivity become negative after the gray area. This results in a metallic behavior with reflection amplitude near 1. For Sample 3, whose fill fraction is 0.44, the $\varepsilon_{\parallel}$ become negative while $\varepsilon_{\perp}$ stays positive resulting in a type II HMM behavior. It also has the largest bandwidth percentage of around 25%. These data indicate that the optical properties of single material HMM at long wavelength are designer by fine adjusting the fill fraction. Another important conclusion is that the sample with 0.5 fill fraction has the largest bandwidth percentage. To our best knowledge, this is the first experimental demonstration of the effect of fill fraction on HMM behavior.

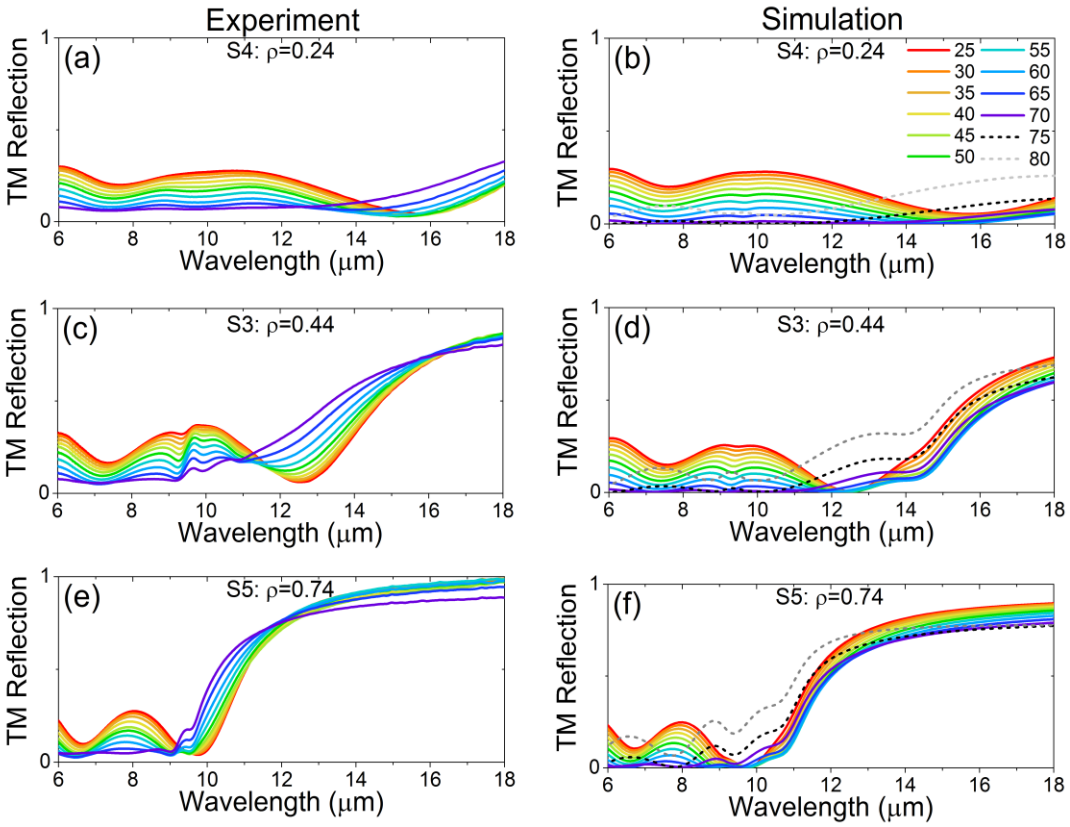

Figure 3.6: Experimental TM reflection for Sample 4 (a), Sample 3 (c), and Sample 5 (e) for various angles, as indicated in the legend. For all samples, plasma wavelength is ~9.5μm. Simulated TM reflection using EMT for Sample 4 (b), Sample 3 (d), and Sample 5 (f). Dotted lines are simulated reflection data that are not shown on the experimental plots due to the inaccessibly high angle [97]. Reprint permission obtained from The Optical Society.

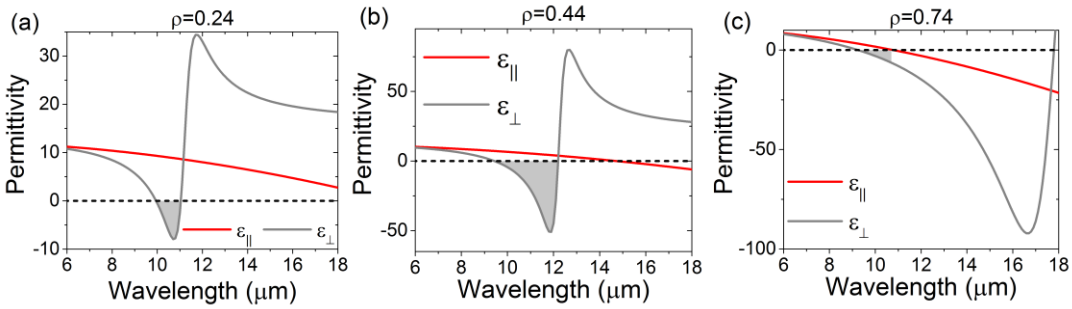

Figure 3.7: Parallel (red) and perpendicular (gray) permittivity for Sample 4 (a), Sample 3 (b), and Sample 5 (c). Note the different y-axis scales. Gray region indicates HMM behavior [97]. Reprint permission obtained from The Optical Society.

When comparing the experimental data to simulated data, we found that, though they match well, there are a few discrepancies. First, EMT predicts a feature at a longer wavelength (for example, Figure 3.6 (f) at 11μm), but we are not observing this feature in our experimental data. Second, the EMT doesn't work well at high reflection angles. To explain these discrepancies, we need to be aware that EMT doesn't consider the details of the layered structure. It only considers the properties of each layer and the ratio of the metal layer to the dielectric layer. Two structures with a 200nm period and 400nm period are considered the same using EMT. In addition, EMT is known to break down at higher angles [98–100]. We used COMSOL to simulate the reflection with consideration of the details of these structures as shown in Figure 3.8 and Figure 3.9. Simulation from COMSOL matches the experimental data much better than EMT.

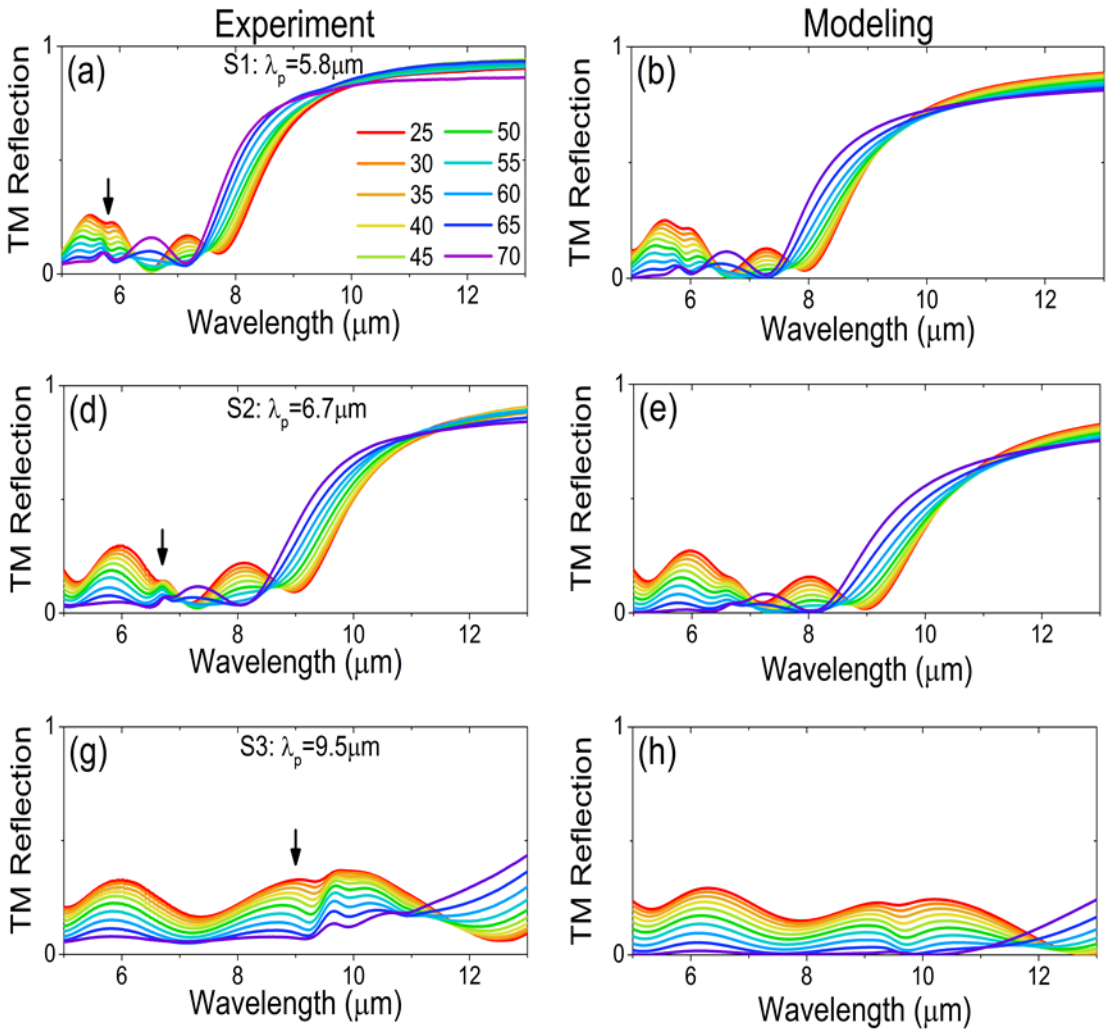

Figure 3.8: Experimental TM reflection for samples with plasma wavelengths 5.8μm (a), 6.7μm (c), and 9.5μm (e) for various angles, as indicated in the legend. For all samples, the fill factor is ~0.5. Simulated TM reflection using COMSOL for samples with plasma wavelengths 5.8μm (b), 6.7μm (d), and 9.5μm (f). Arrows indicate plasma wavelength.

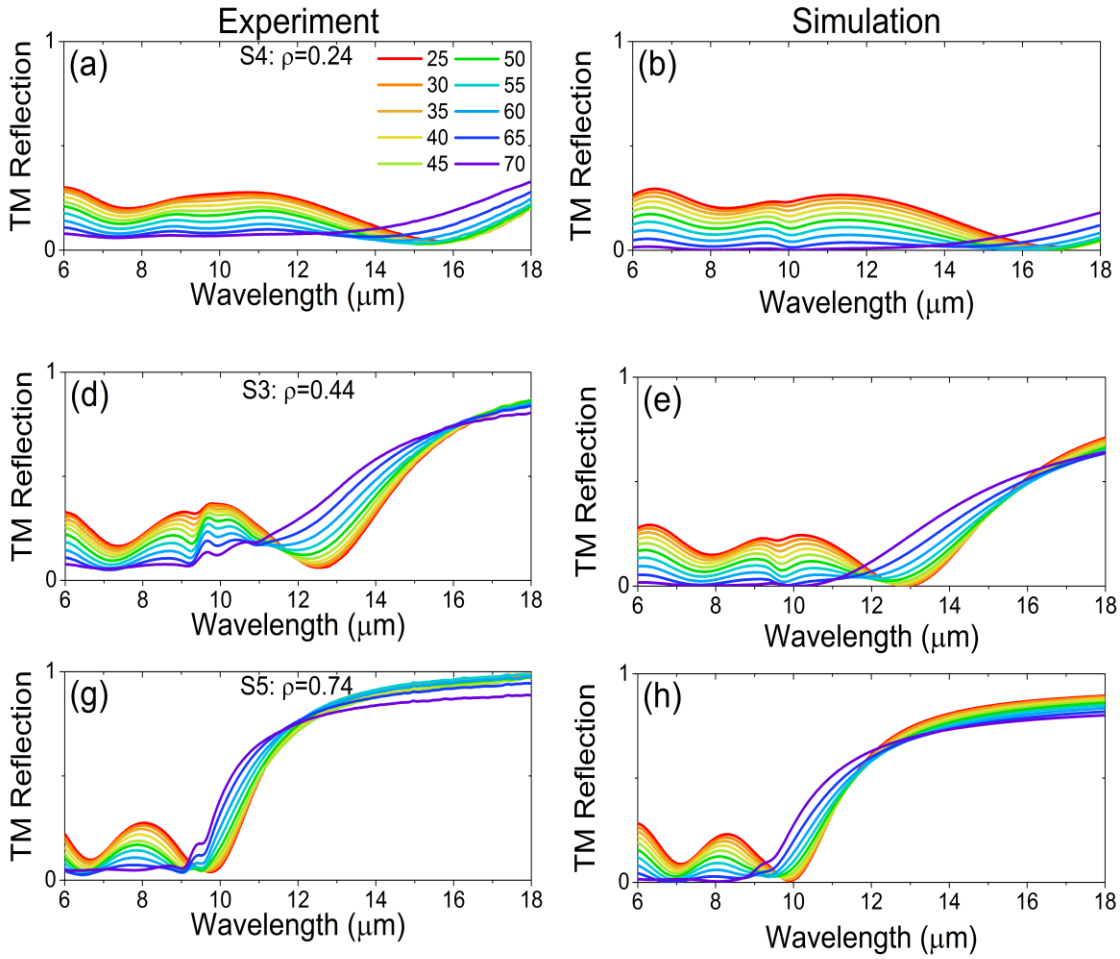

Figure 3.9: Experimental TM reflection for Sample 4 (a), Sample 3 (c), and Sample 5 (e) for various angles, as indicated in the legend. For all samples, plasma wavelength is ~9.5μm. Simulated TM reflection using COMSOL for Sample 4 (b), Sample 3 (d), and Sample 5 (f).

3.4 Discontinuity of the Brewster Angle

When light is incident from one medium to another medium, the reflection and transmission coefficients are determined by the polarization of the incident light, incident angle and the refractive index of two media. Figure 3.10 plots the reflection coefficient for TM and TE polarized light as a function of incident angle. Here, we

assume light is incident from the air (refractive index = 1) to a medium with a refractive index at 3.3, a typical value for semiconductor. For TM polarized light, the reflection coefficient gradually decreases to zero then increases until it approaches unity. The angle where the reflection coefficient reaches 0 is called the Brewster angle. Unlike TM polarized light, TE reflection doesn't exhibit a Brewster angle.

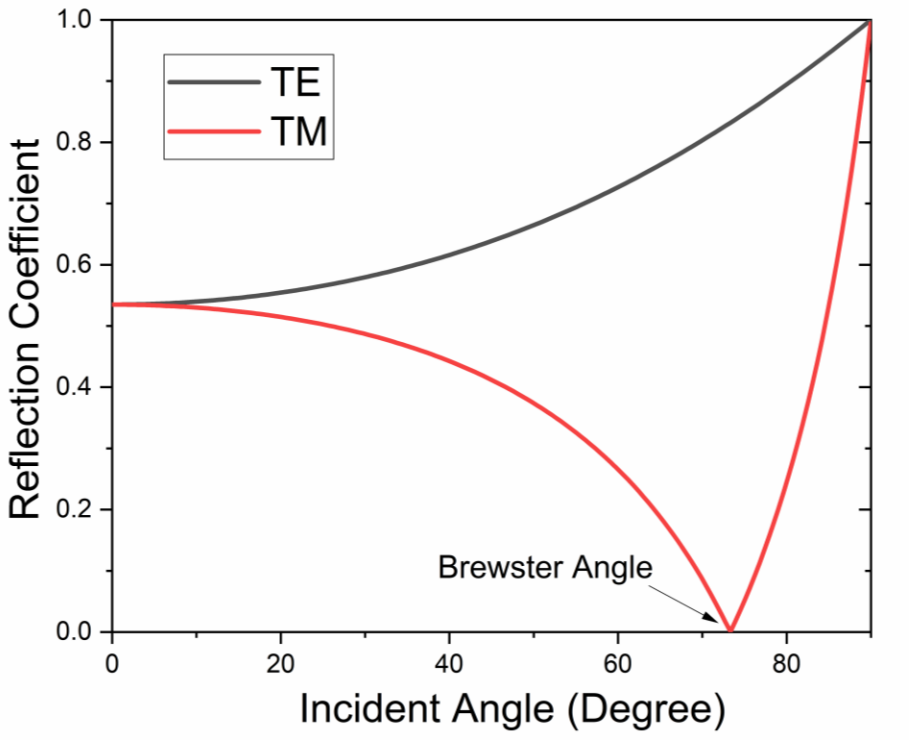

Figure 3.10: TM and TE reflection coefficient as a function of Incident angle, assuming light incident from the air (refractive index = 1) to a medium with refraction index at 3.3, a typical value for semiconductor.

The Brewster angle can be calculated as follows:

$$\theta_B = Arctan\left(\frac{n_2}{n_1}\right) \qquad \text{(Equation 3.1)}$$

Where θ_B is the Brewster angle while $\boldsymbol{n}_1$ and $\boldsymbol{n}_2$ are the refraction index of the two media.

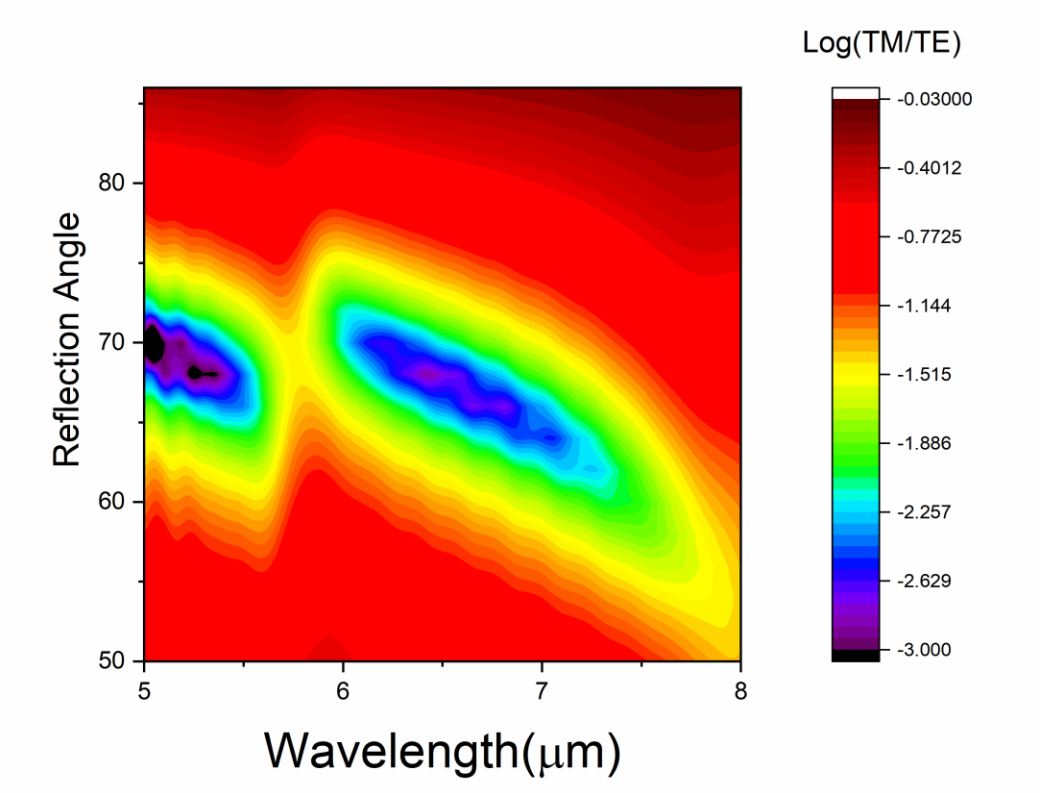

Figure 3.11: Log (TM/TE) reflection simulation of a thick HMM with plasma wavelength at 5.8μm. The thickness is assumed to be 15μm. There is a discontinuity of the Brewster angle at 5.8μm.

For HMM, the $\varepsilon_\perp$ changes from positive to negative at plasma wavelength while parallel permittivity stays positive. The dispersion changes from normal dispersion (described by a sphere) to hyperbolic dispersion. This results in the discontinuity of the Brewster angle. Discontinuity of the Brewster angle is the characteristic feature of an extremely anisotropic material. We won't observe this

phenomenon for an isotropic doped semiconductor at the plasma wavelength as demonstrated by other people in [7]. In Figure 3.11, I simulated the reflection of an HMM as a function of wavelength as well as reflection angles ranging from 50 to 80 degrees. As we have seen in Section 3.4, TE doesn't exhibit any HMM specific features as well as the Brewster angle (Figure 3.10), so it is a good reference. The figure plots TM/TE to cancel out the same features in both TM and TE spectrums and only focuses on the unique features for TM polarized light. The plasma wavelength is set to be 5.8μm which is the same as Sample 1. To reduce the effect of Fabry-Perot interference, we assume the thickness of HMM to be 15μm, much thicker than our samples. In Figure 3.11, the darkest area corresponds to the Brewster angle for a specific wavelength. There is a clear discontinuity around 5.8μm. Figure 3.12 is the experimental TM reflection of Sample 1. It is difficult to directly observe the discontinuity of Brewster due to the disturbance of Fabry-Perot interference (Figure 3.12 (a)). I made a color plot similar to Figure 3.11 as shown in Figure 3.12 (b). A discontinuity is present around the plasma wavelength. This demonstrates the characteristic HMM behavior in our single material HMMs.

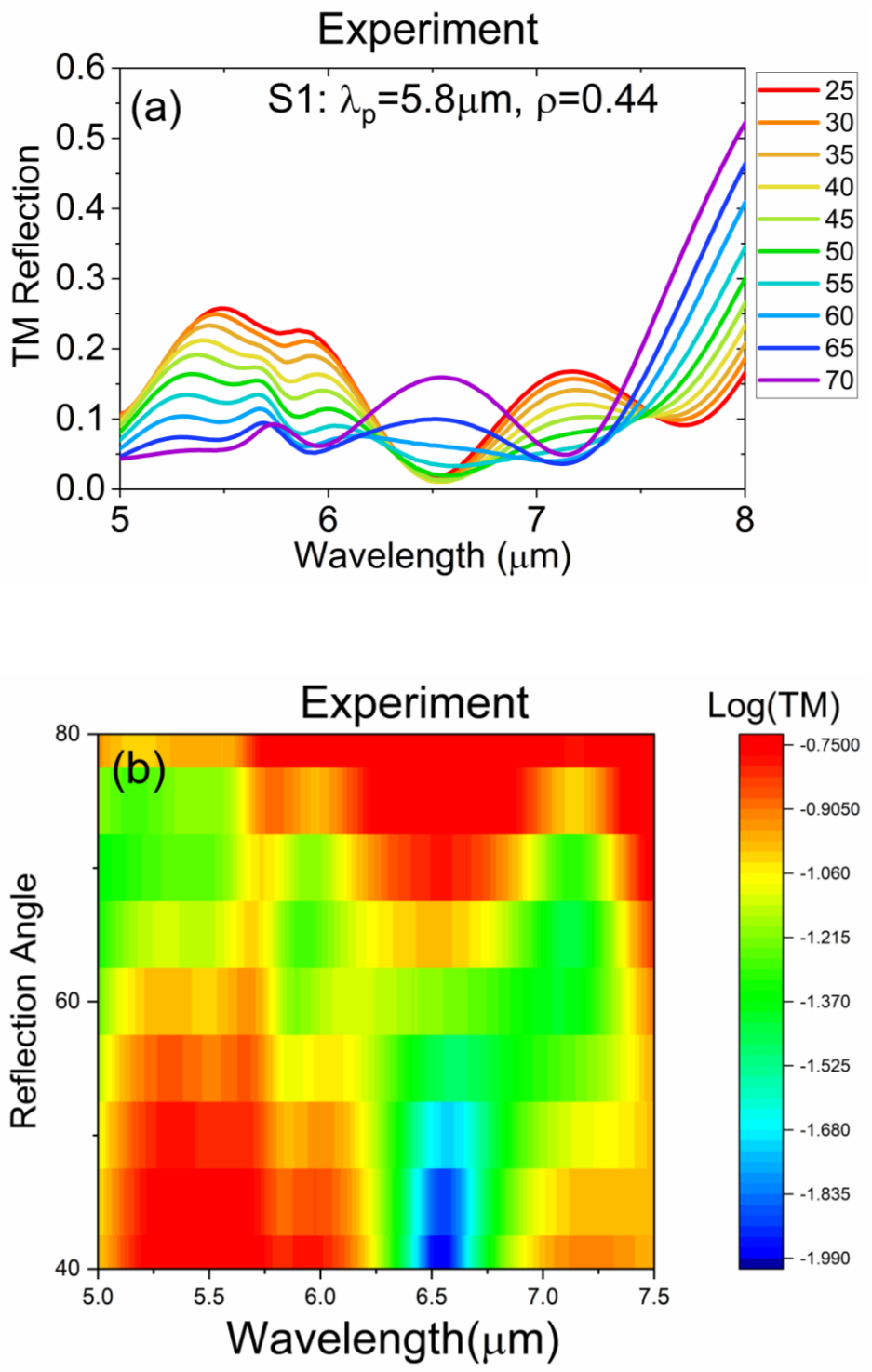

Figure 3.12: (a) Experimental TM reflection of sample 1 plotted in a line plot. (b) Experimental TM reflection of sample 1 plotted in a color plot.

3.5 Negative Refraction

Negative refraction is one of the most interesting properties of metamaterials. It demonstrates the ability of metamaterials to bend the light backward. The first negative refraction experiment was carried out by D.R. Smith et al. [34,37] using a structure based on split-ring resonators. The structures achieve negative refraction through the overlapping of electric and magnetic resonances, resulting in a material with simultaneously negative permittivity and permeability. However, such resonances are accompanied by high losses inside the structures which can limit their practical applications. Additionally, such structures require fabrication on a small scale. Existing fabrication technologies are not able to scale down the feature size of such devices to achieve shorter wavelength ranges. It requires sub-100nm resolution when we deal with the metamaterials working in infrared or visible ranges.

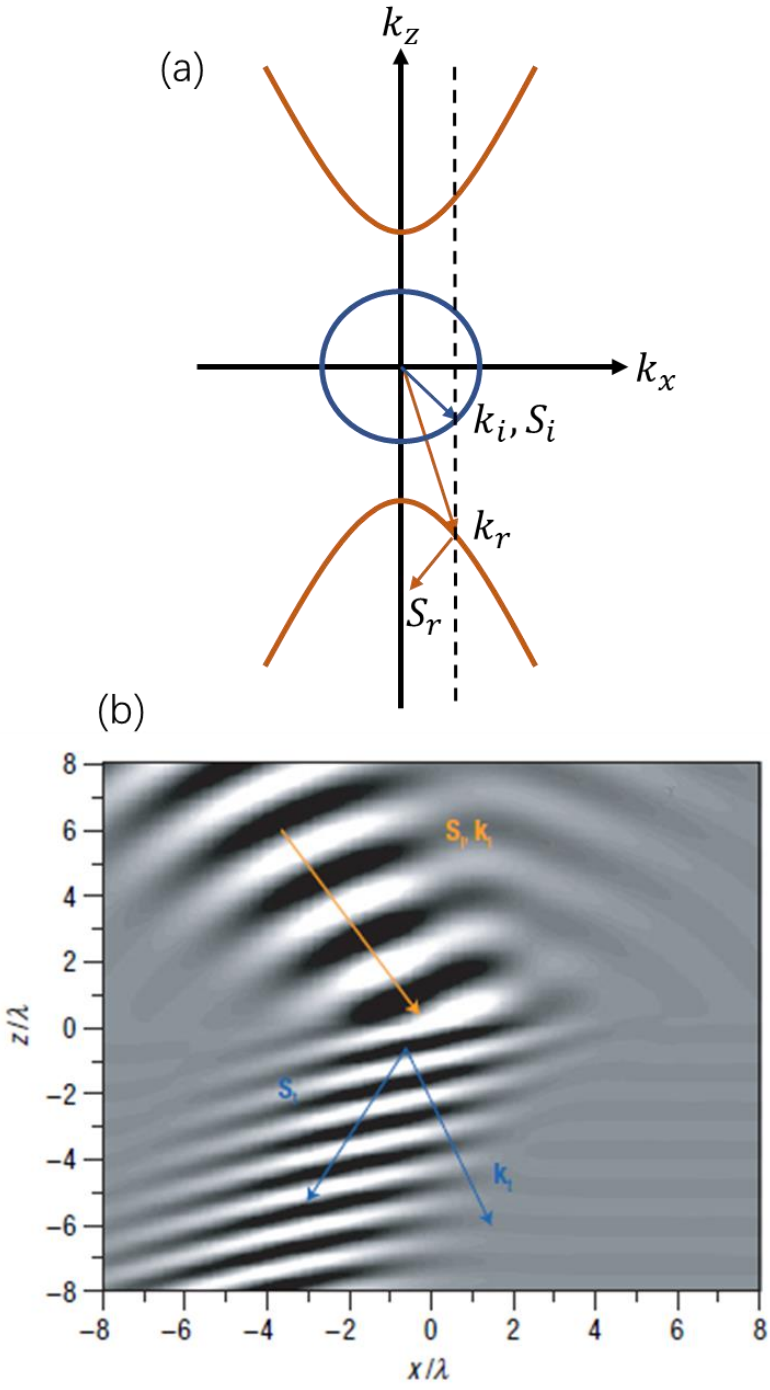
(a)
k_z
k_x
k_i, S_i
k_r
S_r
(b)
S_i, k_i
S_r
k_r
z/λ
x/λ
8
6
4
2
0
−2
−4
−6
−8
−8
−6
−4
−2
0
2
4
6
8

Figure 3.13: (a) Isofrequency surface of isotropic material and a Type I hyperbolic metamaterials, indicating how light transmits through an isotropic/HMM surface. (b) Numerical calculations demonstrating the negative refraction of layered HMMs composed of Si:InGaAs/InAlAs [7]. Reprint permission obtained from Springer Nature.

HMM overcome these shortages by only having negative permittivity in one direction and simpler design. We can deduct the negative refraction of HMM from the isofrequency surface. Isofrequency surface is a surface defined by the Maxwell equation in k-space. Only the wavevectors on the isofrequency surface can propagate inside a specific material at a given frequency. Figure 3.13 (a) shows the isofrequency surfaces of a normal isotropic material and a Type I HMM. For isotropic normal material, the wavevector (**k**) and energy flow (Poynting vector, **S**) are parallel to each other. But this is not necessary for an anisotropic material. When TM polarized light incident from normal material to Type I HMM, the wavevector undergoes positive refraction, while the energy flow is negatively refracted because it has to be normal to the isofrequency surface. For Type II HMM, negative refraction is not going to happen in the perpendicular direction (k_z direction in Figure 3.13 (a)) but the parallel direction (k_x direction in Figure 3.13 (a)).

To demonstrate the negative refraction of our material, we carried out a negative refraction experiment similar to [7]. The details of the setup are shown in Figure 3.2. We first collected standard transmissions with a full beam for both polarizations. The transmission angle is set at 30 degrees. Then we use a blade to block half of the transmitted light from the sample in four different directions (right, left, bottom, top). We then calculated the ratio of blocked transmission to standard transmission as shown in Figure 3.14 (b) and (c). When negative refraction happens,

the light will bend to the opposite direction of the normal refraction as shown in Figure 3.14 (a), resulting in a peak in the ratio when we block the light from left (orange line in Figure 3.14 (c)). In contrast, we could see a dip at the same position when we blocked the light from the right (blue line in Figure 3.14 (c)). Since the negative refraction only exists in the horizontal plane for this setup, we won't see any negative refraction features when we blocked the light from bottom or top directions (pink and black line in Figure 3.14 (c)). For TE polarized light whose electrical field is parallel to the layers and thus only affected by $\varepsilon_{\parallel}$, there is no peak or dip features around the plasma wavelength, but a monotonically increasing or decreasing signal caused by the wavelength-dependent refractive index of the material (Figure 3.14 (b)).

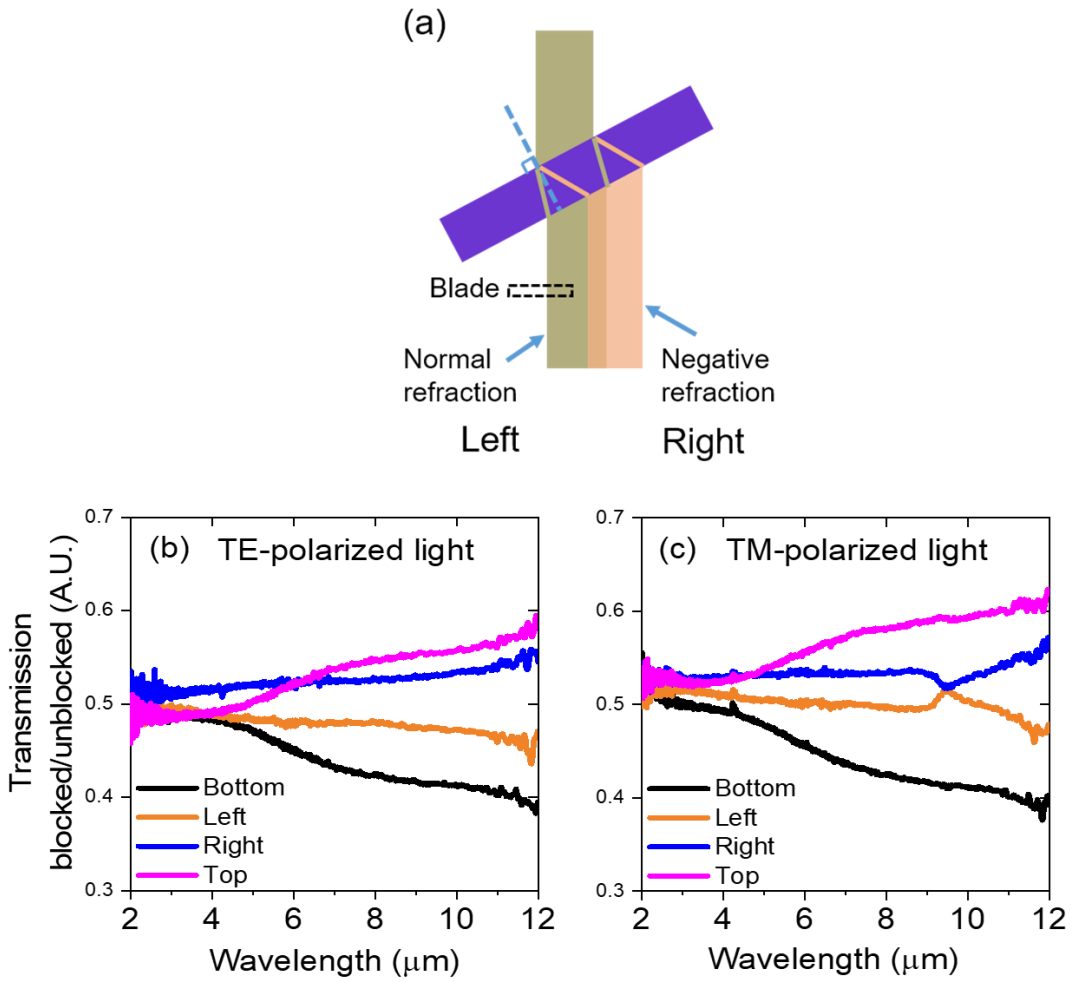

Figure 3.14: (a) Schematic of the negative refraction measurement setup. When negative refraction occurs, the beam shifts to the right with respect to normal refraction [97]. Reprint permission obtained from The Optical Society. (b) and (c) are negative refraction data for sample 5 (b) Negative refraction data for TE-polarized light with blade blocking the light from the bottom, left, right and top directions. (c) Negative refraction data for TM-polarized light with blade blocking the light from the bottom, left, right and top directions. There is a dip when cover half of the light from the right and a peak when cover half of the light from the left.

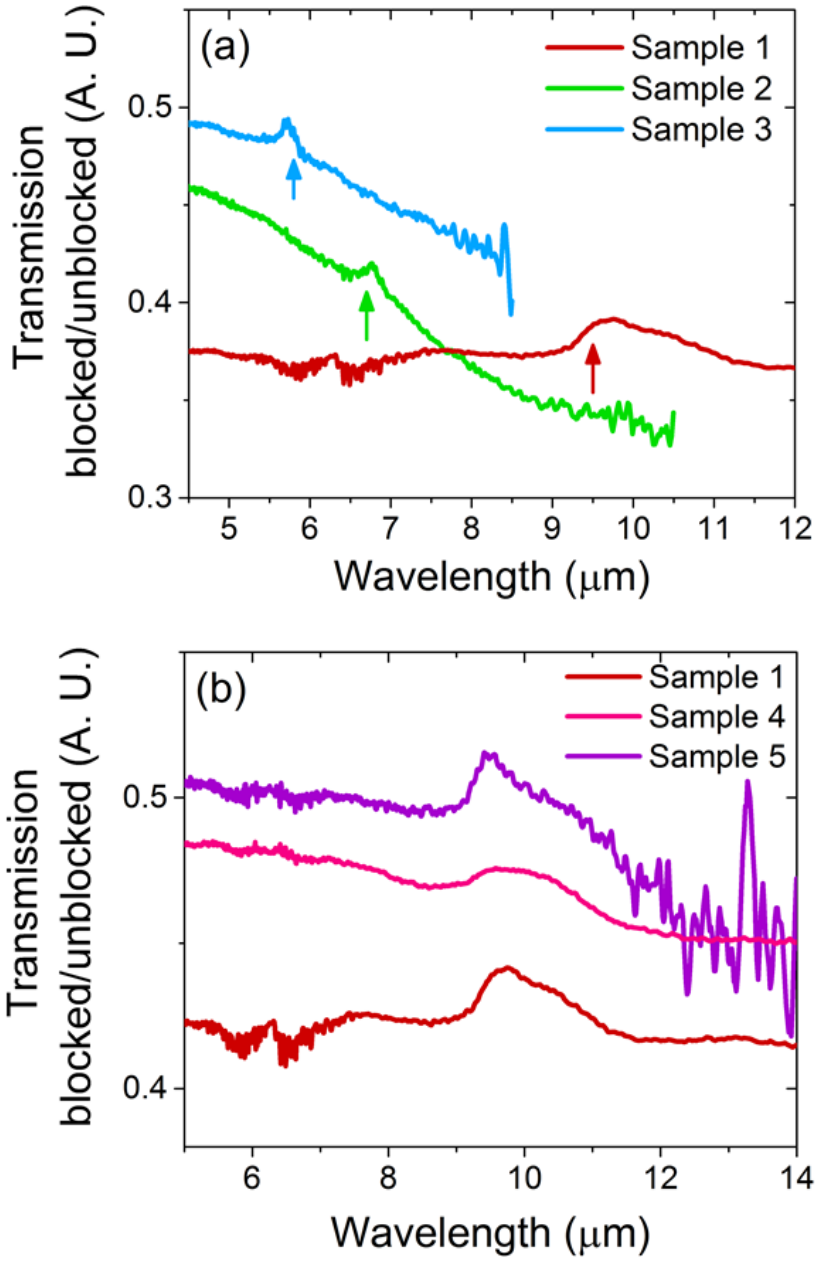

Figure 3.15: (a) Negative refraction data for TM-polarized light with the blade in the left position for Sample 1,2,3. Arrows indicate the plasma wavelength. (b) Negative refraction data for TM-polarized light with the blade in the left position for Sample 1,4,5 (same plasma wavelength). Data was shifted vertically for visual clarity [97]. Reprint Permission obtained from The Optical Society.

In Figure 3.15, we plot the negative refraction data (blade cover from left) for all samples. Figure 3.15 (a) is the data for samples with different plasma wavelength. Negative refraction is observed at the corresponding plasma wavelength as what we expected. For samples with the plasma wavelength held near to 9.5μm (Figure 3.15 (b)), a peak from negative refraction is observed at the same position (9.5μm). The negative refraction data strongly demonstrate that our materials act like designer HMMs.

3.6 Conclusion

We fabricated single material HMMs using InAs who has a small effective mass and offers the smallest plasma wavelength among III/V material. This is the first demonstration of the HMM in a single material system. The growth of a single material system is easy and straightforward using techniques like MBE. We demonstrated the design flexibility of our materials by exploring the reflection and transmission properties of samples with different fill fractions (0.25-0.75) and plasma wavelength (5.8μm-9.5μm). Our material could work down to 5.8μm by adjusting the doping level in metal layers. In addition, the long wavelength response could exhibit metallic, dielectric or Type II HMM behavior by adjusting the filling ratio ρ. We also demonstrated the discontinuity of the Brewster angle and the negative refraction, two characteristic features of HMM, in the infrared range. The fabrication of single material HMMs could lead to applications in subwavelength imaging, high sensitivity detector, and enhanced emission. It opens up the possibility of fabricating HMM in a simpler way.

Chapter 4

VOLUME PLASMON POLARITONS IN LAYERED HYPERBOLIC METAMATERIALS

4.1 Background of Volume Plasmon Polariton (VPP) modes

An important feature of HMMs is that they could support electromagnetic modes with large wavevectors (see Figure 4.1). Such modes are forbidden in conventional media but become propagating in HMMs that have extreme anisotropy [19,47,101–105]. These modes have several names: high-k modes, bulk plasmon polaritons, volume plasmon polaritons (VPPs). Throughout this dissertation, they are called VPP modes.

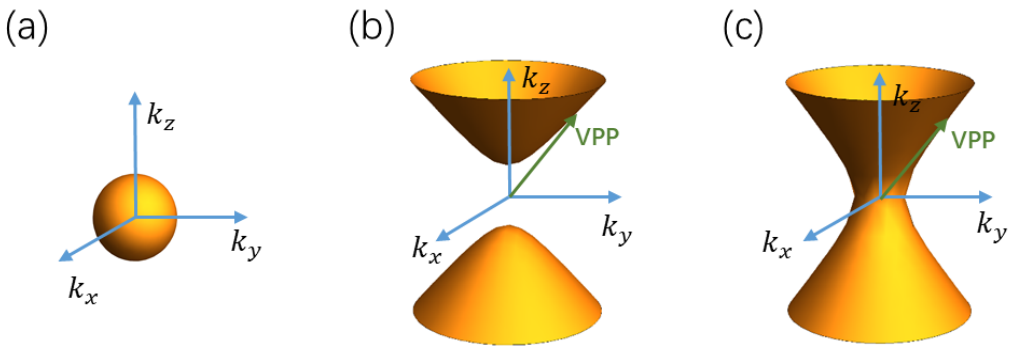

Figure 4.1: (a) Normal isotropic materials; (b) Type I HMMs: $\varepsilon_\perp < 0, \varepsilon_\parallel > 0$; (c) Type II HMMs: $\varepsilon_\perp > 0, \varepsilon_\parallel < 0$; The green arrows indicate the VPP modes.

Many proposed HMM-based applications are based on VPP modes. For example, far-field super-resolution imaging based on a curved HMM structure [73] (see Figure 4.2). In normal materials, these modes are evanescent since their wavevectors are outside the isofrequency surface. In HMMs, the unique hyperbolic dispersion enables the propagation of high-wavevector components through the excitation of VPP modes. In this structure, evanescent waves that carry subwavelength structure information propagate along the radial direction and could be received by a detector placed in the far-field.

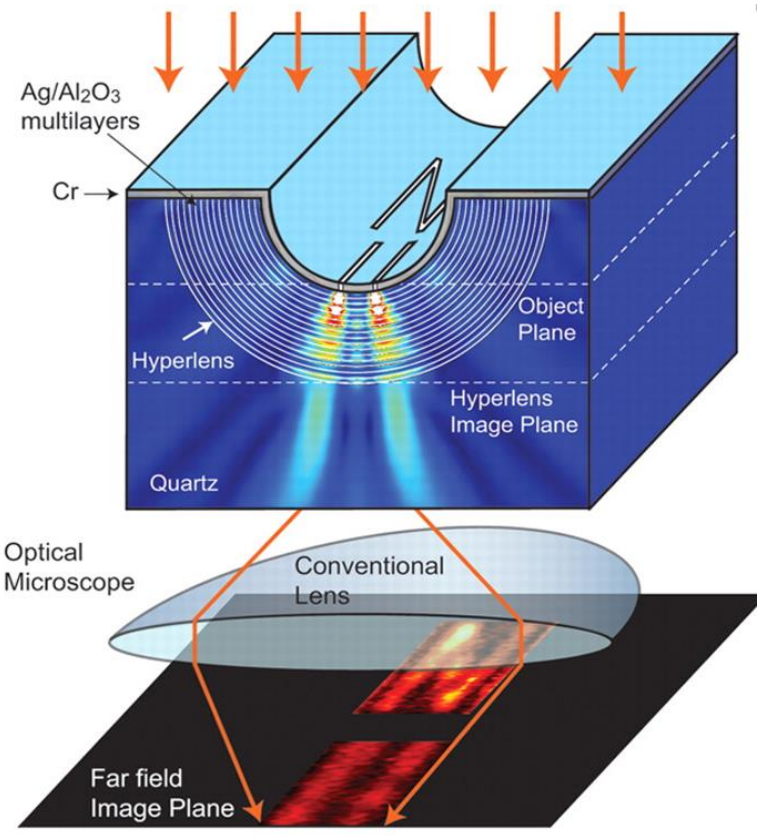

Figure 4.2: Schematic of hyperlens and numerical simulation of imaging of sub-diffraction-limited objects [64]. Reprint permission obtained from the American Association for the Advancement of Science.

Another example is strong coupling [84]. VPP modes are highly confined modes with large mode index, indicating a strengthened electromagnetic field in a small volume. The strong coupling between VPP modes and other resonance (such as quantum well intersubband transitions (ISBT), see Figure 4.3) could lead to the realization of more efficient quantum well infrared photodetectors and tunable intersubband light-emitting devices.

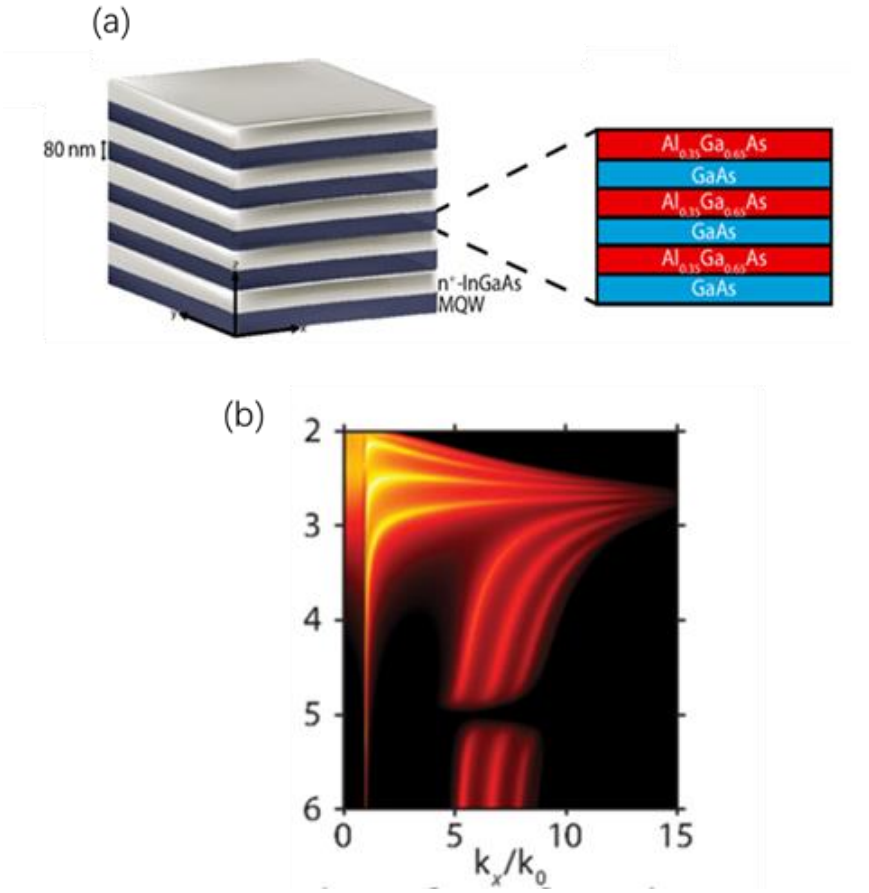

Figure 4.3: (a) Multilayer realization of a semiconductor HMM. The structure consists of alternating 80-nm-thick subwavelength layers of a dielectric MQW slab and degenerately doped As. The extreme anisotropy of the structure results in a hyperbolic isofrequency surface. (b) Strong coupling between the ISBT and type-II modes of the multilayer structure at λ_{ISBT}=5μm. A series of high-k-ISBT polaritons are formed [84]. Reprint permission obtained from the American Physical Society.

To understand the origin of VPP modes, we need to start from the surface plasmon polaritons (SPPs). Polariton is the result of strong coupling between photons and other electric dipoles [106,107]. When a vibration in a medium shares the same frequency of incident electromagnetic waves, they resonate. Near the resonance

frequency where the two dispersion curves meet, there is going to be a splitting leading to an ‘upper’ and a ‘lower’ mode since two resonances with the same frequencies are not allowed in the same system. This is also called anti-crossing and the splitting gap depends on the strength of coupling. In other words, polaritons are mixed modes of light mode and medium mode. Surface plasmon polariton is the coupling between electromagnetic waves and surface plasmons at a metal/dielectric interface (see Figure 4.4) [106]. The existence of SPPs can be deduced from the Maxwell equation. It only exists for TM polarized light. From Figure 4.4 (c), we can find that SPPs have a larger wavevector than light at the same frequency, indicating stronger spatial confinement and higher local field intensity. In the direction perpendicular to the surface, the penetration depth of SPP fields is determined by the refractive index of the two media (Figure 4.4 (b)). Most of the time, the SPP field is confined to a subwavelength scale in the perpendicular direction.

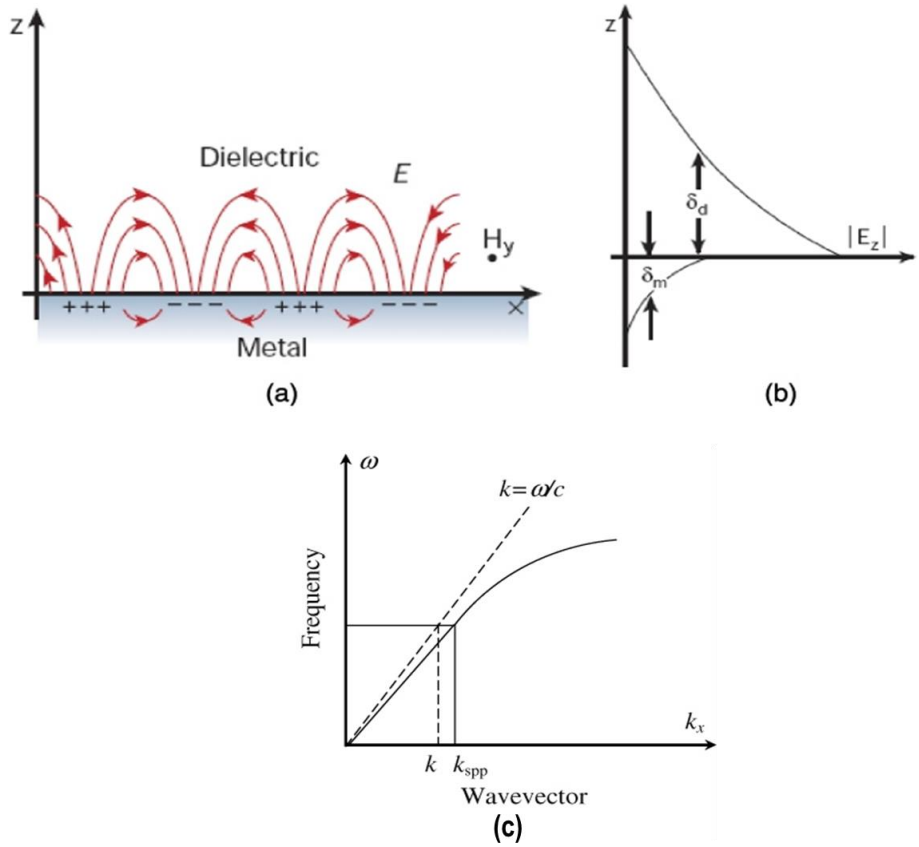

Figure 4.4: (a) Schematic illustration of electromagnetic wave and surface charges at the interface between the metal and the dielectric material, (b) the locally electric field component is enhanced near the surface and decay exponentially with distance in a direction normal to the interface. (c) Dispersion curve of an SPP wave, k_{spp} and k are the SPP and free-space wavevectors, respectively, the momentum ($\hbar k_{spp}$) of the SPP wave is larger than that of the light in free space photon ($\hbar k$) for the same frequency (ω) [108]. Reprint permission obtained from IOP publishing.

The following equation determines the dispersion relation of SPPs:

$$\omega = \sqrt{\frac{\varepsilon_m + \varepsilon_d}{\varepsilon_m \varepsilon_d}}\, c k_x \qquad \text{Equation (4.1)}$$

where ω is the frequency, ε_m is the permittivity of the metal, ε_d is the permittivity of the dielectric, c is the speed of light in vacuum, and k_x is the wavevector along the x direction.

Now we turn to a little bit more complicated system: a dielectric layer sandwiched by two metallic layers (Figure 4.5). The structure supports four modes, two of which are surface modes. The other two modes are bulk modes propagating inside the dielectric gap. The bulk modes result from the coupling of surface modes when the gap between surface mode is sufficiently small. This is similar to the coupling of wavefunctions of two quantum wells. When quantum wells are brought very close to each other, the wavefunctions overlap with each other, resulting in new states, whose wavefunction can be expressed as linear combinations of original quantum well wave functions. In the sandwiched structure, the two bulk modes are the linear combinations of surface modes. The one with the antisymmetric magnetic field has a cut-off wavelength so it does not exist in nanoscale. In Figure 4.5, the cut-off for the antisymmetric mode is around 480nm. The other one with the symmetric magnetic field, called gap plasmon polariton (GPP), is the mode that contributes to the formation of VPP modes [19].

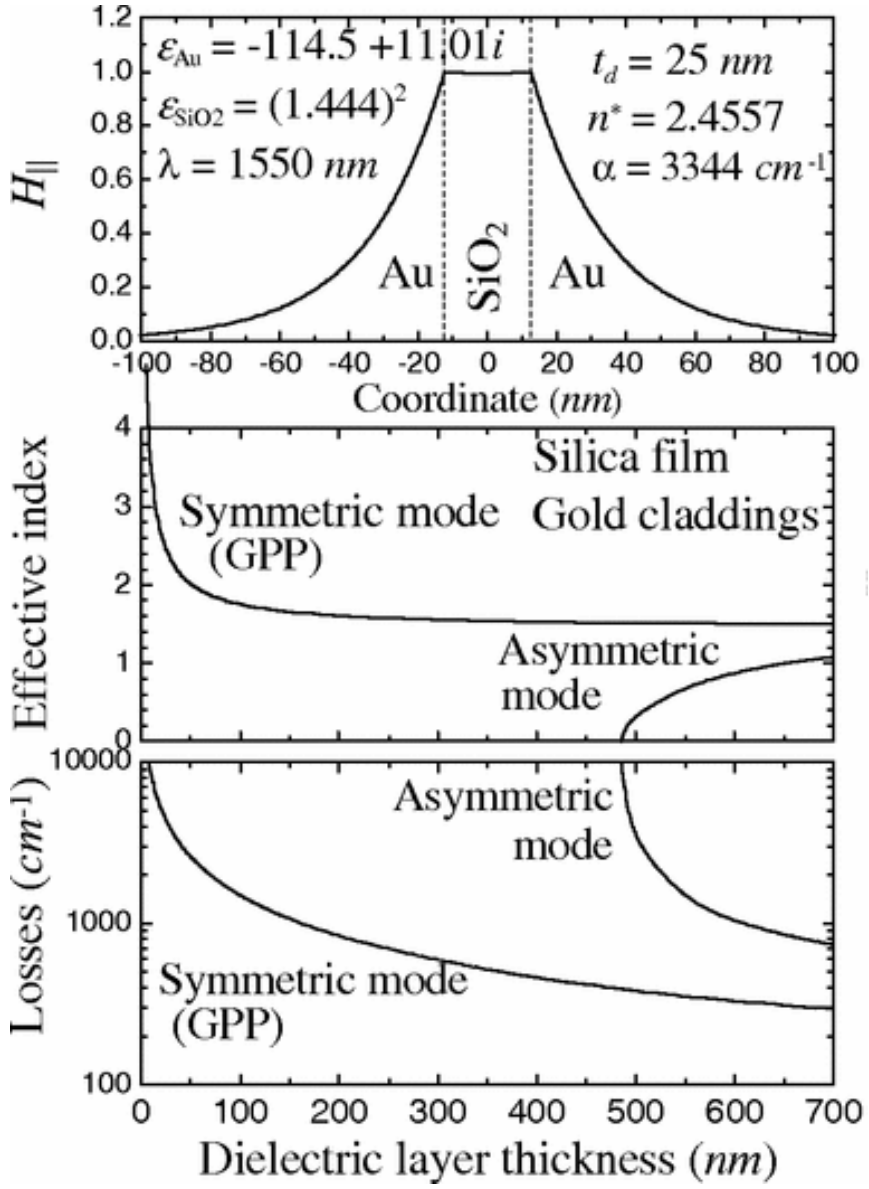

Figure 4.5: Field profile (strength of magnetic field versus coordinate across the structure) for a gap plasmon polariton and its modal index and losses as a function of the dielectric layer thickness [19]. Reprint permission obtained from the American Physical Society.

Finally, we arrive at a multilayer structure consisting of alternating metal and dielectric layers. We know that if a dielectric layer is sandwiched by two metallic

layers, there is going to be a GPP in the dielectric layer. In a multilayer structure, the GPPs in each dielectric layer repulse with each other, resulting in new modes that are highly confined in the bulk structure. The interaction between GPPs is similar to the coupling between multiple quantum wells. The coupling between quantum wells leads to the splitting in energy levels. Some energy levels are going to be higher than the original ones while others will be lower. The coupling between surface modes leads to the splitting in modal indices. Figure 4.6 (a) plots the splitting of modal indices of layered material with decreasing dielectric thicknesses. When the dielectric layer is thinner, the coupling between SPPs is stronger, leading to bigger splitting in modal indices. Higher mode indices indicate stronger field confinement. Figure 4.6 (b) is the magnetic field profiles of modes supported by a silica/gold multilayer structure. We could observe that the magnetic field is near zero outside the multilayer structure for higher order modes ($TM_2, TM_3, TM_4,$ and TM_5 in Figure 4.6 (b)), demonstrating that these modes are highly confined in the bulk. In addition, the number of nodes increases for modes with higher modal indices [19].

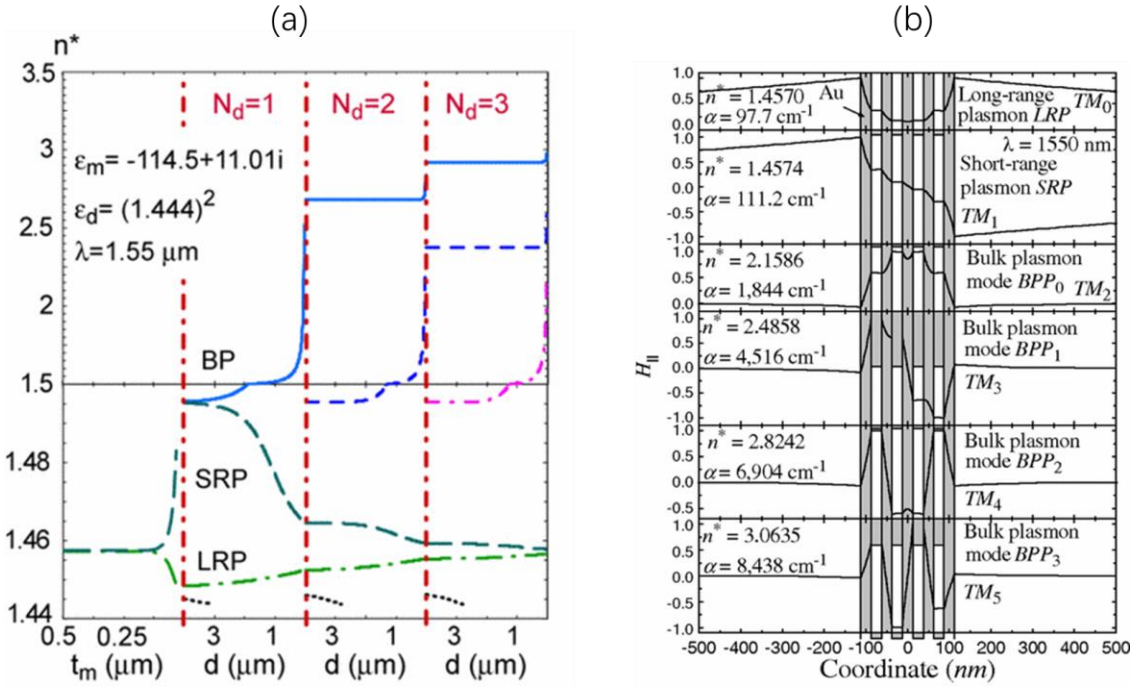

Figure 4.6: (a) Evolution of coupled SPP modal indices in the layered materials with dielectric claddings for $|\varepsilon_m| > |\varepsilon_d|$. First vertical portion of the figure illustrates the appearance of a SRP-LRP doublet as a result of splitting between two SPPs (left) and as a result of mode-antimode formation (right). Other vertical portions illustrate modal indices in a layered structure when a metal layer is being gradually brought closer to the nanolayer stack. (b) Profiles of modes supported by a nanoscale multilayer of four silica layers and five gold layers between silica claddings (right) [19]. Reprint permission obtained from the American Physical Society.

Highly confined VPP modes provide unprecedented opportunities for many HMM-based applications, such as hyperlens, superlens, enhanced sensors, and detectors. The systematic study of VPP modes not only helps us better understand how light interacts with matter in the HMMs but also lays a solid foundation for future applications based on HMMs. Several papers focus on the VPP modes for visible and near-IR using materials including Au, TiO_2, SiO_2, and Al_2O_3 [19,75,102,103,109].

However, these materials are not compatible with infrared, and it is challenging to integrate them with other III-V semiconductor optoelectronic components and devices, including quantum wells, quantum dots, quantum cascade lasers. In this project, we explored the VPP modes of semiconductor HMMs in the wavelength between 12μm to 30μm. We demonstrated high-quality VPP modes and investigated the factors that could affect their behaviors.

In this chapter, I am going to analyze the VPP modes from four different semiconductor HMMs samples: two Si:InAs/InAs HMMs (Sample 1 and Sample 3 in Chapter 3), Si:InGaAs/InAlAs HMM and Si:InAs/AlSb HMM. The structure details are described in Table 4.1. Section 4.2 will be talking about the experimental details of the growth and the fabrication of gold grating couplers. Section 4.3 discusses how we model samples with poor confinement of electrons. Section 4.4 analyzes the experimental data of Si:InAs samples. In Section 4.5, I compare the different behaviors of VPP modes in different material classes. Section 4.6 is the conclusion of this Chapter.

Table 4.1: Structure details of three HMMs created from different materials

Sample	$\frac{t_m}{t_m + t_d}$	$\lambda_p(\mu m)$
Si:InAs/InAs (Sample 1)	0.5	5.8
Si:InAs/InAs (Sample 3)	0.44	9.5
Si:InGaAs/InAlAs	0.5	8.4
Si:InAs/AlSb	0.47	8.5

4.2 Growth of the Samples and the Excitation of the VPP modes

The growth of Si:InAs/InAs HMMs is described in detail in Section 3.2. The growth of Si:InGaAs/InAlAs HMM is done by our collaborators, Stephanie Tomasolu and Michael Yakes, at Naval Research Lab. The sample was grown at InP:Fe substrate with oxide off temperature at around 550℃. The growth temperature is around 510℃. The growth of Si:InAs/AlSb HMM is done by Patrick Sohr at the University of Delaware. The sample was grown at undoped single side polished GaAs substrates. The de-oxidation process is described in detail in Section 3.2. After the de-oxidation process, the substrate temperature was brought down to 510℃ for the growth of a 500nm thick GaSb buffer layer. The growth temperature was then decreased to 450℃ for the growth of alternating Si:InAs and AlSb layers. For all the samples, the period is between 200 ~ 220nm and the number of periods is 10. The top layer is always the undoped dielectric layer. The dielectric layer on the top could better guide the light into the structure rather than reflecting them off the surface.

To excite the VPP modes, we fabricated gold grating couplers on top of the samples to match the momentum of the incident light and the momentum of VPPs. The relationship between wavevector and the period of the grating can be expressed as:

$$\frac{k_x}{k_0} = sin\theta + \frac{\lambda}{\Lambda} \qquad \text{Equation (4.2)}$$

where k_x is the wavevector in the HMM along the x direction (parallel to the layers), k_0 is the wavevector of the incident light, θ is the incident angle, λ is the wavelength of the incident light, Λ is the period of the grating. The fabrication process is described in Figure 4.7. We first deposited a bi-layer photoresist on the surface of the samples. The first layer is photoresist LOR 3A; the second layer is photoresist CSAR 6200.04.

The bi-layer photoresist will form an under-cut which enables an easier strip-off process. We used an e-beam writer to expose the photoresist, forming the grating pattern. Then the sample was developed in AR 600-546 for 60 seconds and AR 300-47 for 35 seconds respectively. The deposition of the gold was done in an e-beam evaporator (see Section 2.2.2). We first deposited a 15nm titanium following by a 100nm gold. The titanium layer is used to help gold stick to the surface. Then we stripped off the photoresist and unwanted metal layer in warm N-Methyl-2-pyrrolidone solutions. SEM and optical microscopy were used to confirm the grating period, grating profile, grating thickness, and stripe width (Figure 4.7 (b)).

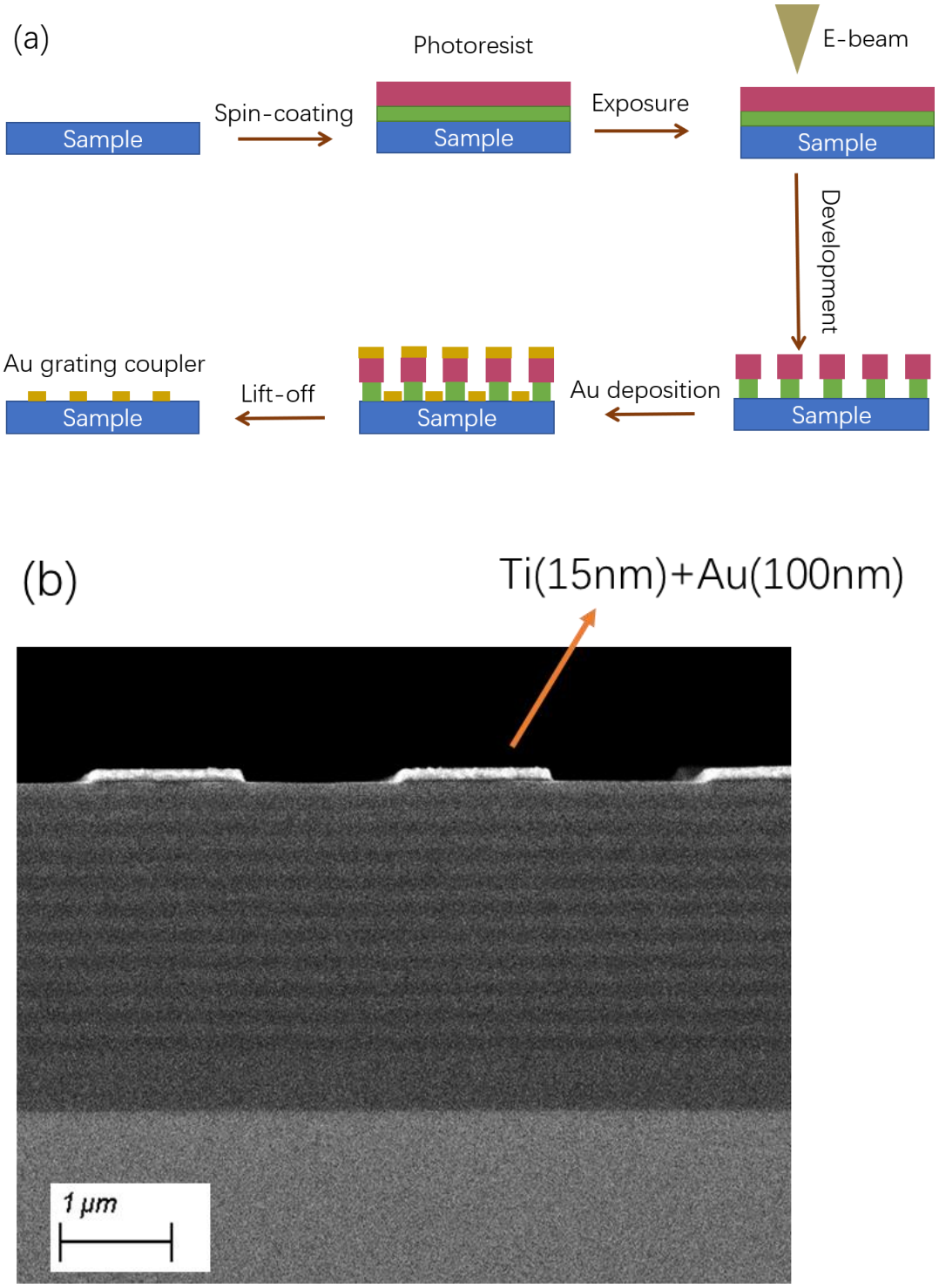

Figure 4.7: (a) Schematic of the e-beam lithography process, (b) Cross-sectional SEM of Si:InAs/InAs HMM with Ti/Au grating couplers.

We studied the optical properties of VPP by taking TM and TE polarized reflection using Bruker Vertex 70V Fourier transform infrared (FTIR) spectrometer. A wide-range DTGS detector, a KRS-5 holographic wire grid polarizer and a Pike 10spec accessory whose reflection angle is set to be 10 degrees were used to set up the measurement in the FTIR sample compartment. The reflection was corrected by a gold mirror whose reflection is assumed to be unity at infrared. The scan velocity was 2.5 kHz and the scan resolution was 2cm^{-1}.

4.3 Modeling of Si:InAs HMM VPP Modes

As discussed in Section 4.1, VPP modes in a multilayer HMM originate from the coupling of SPP modes at each metal/dielectric layer. As a result, the exact distribution shape of the electron could have a significant effect on the VPP modes. Ideally, we would like to have a sharp interface where all electrons are confined in the metal layer, leaving dielectric layers completely undoped. In this situation, the carrier density is a constant at the metal side, resulting in a sharp SPP resonance. If the electrons are not well confined in the metallic layer, the graded interface will lead to a depth-dependent carrier density, leading to broad and weak SPP resonance. This is the case for Si:InAs HMMs samples due to the lack of large conduction band offset to confine the electrons. For multilayer semiconductor structures, the distribution of the electron is determined by the conduction band offset. Figure 4.8 (a) plots the conduction band and the electron distribution of Si:InAs HMM as a function of sample depth calculated from a one-dimensional self-consistent Poisson solver (1D Poisson made freely available by G. Snider). The distribution of electrons is not a square-wave type function, with the graded area (area b) between doped (area a) and undoped layer (area c). To accurately model the optical properties of the graded area of Si:InAs

HMM, we need to find the relationship of doping density as a function of sample depth. We found the Boltzmann equation works well for our situation. The distribution of electron density can be described by the following equation [110]:

$$\mathrm{n(z)} = n_{max}\left(-0.5226 + \frac{1.5170}{1+\exp(\frac{z-225.5435}{38.8166})}\right) \qquad \text{Equation (4.3)}$$

Where n_{max} is the maximum doping density, z is the sample depth. For Sample 1, n_{max}=$7.35 \times 10^{19} cm^{-3}$ while for Sample 3 n_{max}=$1.25 \times 10^{19} cm^{-3}$. The above Boltzmann equation is merely a phenomenological fitting.

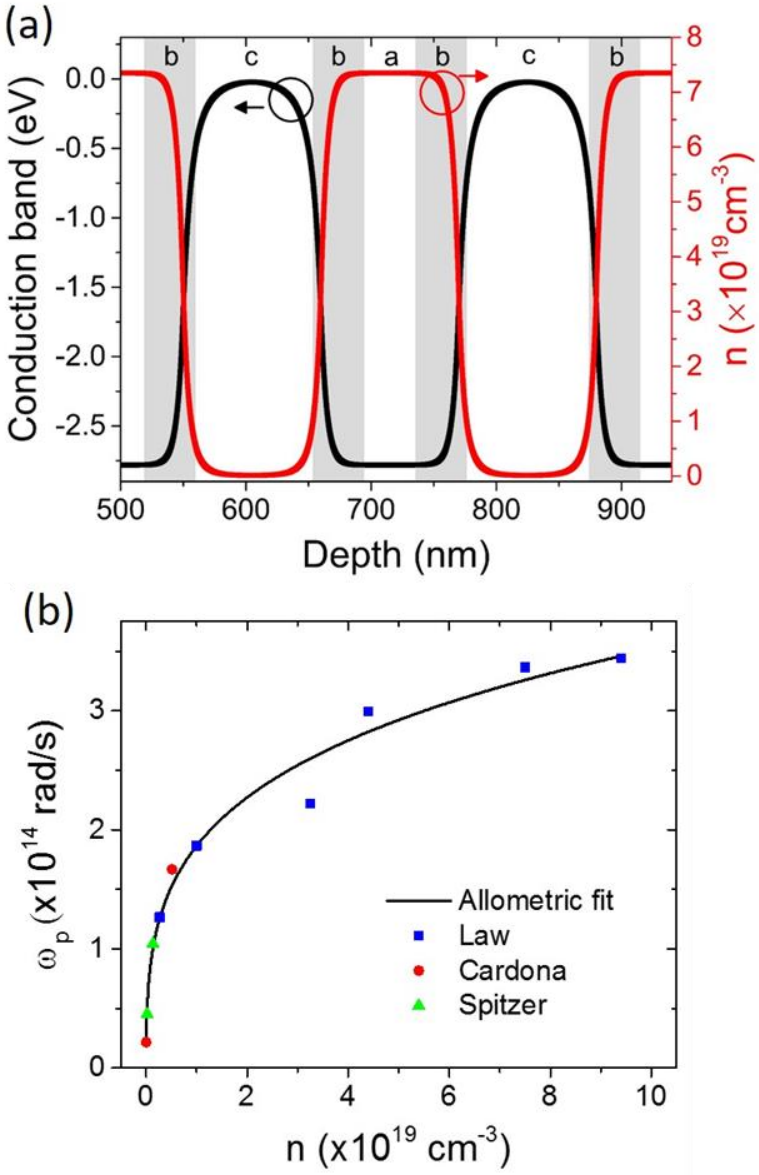

Figure 4.8: (a) Conduction band profile (black) and carrier density (red) in the Si:InAs/InAs superlattice from Sample 1 as calculated using a self-consistent Poisson solver. In region a, the material is modeled as a Drude metal with a constant carrier density, while in region c, the material is modeled as undoped InAs with a constant permittivity of 12.3. In the shaded region b, the carrier density depends on depth as described below. (b) Experimental (symbols) and empirical model (black line) for plasma frequency as a function of carrier density in doped InAs [111–113]. Reprint from [110] with permission from The Optical Society.

The next step is to find the relationship between the electron density and the plasma wavelength of Si:InAs. A simple Drude model couldn't be applied to this situation because the effective mass of InAs is highly non-parabolic, leading to a non-linear relationship between the plasma frequency and the doping density. We found multiple data points of Si:InAs from three references and plotted them in Figure 4.8 (b). We found the following equation fit the data points very well [110]:

$$\omega_p(n) = -4.5433 \times 10^{13} + 8.44 \times 10^{9} \times n^{0.23363} \quad \text{Equation (4.4)}$$

Where ω_p(rad/s) is the plasma frequency and n (cm^{-3}) is the doping density. We need to clarify that this equation is an empirical equation and can only apply to the sample with doping density between $5 \times 10^{16} \sim 1 \times 10^{20} cm^{-3}$. We then incorporated this equation as well as the distribution of electron doping density into COMSOL to simulate the TE and TM reflection of Sample 1 and Sample 3 with varying grating coupler periods.

4.4 VPP Modes in Si:InAs/InAs HMMs

We first look at the VPP modes in Si:InAs/InAs HMM. The two samples are Sample 1 and Sample 3 discussed in Chapter 3. They have similar fill fractions (~0.5) but different plasma wavelength (Sample 1 = 5.8μm, Sample 3 = 9.5μm). We fabricated gold grating couplers on the two samples with different periods varying from 1.8μm to 4.6μm. The procedure of fabricating the gold grating couplers are described in Section 2.2 and Section 4.2. TM and TE polarized reflections were collected by FTIR on these samples using the setup described in Section 4.2. To excite the VPP modes, the experiment was set up so that the electric field of TM polarized light is perpendicular to the gratings (see Figure 4.9 (a)).

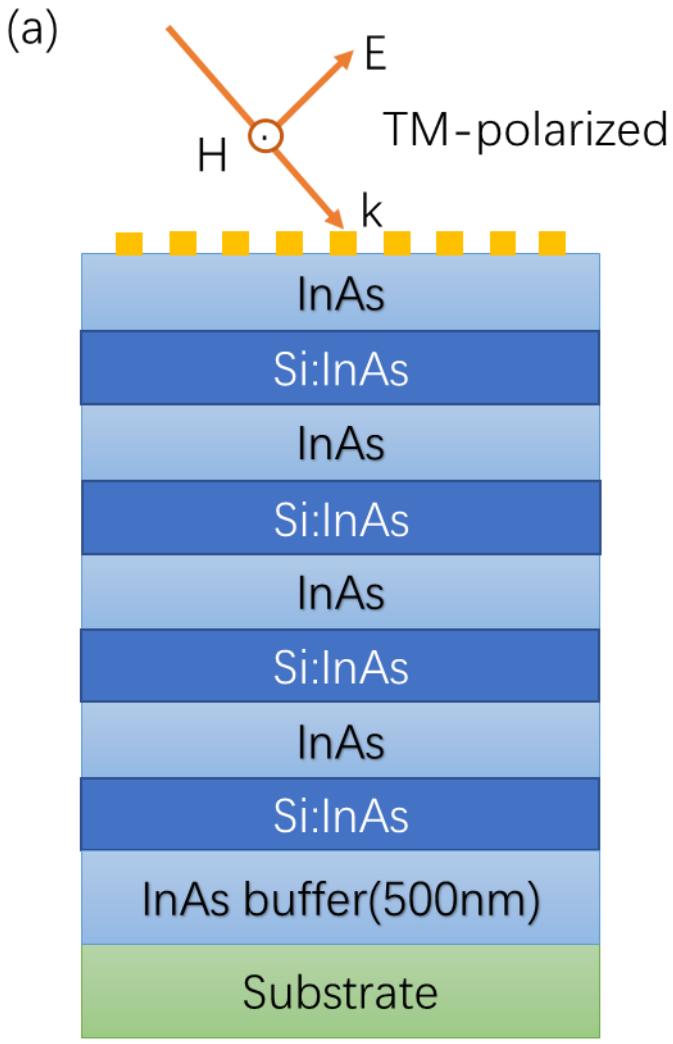
(a)
E
TM-polarized
H
k
InAs
Si:InAs
InAs
Si:InAs
InAs
Si:InAs
InAs
Si:InAs
InAs buffer(500nm)
Substrate

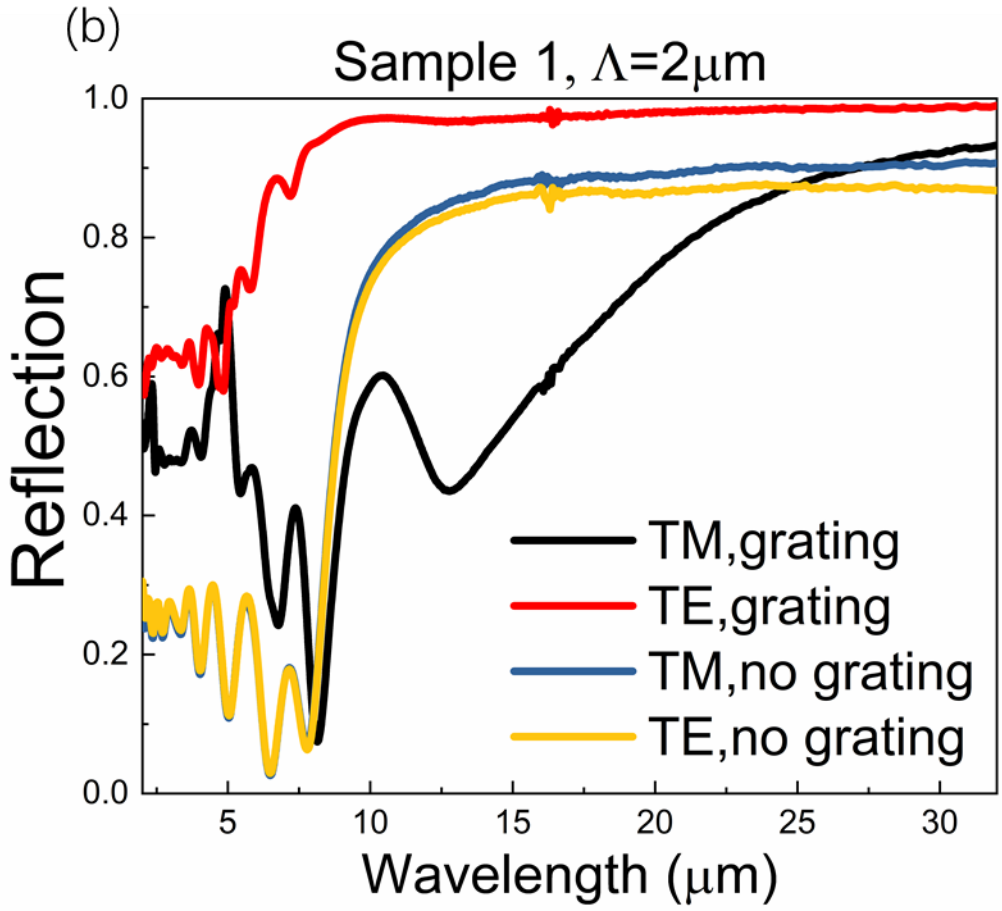

Figure 4.9: (a) Schematic of sample structure, grating coupler, and incident light. TM polarized light is perpendicular to the gratings. (b) TM and TE reflection of sample 1 with and without grating. The period of the grating is 2μm [110]. Reprint permission obtained from The Optical Society.

Figure 4.9 (b) plots the reflection data of Sample 1 with and without a 2μm grating coupler for different polarizations. The grating period is designed to excite the VPP modes in type II HMM region ($\varepsilon_{\parallel} < 0, \varepsilon_{\perp} > 0$), which is free from the disruption of Fabry-Perot oscillations and much broader than the type I region. In addition, our setup won't be able to observe the VPP modes in type I region. For the TM and TE reflection without a grating (yellow and blue curve), the reflection is near 0.9 after

10μm due to the negative $\varepsilon_{\|}$. For the TM reflection (black curve) with a grating, there is a VPP absorption around 12.5μm while this is not seen for TE polarized light (red curve). TE reflection with gold grating exhibits a higher reflection near unity after 8μm compared to those without a grating. This results from the large negative permittivity of the gold at long wavelengths.

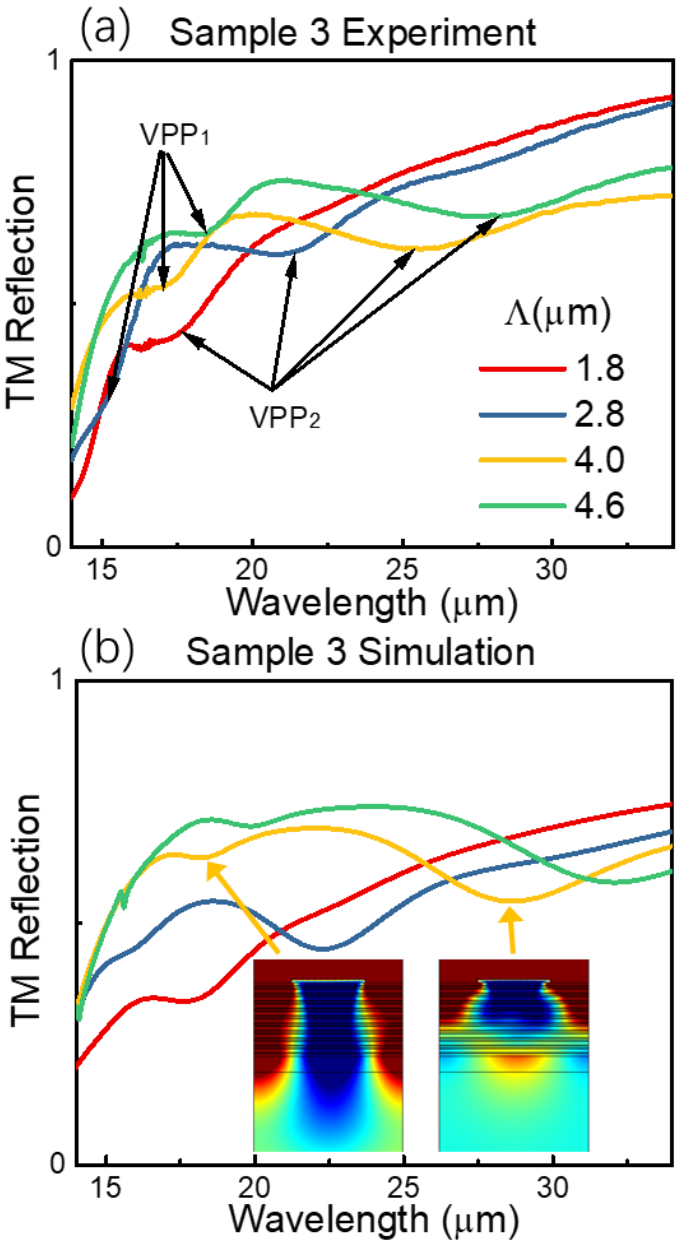

Figure 4.10: (a) Experimental and (b) simulated TM-polarized reflection from Sample 3 for four different period gratings, as indicated in the legend. VPP modes are clearly visible and marked with arrows in (a). In (b), the out-of-plane magnetic field profile is shown for two VPP modes. The shorter wavelength resonance has no nodes, while the longer wavelength resonance has one node, as expected for VPPs [110]. Reprint with permission from The Optical Society.

Figure 4.10 shows the experimental and simulated TM reflection of Sample 3 with varying grating periods ranging from 1.8 to 4.6μm. We cut the sample into a few pieces so we can fabricate gratings with different periods to map out VPP modes at different wavevectors. There are two clear VPP modes indicated by the arrows. The mode moves to a longer wavelength when we increased the grating period. This is consistent with the dispersion characteristics of VPP modes. The simulation is done by COMSOL, taking the distribution of the electron and relationship between plasma wavelength and doping density into account as described in Section 4.3. In the model, we assume a constant scattering rate across the wavelength. Maximum doping density is estimated using the plasma wavelength we derived in Chapter 3. The model reproduces the major features of the experiment data, demonstrating our assumptions of the graded interface in Section 4.3. However, the features exhibit a redshift compared to the experimental data. We attribute this to the difference between the modeled electron distribution and the real electron distribution in the sample.

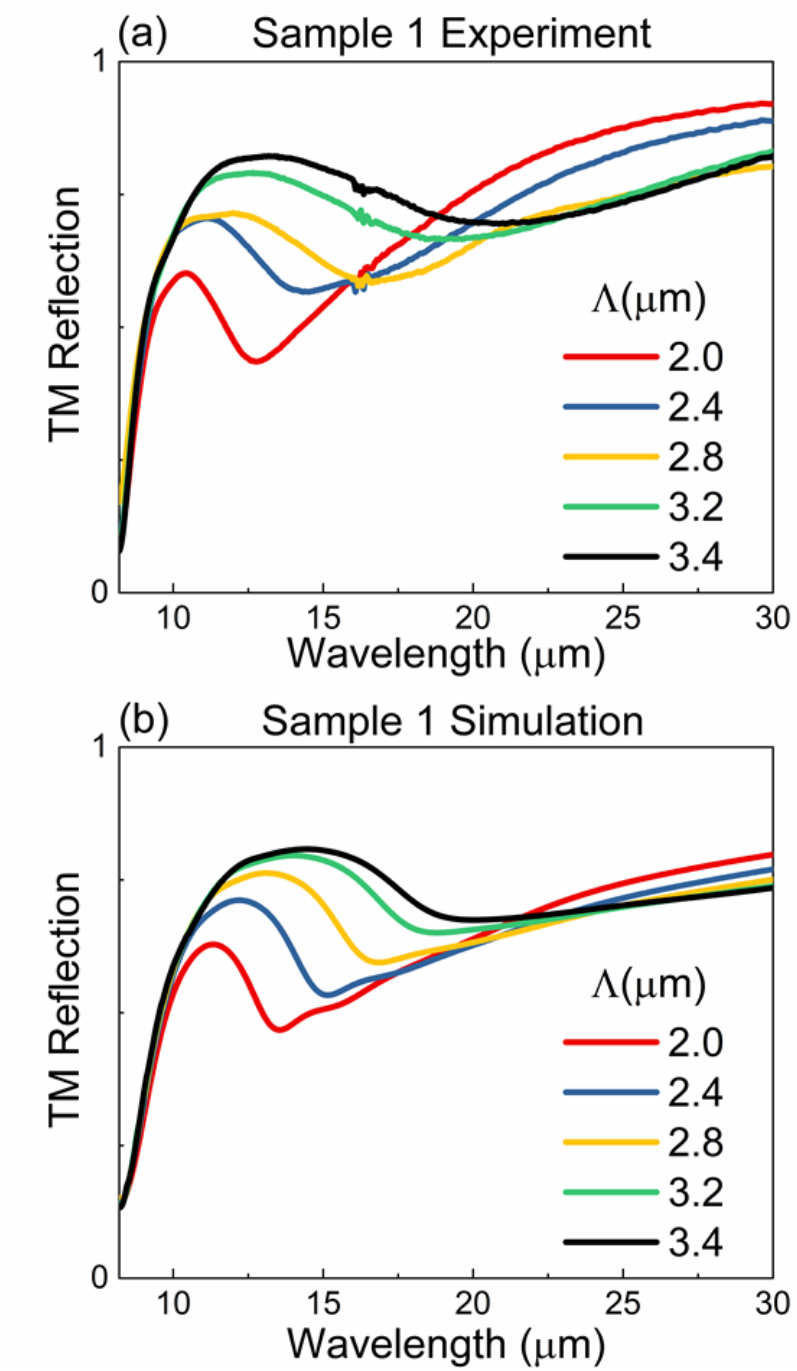

Figure 4.11: (a) Experimental and (b) simulated TM-polarized reflection from Sample 1 for five different period gratings, as indicated in the legend. Two VPP modes are visible, though they are not well-separated [110]. Reprint permission obtained from The Optical Society.

Now we turn to Sample 1 which has a plasma wavelength around 5.8μm (Figure 4.11). In the experimental data (Figure 4.11 (a)), We only observed one broad VPP absorption at shorter wavelength compared to Sample 3 ($\lambda_p = 9.5\mu m$), which has two separated VPP modes. The absorption moves to a longer wavelength with an increasing grating period. The simulation by COMSOL exhibits similar behavior, as shown in Figure 4.11 (b).

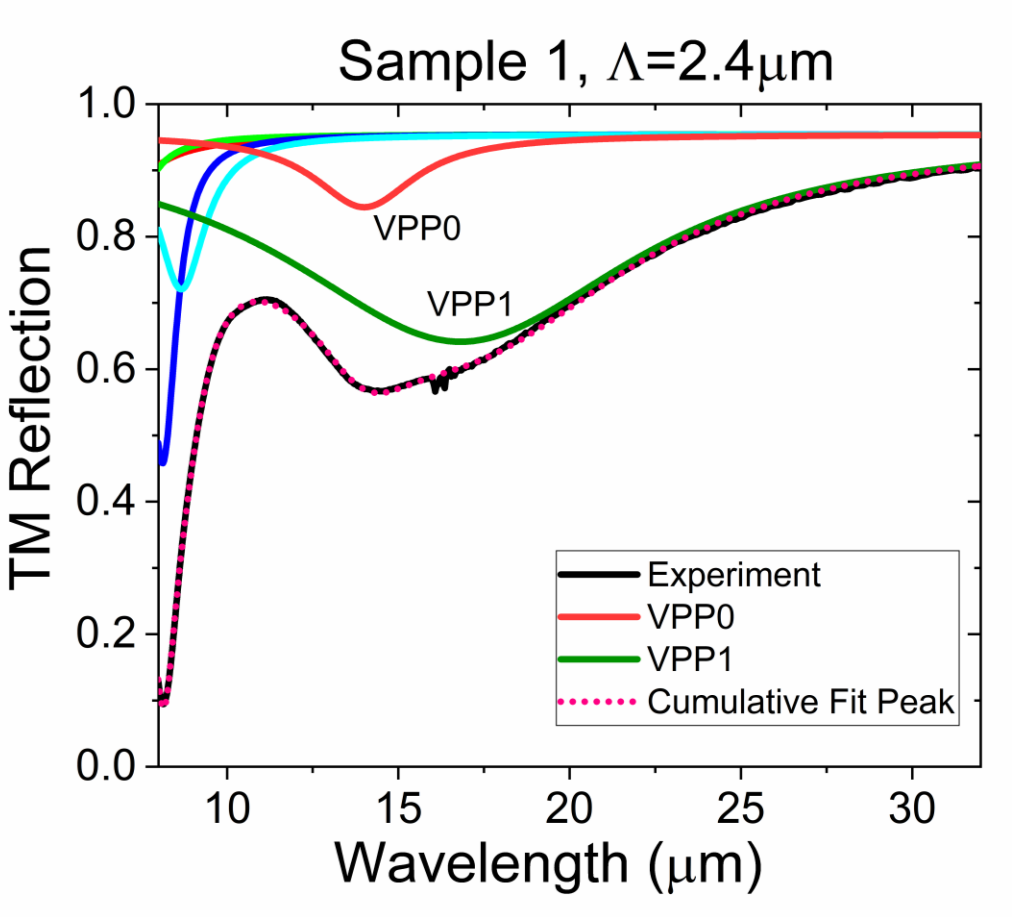

Figure 4.12: Lorentz fitting of the TM reflection of Sample 1 with a 2.4μm grating period.

In Figure 4.12, TM reflection of Sample 1 is decomposed using the Lorentz fitting, a built-in function in Origin. As shown in Figure 4.12, two VPP modes contribute to the absorption dip at 13μm. Though there could be other VPP modes at long wavelength (Figure 4.13 red line), we found that the contribution from those VPP modes is negligible and we arrived at a good fitting even we only use two peaks. The strength of the long-wavelength modes is weaker than the ones at shorter wavelength due to the large negative $\varepsilon_{\parallel}$ of HMM at long wavelength. In addition, the high scattering rate as well as poor electron confinement weaken their strength. As a result, they have a negligible effect on the VPP absorption dip.

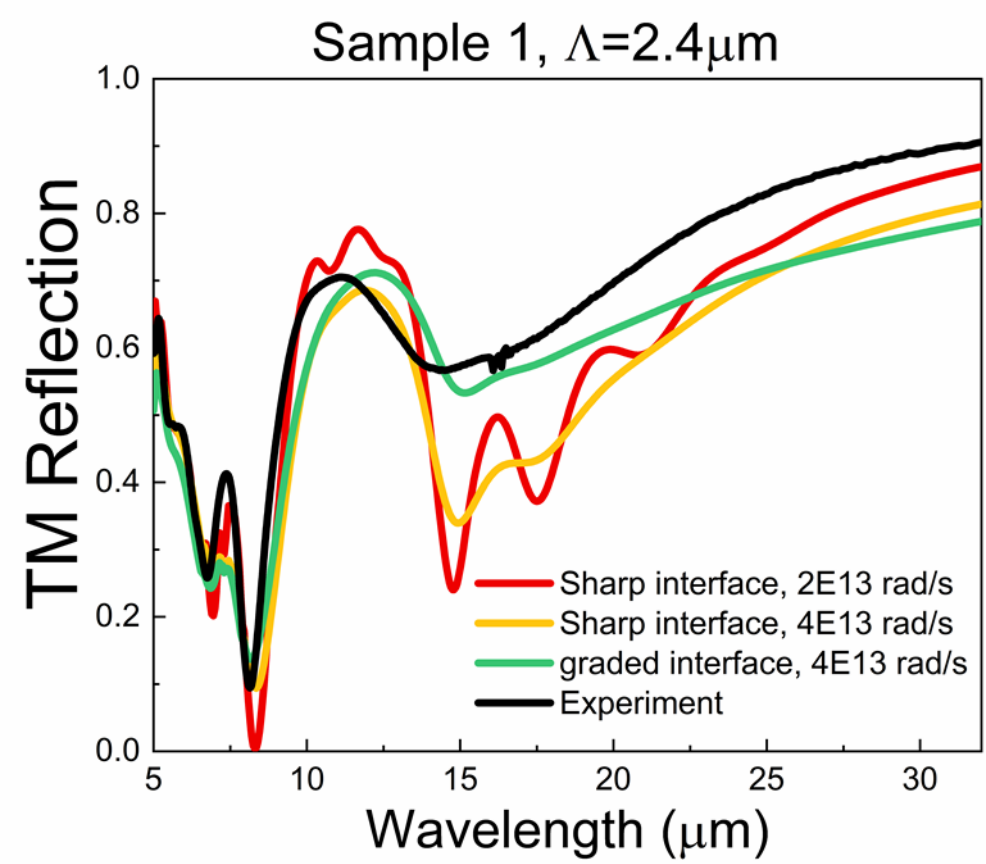

Figure 4.13: Comparison of models for TM-polarized reflection for Sample 1 with a 2.4μm period grating. Experimental data is shown in black, modeled reflection assuming a sharp interface with low scattering ($\Gamma=2\times10^{13}$ rad/s) is shown in red, a sharp interface with high scattering ($\Gamma=4\times10^{13}$ rad/s) is shown in yellow, and the graded interface is shown in green.

To analyze the behavior of the VPP modes, we simulated the reflection of the Si:InAs with different scattering rates and interface types (sharp and graded) in Figure 4.13. Other parameters are the same as Sample 1. When we have square wave distribution and small scattering rate (red line), there are up to four visible VPP modes. The high scattering rate brings down the reflectivity as well as weakens the strength of the VPP modes (yellow line). The graded interface further broadens and

weakens the VPP modes (green line), resulting in a big broad absorption. Due to the large scattering rate as well as the graded electron distribution, the VPP modes are weakened and tend to merge with each other. Since the VPP modes are simultaneously affected by the scattering rate and electron confinement, it is difficult to quantize the effect of the two parameters. However, there is a difference between the two effects. The scattering rate weakens not only the VPP modes but also other features across the whole spectrum, including Fabry-Perot oscillations. It is impossible to simulate the experimental data well for Si:InAs HMM with gratings if we only fit the scattering rate. We then turned to the electron confinement to explain the behavior of VPP modes, and we found that electron confinement only affects the strength of VPP modes. Though we incorporate these two factors into our model, there are still some discrepancies between the simulation and experiment. Therefore, other factors, such as wavelength-dependent scattering rate or imperfect gold grating profile, might need to be taken into account to simulate the VPP modes accurately. The discovery of the effect of electron confinement also provides us with an idea to improve the VPP quality: use other material classes with better electron confinement, such as Si:InGaAs/InAlAs and Si:InAs/AlSb (Section 4.5).

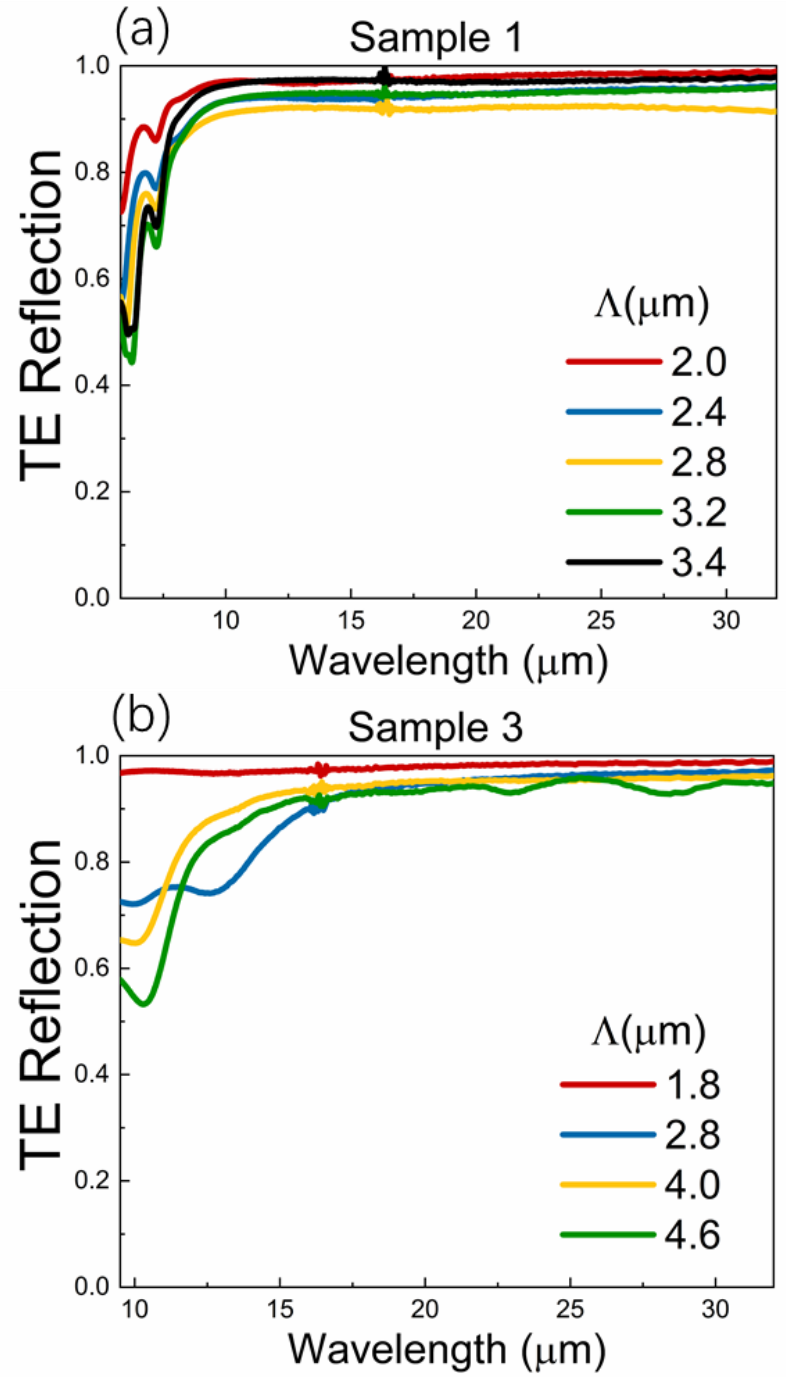

Figure 4.14: TE reflection of (a) sample 1 and (b) sample 3 with varying grating periods.

For comparison, I plotted the TE reflection of Sample 1 and Sample 3 with varying grating periods (Figure 4.14). VPP modes do not exist for TE polarized light because the electric field is parallel to the layers and the gratings. The value of TE reflection is near unity at long wavelengths for all samples. This is expected due to the negative value of $\varepsilon_{\parallel}$ and the large negative value of gold permittivity.

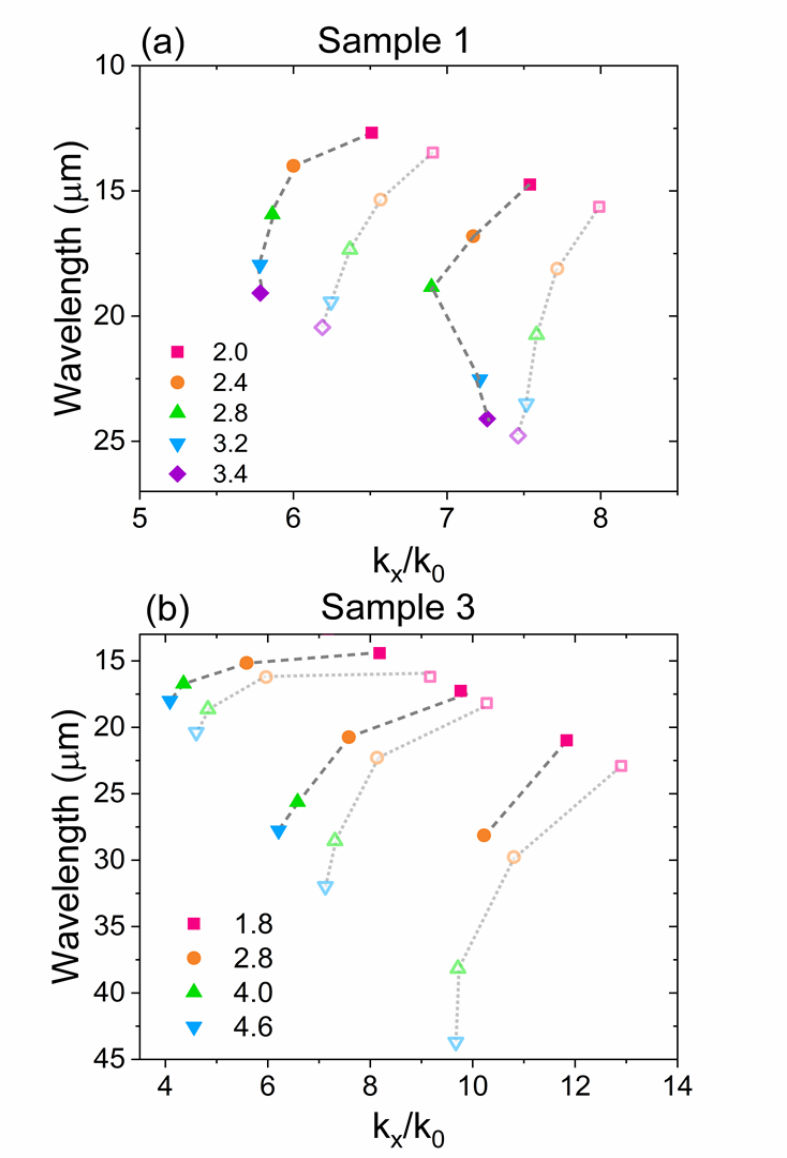

Figure 4.15: Dispersion relations for VPP modes for experimental (filled symbols) and simulated (open symbols) data for Sample 1 (a) and Sample 3 (b). Lines are a guide to the eye. Reprint with permission from [110], The Optical Society.

To study the dispersion of VPP modes, we extracted the positions of the modes and calculated the mode index using the following equation:

$$\frac{k_x}{k_0} = sin\theta + \frac{\lambda}{\Lambda} \qquad \text{Equation (4.5)}$$

Where k_x is wavevector in the HMM along the x direction, k_0 is the wavevector in the air, θ is the incident angle (10°), λ is the wavelength, Λ is the grating period. The positions of the peaks (λ) were extracted from Lorentz fitting (Figure 4.12). Then the mode index $\frac{k_x}{k_0}$ can be calculated from the above equation. The dispersion relations for Sample 1 and Sample 3 are shown in Figure 4.15. For a single mode, the mode index increases while wavelength decreases. The data points from simulation exhibit a redshift in the wavelength compared to the experimental data. We attributed it to the difficulty of knowing the exact electron distribution in the sample. The extracted dispersion curves exhibit the expected dependence of VPP modes. For Sample 3, we were able to excite VPP modes with mode index around 12 which is much larger than the wavevector of light in free space. This is also comparable to other HMM systems.

In summary, VPP modes were successfully excited in two Si:InAs/InAs HMMs with different plasma wavelength by gold grating couplers. VPP modes move to longer wavelengths with an increasing period, which can be explained by the characteristic dispersion relation. I discuss the factors that affect the VPP strength and found that the electron distribution near the interface plays an important role. The extracted dispersion relationship of VPP from reflection data is consistent with the theoretical calculation. The mode index is as high as 12, indicating strong confinement of the optical field. The next section will discuss VPP modes in different material classes that exhibit better electron confinement.

4.5 Properties of VPP Modes in Different Material Systems

Section 4.4 discussed the experimental data and simulation results of VPP modes in Si:InAs/InAs HMM. Though the VPP modes were successfully excited in

Si:InAs/InAs HMM, the modes are weak and broad. This makes Si:InAs/InAs HMM not ideal for many HMM-based applications that require strong VPP strength. As discussed in Section 4.4, the weak electron confinement contributes to this problem. In this section, VPP modes in other material classes will be investigated, including Si:InGaAs/InAlAs HMMs and Si:InAs/AlSb HMMs. These material combinations have bigger conduction band offsets than Si:InAs/InAs HMMs, indicating stronger electron confinement. The results in this section were done in collaboration with Patrick Sohr from the University of Delaware.

For Si:InAs/InAs HMM, the conduction band offset only depends on the dopant density difference, resulting in small band offset and weak confinement for electrons. Si:InGaAs/InAlAs HMM (0.52 eV) and Si:InAs/AlSb HMM (1.32 eV) both have a larger conduction band offset than Si:InAs/InAs HMM, leading to stronger confinement for electrons in the metal layer.

The growth of Si:InGaAs/InAlAs HMM and Si:InAs/AlSb HMM were described in Section 4.2. The plasma wavelength is 8.4μm for Si:InGaAs/InAlAs HMM and 8.6μm for Si:InAs/AlSb (Table 4.1). We fabricated gold grating couplers with different periods on these two samples and took polarized reflections by FTIR.

Figure 4.16 compares the experimental TM reflection and the electron distribution of three samples starting from the topological transition point where the HMM behavior changes from type I to type II. For Si:InAs/InAs, the electrons are not well confined in the doped layer. There are two separate VPP modes, which are weak and broad, as discussed in Section 4.4. Si:InGaAs/InAlAs HMM has much better confinement for electrons, leading to a stronger and narrower VPP absorption. There are three visible modes, more than the Si:InAs/InAs HMM. The Si:InAs/AlSb HMM

has an ideal square wave distribution with well-separated VPP mode absorptions. The absorption is stronger and sharper than the Si:InAs/InAs HMMs and Si:InGaAs/InAlAs HMM. The number of visible modes is five, more than the Si:InAs/InAs and Si:InGaAs/InAlAs HMMs. The reflection data reveals that Si:InAs/AlSb HMM exhibits the best VPP modes among all the samples.

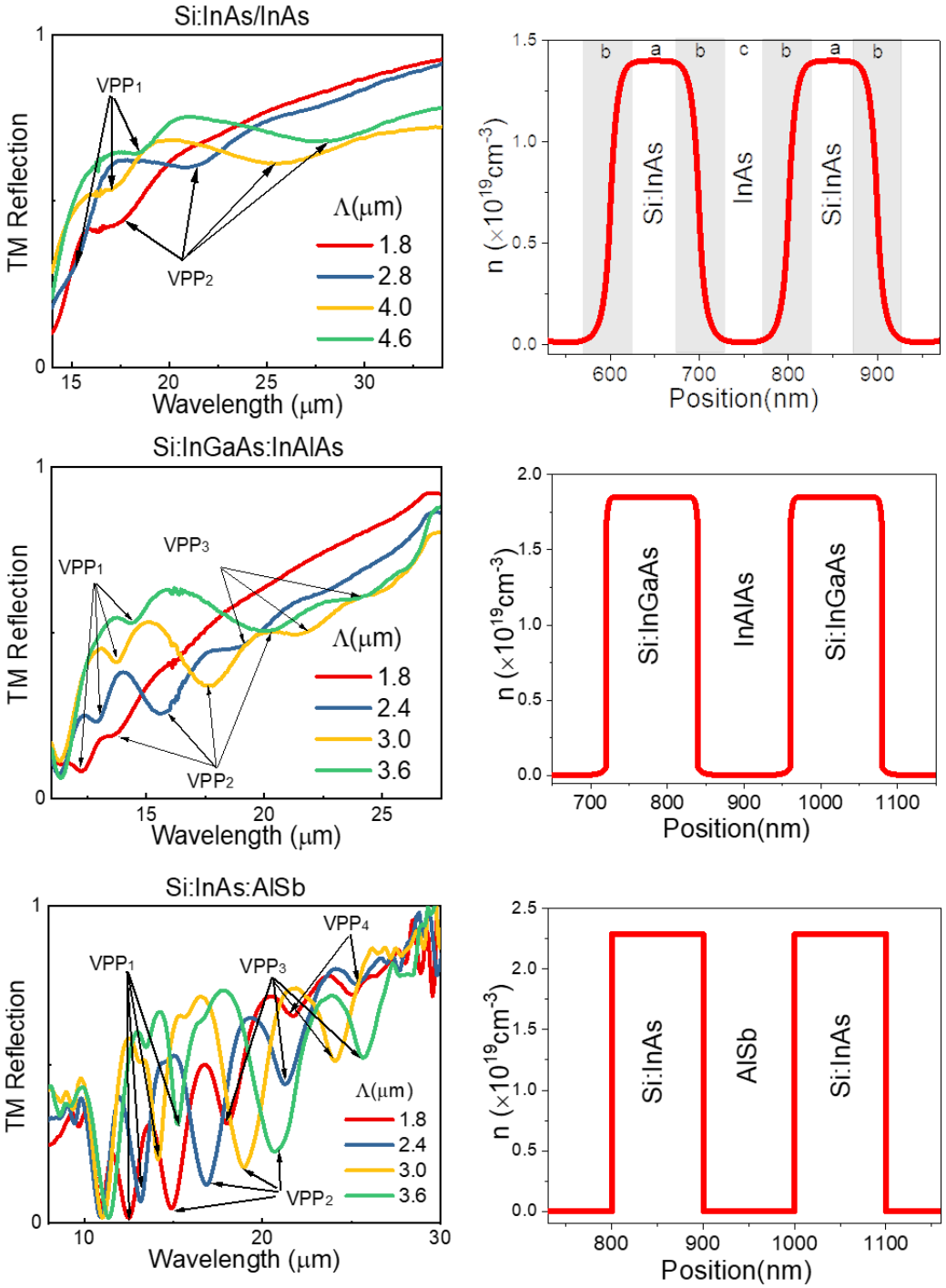
Si:InAs/InAs
TM Reflection
Wavelength (μm)
VPP1
VPP2
Λ(μm)
1.8
2.8
4.0
4.6
n (×10^19cm^-3)
Position(nm)
b
a
b
c
b
a
b
Si:InAs
InAs
Si:InAs
Si:InGaAs:InAlAs
VPP3
2.4
3.0
3.6
Si:InGaAs
InAlAs
Si:InGaAs
Si:InAs:AlSb
VPP4
Si:InAs
AlSb
Si:InAs

Figure 4.16: The experimental TM reflection and simulated electron distribution of Si:InAs/InAs HMM, SI:InGaAs/InAlAs HMM and Si:InAs/AlSb HMM. The simulation of electron distribution was done by Nextnano. Si:InGaAs/InAlAs and Si:InAs/AlSb data were reprinted from [114] with permission obtained from ACS publication.

We studied the magnetic field profile of the Si:InAs/AlSb HMM (Figure 4.17). We indexed the VPP modes after the number of nodes of the magnetic field in the direction out of the plane. This indexing scheme was proposed by Avrutsky *et al* [19]. For VPP0, there are no nodes. For VPP1, there is one node, and so on (Figure 4.17 (b)). This is consistent with the theoretical study done by other people [19]. In Figure 4.17 (a), we used COMSOL to map out the magnetic profile in the direction out of the plane. The number of nodes increases with increasing mode order. This is clearer in Figure 4.17 (b) where we plot the magnetic field strength along a vertical line across the center of the sample. It is also noticeable in Figure 4.17 (a) that the strength of the magnetic field decreases with increasing mode indices (the color become shallower). This is consistent with the TM reflection data as shown in Figure 4.16, where the VPP mode absorption become weaker and broader for higher order modes. For higher order modes, the field confinement is stronger than the lower order modes, leading to a greater scattering loss. The magnetic field profile is not symmetric which differs from the Figure 4.6 (b). The asymmetric magnetic field profile is caused by the different effective refractive index on the two sides of the samples. On one side of the HMM, there are thick buffer layers following by a thick GaAs layer. On top of the sample, there are gold gratings and air. Since the refractive index of gold grating is significantly different from buffer layers and GaAs, the magnetic field profile displays vertical asymmetry.

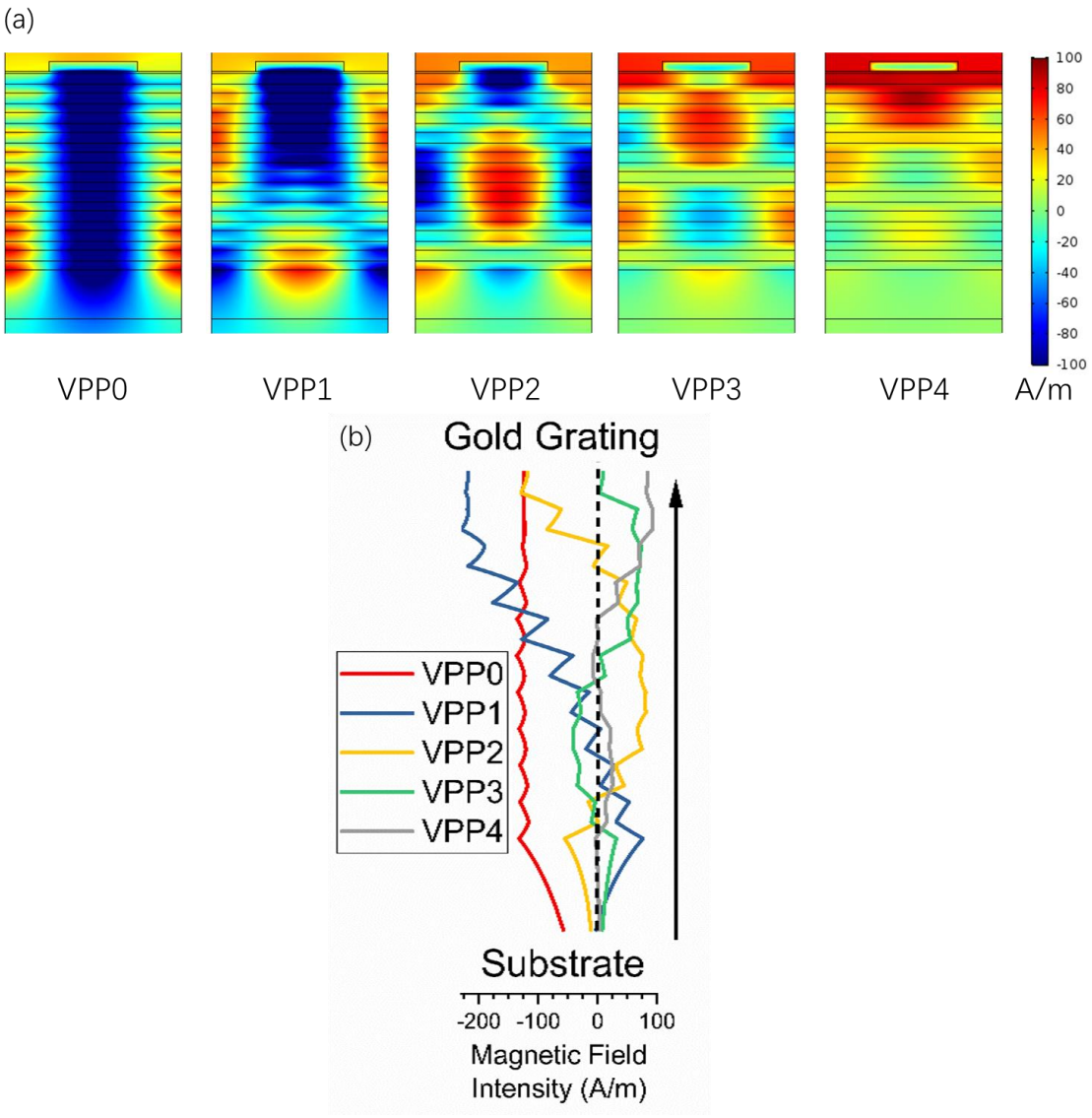

Figure 4.17: (a) Magnetic field profiles for the five VPP modes for the Si:InAs/AlSb HMM with a 1.8 μm grating. (b) Magnetic field intensity as a function of vertical position through the sample. The black dashed line indicates the zero point and the sawtooth nature of the lines are the result of the alternating metal and dielectric layers [114]. Reprint permission obtained from ACS publication.

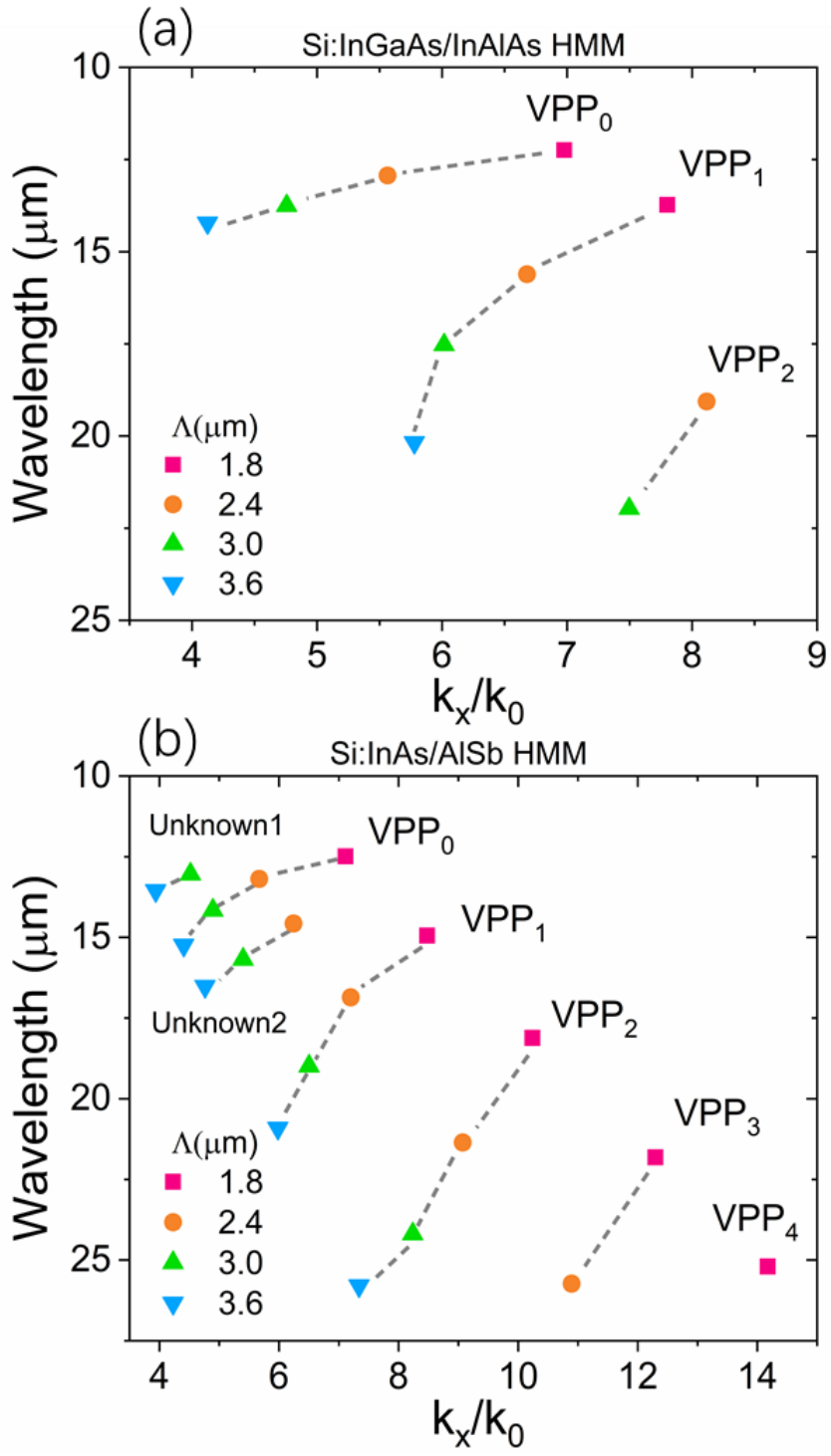

Figure 4.18: Dispersion relation extracted from experimental data. (a) Si:InGaAs/InAlAs HMM (b)Si:InAs/AlSb HMM.

We extracted the dispersion relation of VPP modes for Si:InGaAs/InAlAs HMM and Si:InAs/AlSb HMM from experimental data, as shown in Figure 4.18. The dispersion relation is similar to that of Si:InAs/InAs HMM (Figure 4.15) but with more modes. For a single mode, the mode index increases with decreasing wavelength. Higher order modes have larger mode indices than lower order modes at the same wavelength. The largest mode index is around 14 for Si:InAs/AlSb HMM. This is comparable to other HMMs created from different material classes. There are two unknown modes that exist in Si:InAs/AlSb HMM, as indicated in Figure 4.18 (b). We suspect they are surface modes supported by the multilayer structure.

Among all the material classes we studied, Si:InAs/AlSb HMM exhibits the best VPP modes while Si:InAs/InAs HMMs exhibit the weakest VPP modes. Si:InGaAs/InAlAs has a smaller conduction band offset than Si:InAs/AlSb and it could suffer from the alloy scattering. Thus it exhibits moderate VPP modes. The comparison of VPP modes between different material classes could help people choose the best material combination for the practical applications of HMMs such as subwavelength imaging, focusing, and enhanced detectors.

4.6 Conclusion

In this chapter, high-quality VPP modes of semiconductor HMMs in infrared were demonstrated. We successfully excited the VPP modes in HMMs by gold grating couplers in different material systems, including Si:InAs/InAs, Si:InGaAs/InAlAs and Si:InAs/AlSb HMMs. Through the study of Si:InAs HMM, we found that the electron distribution profile near the dielectric/ metal interface significantly affects the strength of VPP modes. Then we turned to Si:InGaAs/InAlAs and Si:InAs/AlSb material systems, which have better electron confinement. Among the material systems we

studied, Si:InAs/AlSb HMM, which has the largest conduction band offset, exhibits the best VPP modes. We extracted the dispersion relation of these HMMs from the reflection spectrum. The mode index of Si:InAs/AlSb is as high as 14, which is comparable to visible and near-infrared HMMs made from other material classes [19,75,103,104,109].

The systematic study of VPP modes in semiconductor HMMs improves our understanding of how light interacts with multilayer HMM. We also explored the factors that affect the VPP modes. This could be useful when we design HMM-based devices. Though our study focuses on infrared, the conclusion could be applied to other HMM for different wavelengths. The study paves the way for HMM in practical applications such as imaging well below the diffraction limit and detector with better sensitivity.

Chapter 5

THE GROWTH OF HIGHLY SILICON DOPED INDIUM ASENIDE USING BISMUTH SURFACTANT

5.1 Background of the Growth of Si:InAs

Highly Si-doped InAs is one of the major metal components of semiconductor HMM due to its high maximum doping level and small electron effective mass. However, Si atoms tend to segregate at the surface at high doping concentration, which significantly affects the optical properties, electrical properties, and surface quality of the Si:InAs.

To date, the mechanism behind the surface roughening of highly-doped InAs has not been fully investigated. The repulsive Coulomb interaction between the ionized Si atoms could be an important reason. In ref [115], the authors demonstrated that the repulsive Coulomb interaction between Be dopants limits the doping density in the GaAs and leads to the segregation of dopants at extremely high doping concentrations. Also, Si atoms are impurities in the InAs lattice and do not have to be ionized when they stay at the surface. Thus Si atoms could be at a lower energy state if they stay at the surface compared to being ionized in the bulk.

A fast growth rate (over 1.5μm/h) and a low growth temperature (< 450℃) are two common strategies to achieve good Si:InAs quality. When the growth rate is faster than the diffusion rate of Si atoms, Si atoms will not be able to reach the surface. Instead, they are “buried” in the InAs lattice. A lower growth temperature can

decrease the diffusion rate of Si atoms, thus slowing them down from moving to the surface. However, a fast growth rate indicates a higher cell temperature, which is not favored by an MBE system since it increases the chamber pressure and could cause potential problems to the effusion cell. Also, a fast growth rate is not favored when we grow some fine structures such as quantum wells. A lower growth temperature makes the integration of Si:InAs with other material difficult. For example, GaAs, GaSb, and AlSb all favor a higher growth temperature. Changing the growth temperature interchangeably during the growth is not feasible. Therefore we need to investigate other ways to grow Si:InAs with high quality.

Applying surfactants is a common strategy to improve material qualities during the growth of semiconductors by suppressing the diffusion of group III atoms, preventing 3D growth mode. Bismuth has been widely used as a surfactant for the growth of germanium [116], InAs quantum dots [117] [118], GaAs-InGaAs heterostructures [119], InAsSb [120], and many more systems [121–126]. It usually does not incorporate into the lattice unless the substrate temperature is below 350℃ [127–130]. There are other surfactants for the growth of III-V semiconductors, such as tellurium and antimony. However, these surfactants will either introduce significant defect levels or incorporate into the lattice.

In this project, the growth of highly Si-doped InAs using bismuth as a surfactant was investigated. In Section 5.2, I will discuss the growth and characterization details of highly Si-doped InAs. Section 5.3 and Section 5.4 will focus on the optical properties, electrical properties, and surface morphology of Si:InAs grown at different conditions. We will see how Bi surfactant improves the

quality of highly-doped Si:InAs and broadens the growth window of Si:InAs. Section 5.5 is the conclusion of the project.

5.2 The Growth and Characterization of Highly-Doped InAs using Bismuth Surfactant

The chapter will discuss ten Si:InAs samples with varying growth temperatures and Bi fluxes (see Table 5.1). The samples were grown on undoped GaAs substrates directly without buffer layers. The deoxidation process is the same as described in previous chapters (Section 3.2). The indium beam equivalent pressure was 1.56×10^{-6} Torr. The Si cell temperature was the same for all samples.

Table 5.1: Bi/In flux ratio, growth temperature, carrier density, mobility, plasma wavelength and scattering rate of Si:InAs samples.

Sample Number	Sample ID	Bi/In flux ratio(%)	Growth temperature (℃)	Carrier concentration ($\times 10^{19} cm^{-3}$)	Mobility ($cm^2V^{-1}S^{-1}$)	λ_p (μm)	Γ ($\times 10^{13} rad/s$)
1	171020A	1	450	4.655	1160	6.20	1.6
2	171020B	0	450	4.164	1038	6.32	2.5
3	171021A	2	450	4.735	1145	6.15	1.3
4	171021B	2	470	4.644	1139	6.17	0.9
5	171026A	2	490	4.708	1058	6.03	1.9
6	171026B	2	520	4.708	1150	6.05	1.6
7	171027A	2	550	4.629	1264	6.22	2.9
8	171027B	3	550	4.708	1251	6.15	2.1
9	171028A	4	550	4.629	1235	6.20	2.7
10	171028B	5	550	4.790	1246	6.20	2.4

I conducted room-temperature Hall measurements using a custom-built four-point van der Pauw setup to extract the bulk carrier density (n_{3D}) and the mobility (μ) of the samples (Section 2.3.2.1). The plasma wavelength and scattering rate were extracted from the reflection spectrum. A DTGS detector and a Pike instrument were used to set up the reflection experiment with an incident angle of 10 degrees. The spectral resolution is 4cm^{-1} and the scan velocity is 10kHz. The reflection data were normalized to the reflection from a gold mirror whose reflection is assumed to be 100% in infrared. Extracted carrier density, mobility, plasma wavelength (λ_p) and the scattering rate (Γ) were summarized in Table 5.1.

5.3 Optical and Electrical Properties of Heavily Si-doped InAs Thin Films

Hall measurement was used to extract the carrier density and mobility of the films, as shown in Figure 5.1. Solid symbols are used to represent samples with a shiny specular surface, while open symbols indicate a diffuse cloudy surface. The dotted line indicates the carrier density predicted from calibration films assuming the ionization efficiency is 100%. The sample grown at 450℃ with 0% Bi flux (red rectangular) shows a low carrier density and mobility with a cloudy surface. With 1% Bi added (orange circle), the carrier density was increased to the expected value (dashed line) with higher mobility and a specular surface. A 2% Bi (green triangular) further increases the carrier density without a significant effect on the mobility within the error bars. Holding the Bi flux at 2% and other conditions the same, several Si:InAs samples were grown with increasing growth temperatures (green triangular symbols). The surface stays specular even at 520℃. There is a small increase in the carrier density with a small decrease in mobility probably caused by the scattering from incorporated ionized impurities. When we reached 550℃, the surface became

diffuse with a decreased carrier density below the expected value. When Bi flux was increased to 3% (blue triangular), the surface returned to specular with slightly increased carrier density. However, further increasing the Bi flux to 4% leads to a diffuse surface. The three samples grown at 550℃ exhibit the highest mobility, disregarding the quality of the sample surface. We attribute this to the improved crystallinity of the InAs when grown at a higher temperature.

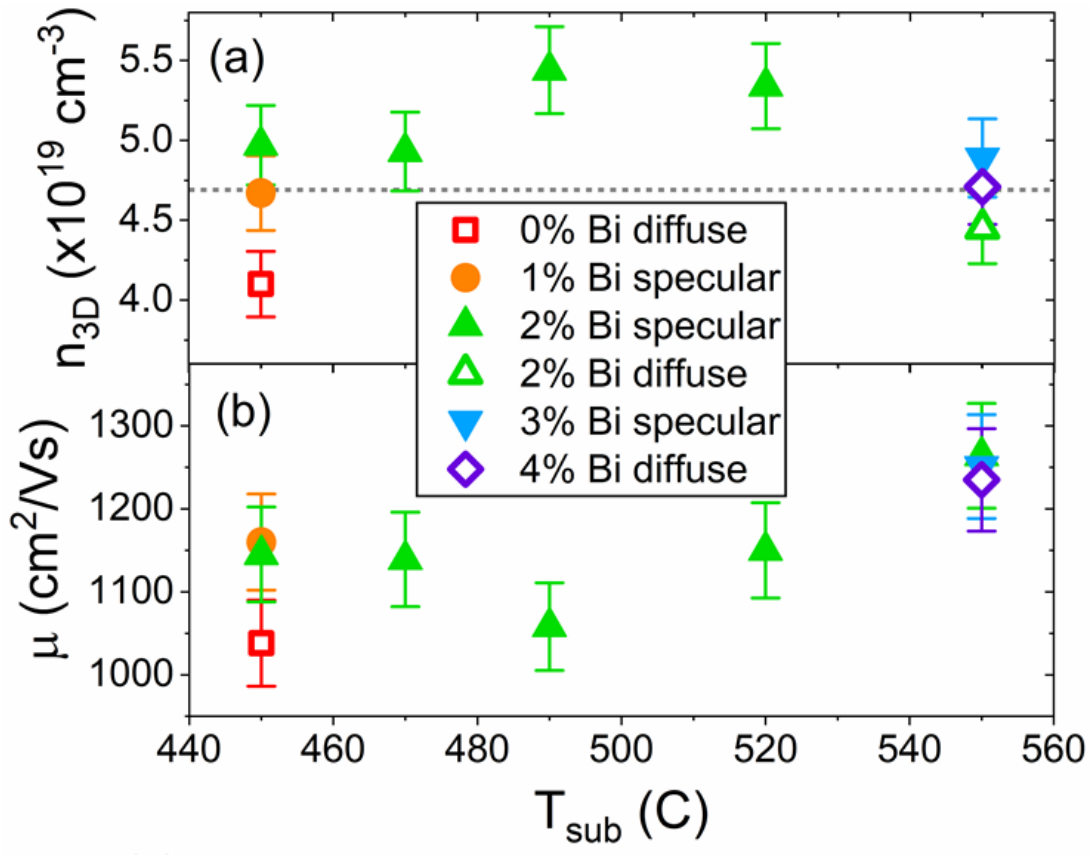

Figure 5.1: Electrical properties extracted from Hall measurements. (a) carrier density (b) mobility. Solid symbols indicate specular surface, while open symbols indicated diffuse surface. The dotted line is the carrier density predicted from calibration films.

Plasma wavelength (λ_p) and scattering rate (Γ) were extracted from the reflection spectrum using transfer matrix and Drude model:

$$\varepsilon_{Si:InAs} = \varepsilon_s \left(1 - \frac{\omega_p^2}{\omega^2 + i\omega\Gamma}\right) \qquad \text{(Equation 5.1)}$$

where ε_s is the high frequency permittivity of the undoped InAs and ω is the frequency of incident light. Figure 5.2 shows the experimental and simulated reflection of the sample grown at 450℃ with 1% Bi flux. The simulation matches the experiment very well.

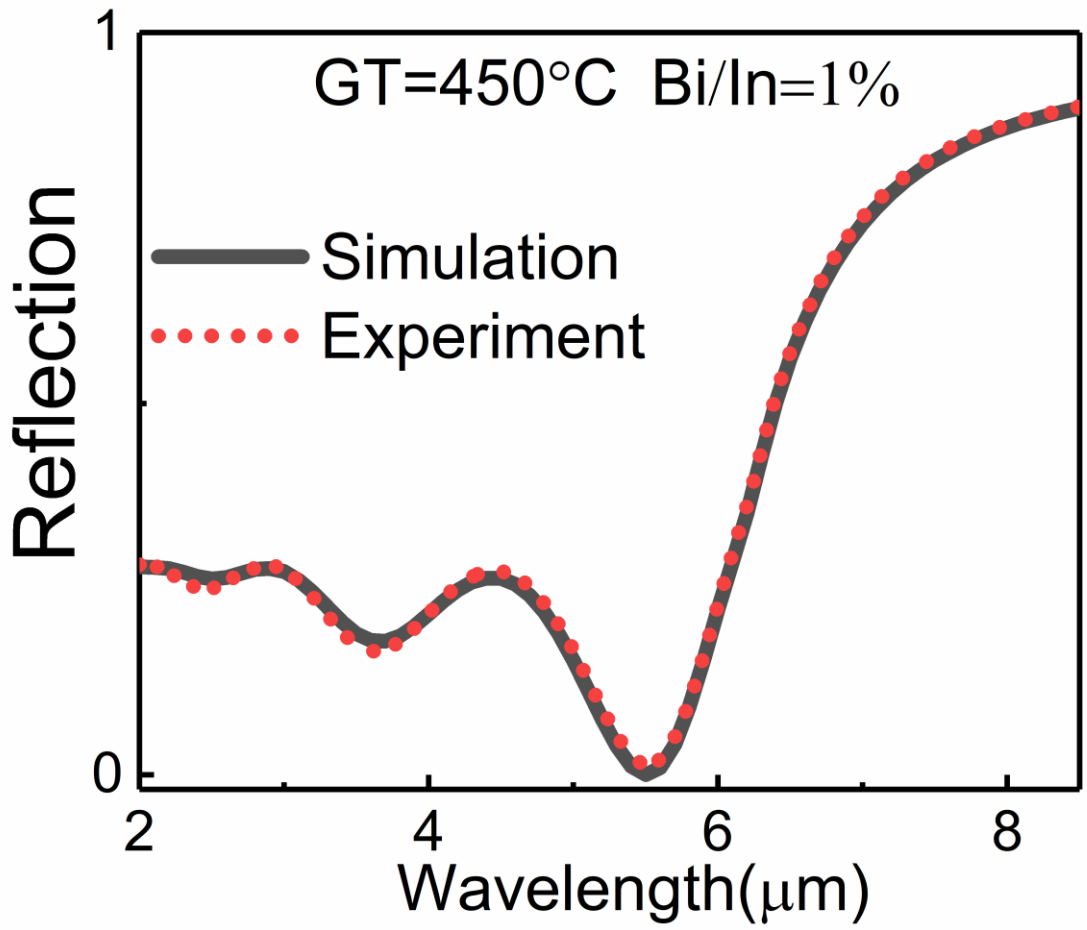

Figure 5.2: Simulated and experimental reflection of the sample grown at 450℃ with a 1% Bi/In flux ratio.

The extracted plasma wavelength and scattering rate were plotted in Figure 5.3. The plasma wavelength exhibits a similar trend to the carrier density since the plasma wavelength is proportional to the free carrier density. Shorter plasma wavelengths were obtained at higher carrier densities. However, the scattering rate doesn't follow the trend of mobility in Figure 5.1 (b). This is reasonable because mobility is a DC measurement, while the scattering rate is measured at high optical frequencies.

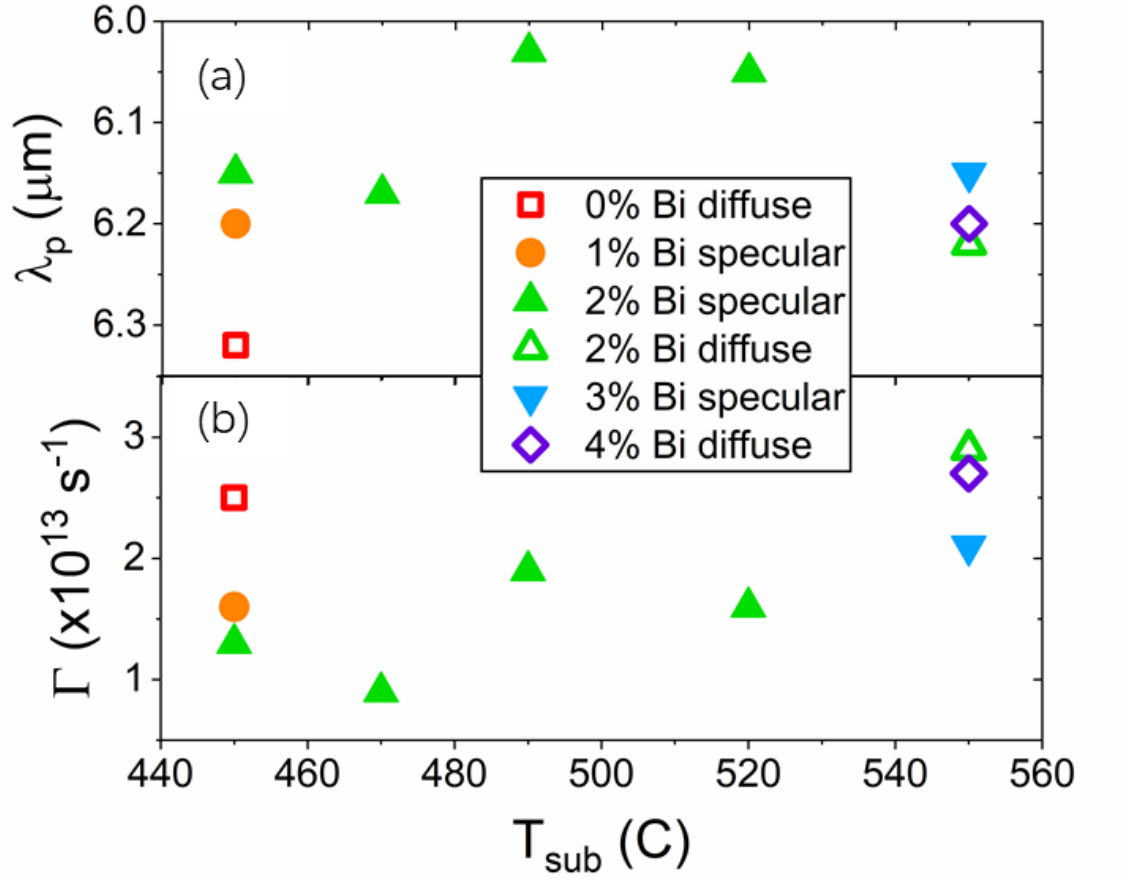

Figure 5.3: Plasma wavelength and scattering rate extracted from the reflection spectrum. Solid symbols indicate a specular surface, while open symbols indicate diffuse surfaces.

5.4 Surface Morphology of Heavily Si Doped InAs Thin Films

Optical microscope, SEM and AFM were used to study the surface morphology of Si:InAs samples. Figure 5.4 shows the pictures from the optical microscope and SEM for two samples grown at 450℃ with different Bi surfactant fluxes. For the sample grown at 450℃ without Bi flux (Figure 5.4(a)), we observed dark spots under the optical microscope. These dark spots cause the sample appearance to be cloudy to the eye. Examined under SEM, these dark spots are deep

trenches elongated along the [110] directions. We think these trenches are caused by the clustering of Si atoms [131,132]. Similar trenches were observed in heavily-doped GaAs [132,133]. For those GaAs samples, the observed trenches also evolved along [110] and it was found that a higher doping density led to more and longer trenches. InAs has similar crystal structure to GaAs and the trenches exhibit similar characteristics, so it is reasonable to hypothesize that the trenches observed in InAs are also caused by Si atoms clustering. For the sample with Bi flux (Figure 5.4 (b)), the surface is smooth without those trenches along [110] direction under optical microscope or SEM. This sample also appeared to be specular and shiny to the eye. We also collected AFM pictures, as shown in Figure 5.5. The sample grown at 450℃ without Bi exhibits deep trenches, with maximum depth around 400nm. The sample grown at 450℃ with Bi is flawless and smooth. The AFM images are consistent with the SEM and optical microscope pictures. The improvement of the surface morphology indicates that the presence of Bi help Si atoms better incorporate into the lattice rather than clustering at the surface. The data from Hall measurement and FTIR also supports this conclusion.

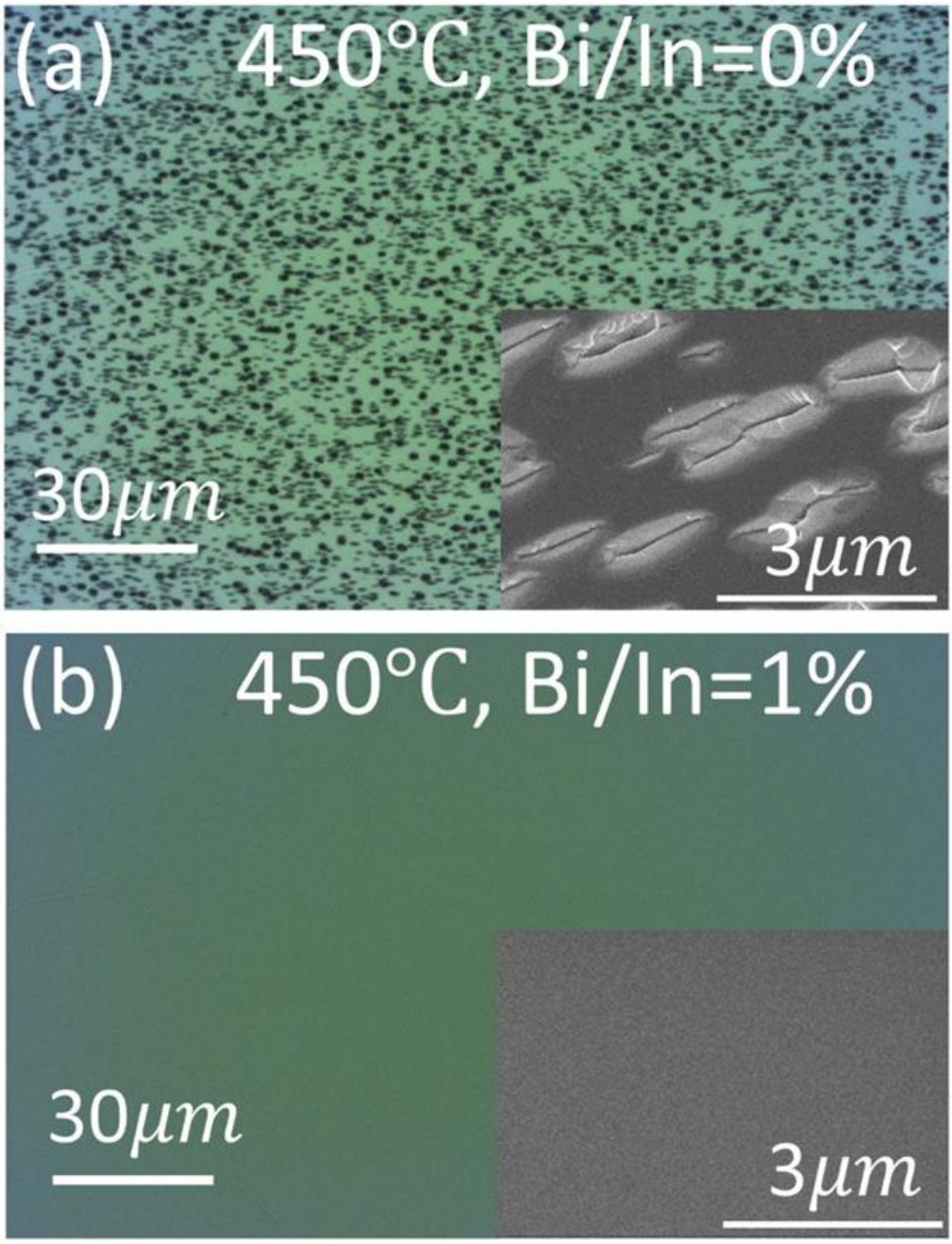

Figure 5.4: Optical microscope images for samples grown at 450℃ with bismuth fluxes of 0% (a) and 1% (b). Insets show corresponding scanning electron microscope images. Rectangular trenches are observed in (a), while (b) is featureless.

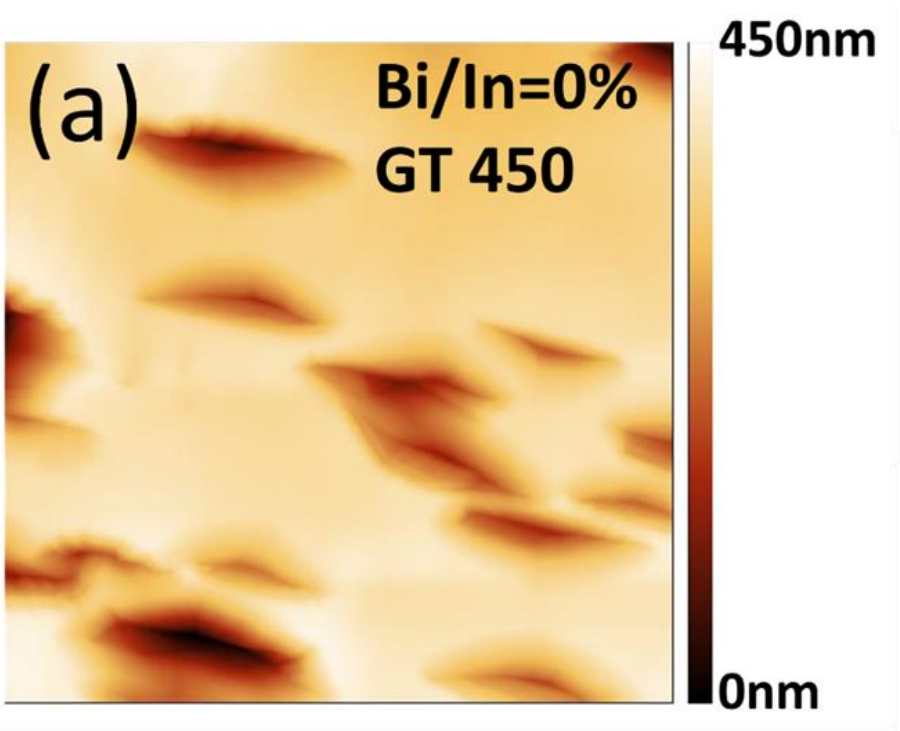
(a)
Bi/In=0%
GT 450
450nm
0nm

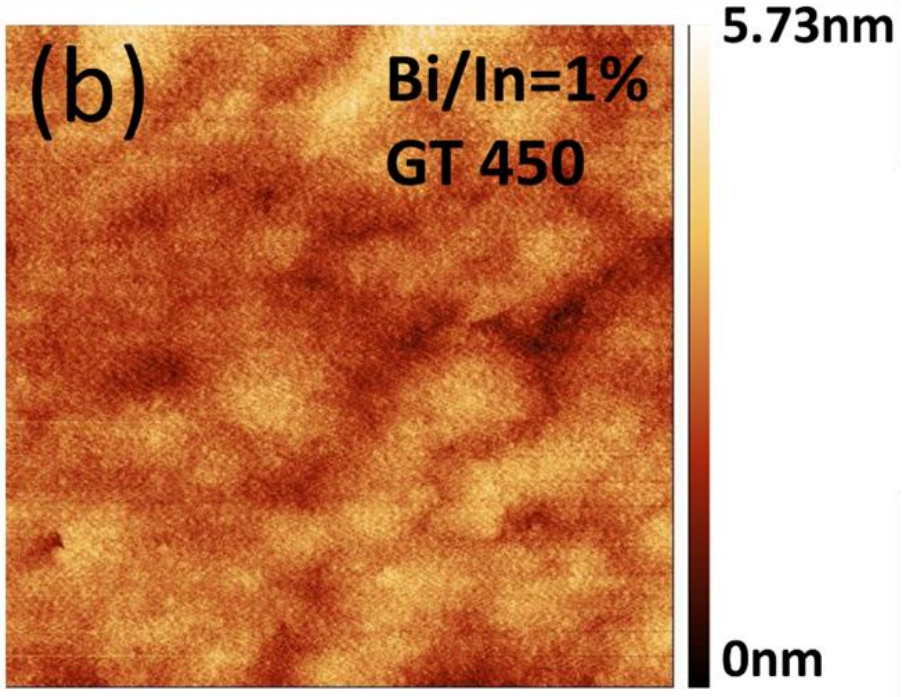
(b)
Bi/In=1%
GT 450
5.73nm
0nm

Figure 5.5: AFM figures for the sample grown at 450℃ (a) without Bi and (b) with Bi. Deep trenches are present in (a) while (b) is atomic smooth. The AFM data were taken by Patrick Sohr from the University of Delaware.

Root mean square (RMS) roughness of surface roughness is extracted from the AFM, as shown in Figure 5.6. Figure 5.6 (a) shows RMS roughness for samples grown at 450℃ and 550℃ as a function of Bi flux. The RMS roughness of samples grown at 450℃ drops from 64.4nm to 0.7nm when Bi/In ratio changes from 0% to 1%. Further increasing the Bi flux does not change the roughness significantly. This indicates that the Bi surfactant has an apparent smoothing effect for Si:InAs. For samples grown at 550℃, the sample with 3% Bi flux has the lowest RMS roughness. This is also the only shiny sample to the eye for samples grown at 550℃. In Figure 5.6 (b) plots the RMS roughness of samples grown at 2% Bi/In flux ratio but with varying temperatures from 450℃ to 550℃. The RMS roughness stays below 15nm when the substrate temperature is below or equal to 520℃, indicating a broader growth window. The RMS roughness increases significantly at a higher temperature, around 32nm at 550℃.

At low temperature and low Bi flux, the roughness of the Si:InAs results from the trenches caused by Si atom clustering. The application of Bi flux could suppress the diffusion of Si atoms, preventing the formation of the trenches. When we held the Bi flux constant and increased the growth temperature, the thermal roughness gradually dominates. Further increasing the Bi could somehow suppress the roughness, by suppressing the movement of group III atoms as well as Si atoms. However, large Bi flux could also lead to the formation of Bi-In complexes, resulting

in a rough surface. In summary, the roughness of Si:InAs is caused by multiple mechanisms, including Si atom clustering, thermal roughness, and Bi-In complex.

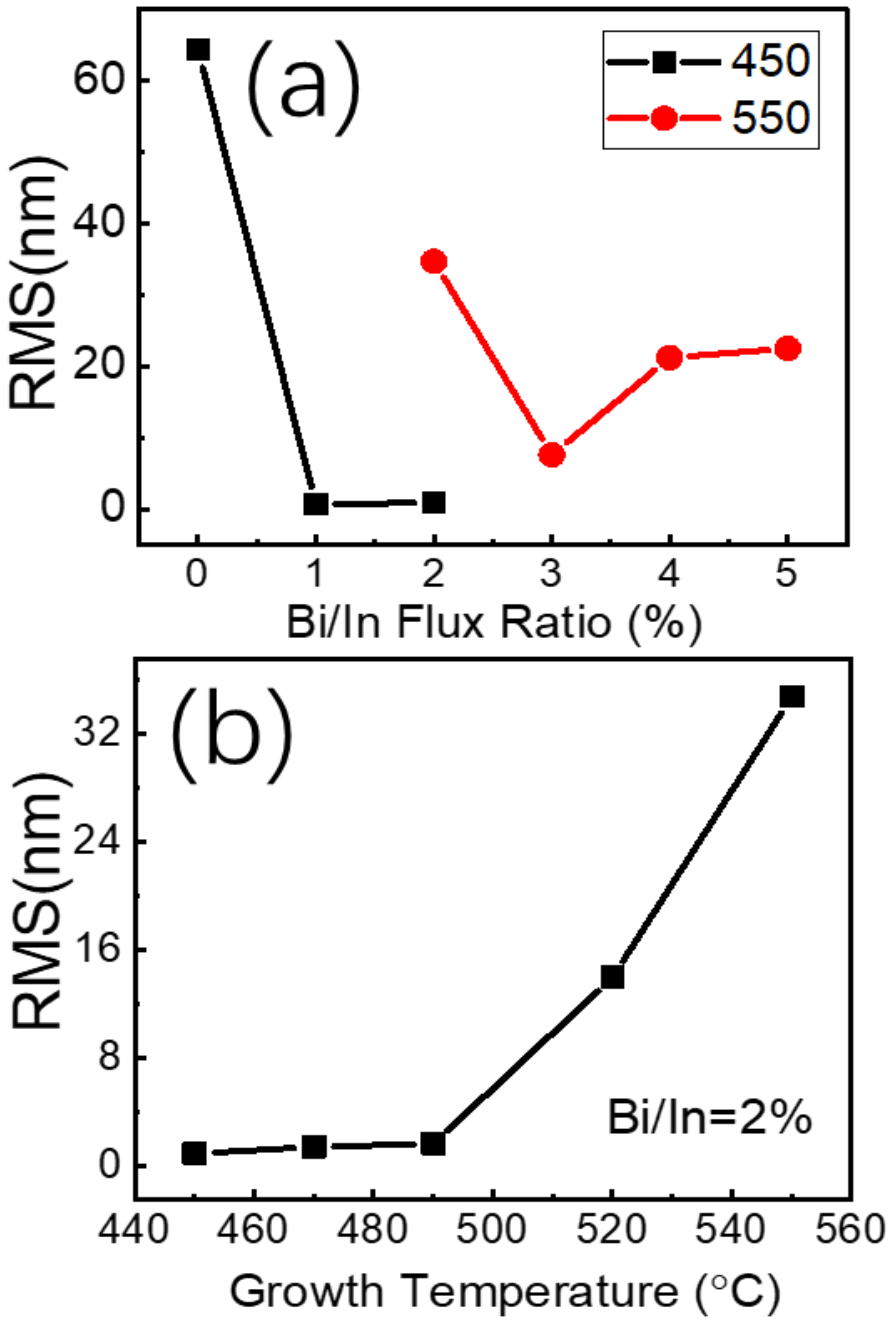

Figure 5.6: RMS roughness as a function of growth temperature for samples grown with a bismuth flux of 2%; surface roughness increases above ~500℃. (d) RMS roughness as a function of bismuth flux for samples grown at 450℃ (black squares) and 550℃ (red circles). The AFM data were taken by Patrick Sohr from the University of Delaware.

5.5 Conclusion

In this chapter, the effects of Bi surfactant on the optical properties, electrical properties and surface morphology of highly Si-doped InAs were investigated. It was demonstrated that a small amount of Bi could improve the silicon incorporation, lower the scattering rate, and lead to a smoother surface. Improved silicon incorporation and a low scattering rate are crucial for the creation of plasmonic materials. Also, a smooth surface is always required for practical device fabrication. The use of Bi surfactant also broadens the growth window of Si:InAs, allowing us to grow Si:InAs at a higher temperature. This makes the epitaxial integration of Si:InAs with other semiconductors, such as AlSb and GaSb which favor higher growth temperature (over 500℃), much easier.

Chapter 6

CONCLUSIONS AND FUTURE WORK

6.1 Summary and Impact of the Work

Previous chapters focus on the growth, characterization, and modeling of semiconductor HMMs for the infrared. In Chapter 1, the concepts of optical metamaterials and HMM were briefly reviewed. To move the study of HMM to the infrared, we chose III-V semiconductor as building blocks due to their remarkable properties including small effective masses and high mobilities.

Chapter 3 presented the designer InAs HMM for the infrared. We grew InAs HMMs with various filling ratios and doping concentrations. The reflection and transmission data shows InAs HMMs have flexible optical properties by adjusting the structure parameters. Discontinuity of Brewster angle and negative refraction, two hallmarks of HMM, were experimentally demonstrated. The shortest experimental working wavelength of InAs HMM is as short as 5.8μm. This is the first demonstration of HMM created from a single material system.

Chapter 4 investigated the VPP modes in different semiconductor HMMs. We first study the VPP modes in InAs HMMs. The experimental result and simulation show that the electron distribution near the metal/dielectric interfaces plays an important role in the quality of VPP modes. Due to weak electron confinement in the doped layer, InAs HMMs exhibit weak and broad VPP modes. Then we turned to Si:InGaAs/InAlAs HMM and Si:InAs/ AlSb HMMs, who have better electron

confinements. Up to five modes were observed in a single sample (Si:InAs/AlSb HMM). The highest mode index is around 14, which leads to strong light confinement in the bulk. We also found that InAs/AlSb HMM exhibits the best VPP modes. The study of VPP modes in different HMMs sheds light on how to select suitable materials when considering practical HMM applications. Though we only focus on infrared in the dissertation, the conclusion could also be applied to other HMMs and wavelength range.

In Chapter 5, the surfactant effect of bismuth on the growth of highly Si-doped InAs was discussed. The optical properties, electrical properties, and surface morphology were significantly improved after the application of bismuth surfactant. The growth window of highly doped InAs is also broadened by the bismuth surfactant, making it more compatible with other semiconductors who favor higher growth temperatures.

This dissertation systematically studies the semiconductor HMMs in the infrared, demonstrating the great potential of doped semiconductors as a new class of plasmonic materials. The semiconductor HMMs have outstanding and flexible optical properties in the infrared, such as negative refraction and VPP modes with high mode indices. These unique properties of HMMs open new routes to manipulate light-matter interaction in the infrared. Also, it is easy to integrate semiconductor HMMs with other state-of-the-art semiconductor optoelectronic structures and devices including quantum wells, quantum dots, and quantum cascade lasers. Semiconductor HMMs may find wide applications in subwavelength imaging, spontaneous emission enhancement, environmental sensing, and biosensing.

6.2 Future Work

6.2.1 Strong Coupling

Chapter 4 focuses on VPP modes in different semiconductor HMMs. As briefly mentioned in Section 4.1, a potential application of HMMs is efficient quantum well infrared photodetectors and tunable intersubband light-emitting devices based on strong coupling between VPP modes and intersubband transition (ISBT) of multiple quantum wells (MQWs) [84].

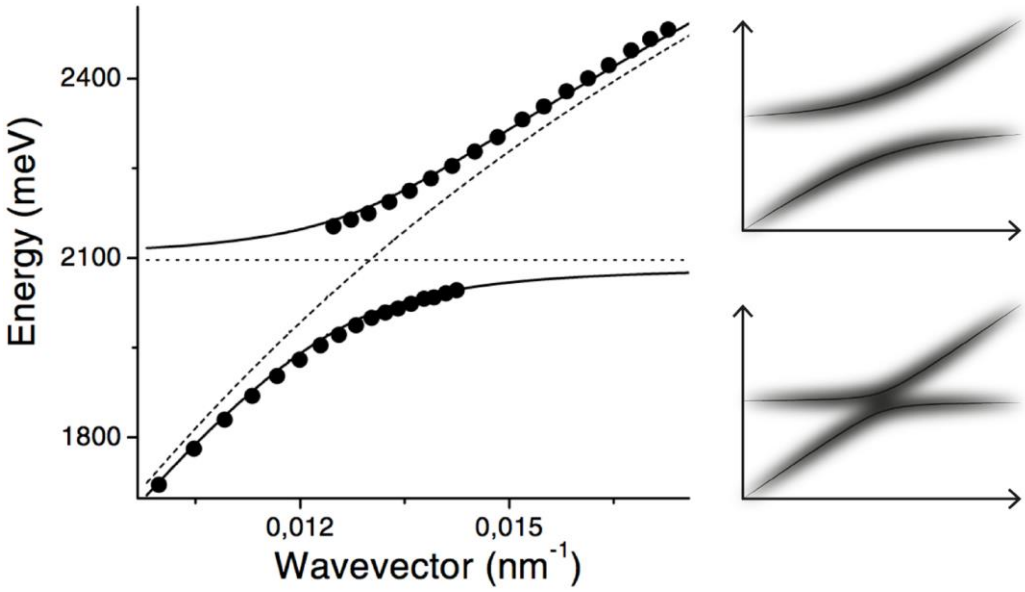

Figure 6.1: Left figure: strong coupling between a surface plasmon-polariton mode (diagonal dotted line) and an excitonic mode (horizontal dashed line). The energies of these two modes are shown as a function of in-plane wavevector. The system is a metal film (that supports the SPP mode) overcoated with a film of polymer containing aggregated dye molecules. The solid lines and the data (circles) show how these modes interact to produce an avoided crossing, the dashed lines show the dispersion expected in the absence of strong coupling. Figure reproduced with permission from [134]. Figures on the right: strong coupling regime can be defined as the splitting being large enough compared to the linewidths of the coupled states so that it is actually experimentally visible as in the upper picture; in the lower one, the splitting is hidden under the linewidths [135]. Reprint permission obtained from IOP Publishing

Strong coupling is an interaction between two distinct resonances in one system [136–139]. A critical feature of the strong coupling is the energy level splitting (Rabi splitting) which could be obtained by classical theory using two coupled harmonic oscillators model. Figure 6.1 shows the anti-crossing of strong coupling between an SPP mode and an excitonic mode. The new modes are neither purely SPP

modes or purely excitons. Instead, the new modes are mix modes of SPP modes and excitons.

It has been theoretically demonstrated that strong coupling could happen in HMM with MQWs embedded in the dielectric layer [84]. The designed structure is shown in Figure 6.2. In this structure, the two resonances that form strong coupling are VPP modes and the ISBT in the MQWs.

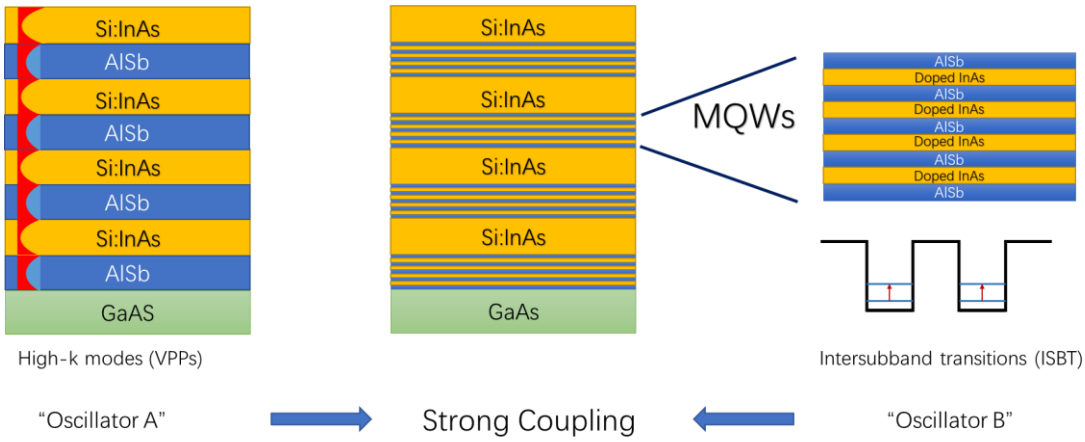

Figure 6.2: Schematic of designed strong coupling structure. The picture on the left shows the VPP modes in a Si:InAs/AlSb HMM. The picture on the right shows MQW structure and intersubband transition (ISBT). Picture in the middle shows the compound structure of MQWs embedded in an HMM.

The strong coupling of the designed structure is simulated by COMSOL as shown in Figure 6.3. In this structure, the ISBT is designed to be 20μm. The topological transition point, where the properties of HMMs transit from type I to type II area, is around 10μm. Strong coupling could be observed in type II region.

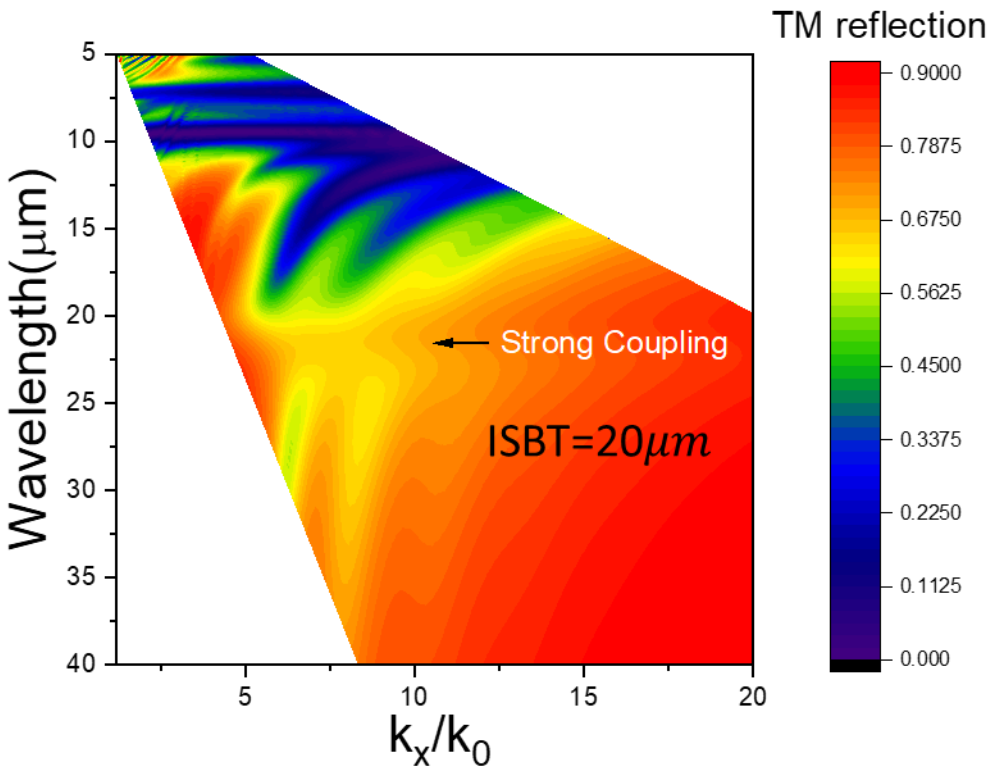

Figure 6.3: Simulated TM reflection of an HMM structure with MQWs as dielectric layers. Strong coupling resulting from the interaction of VPP modes and embedded MQWs is observed at intersubband transition (20μm). The simulation is done by COMSOL.

So far, the weak coupling in HMM has been reported in many papers [21,140,141]. However, the strong coupling has not been experimentally observed in HMMs. Currently, we are working on the growth and characterization of InAs/AlSb MQWs using our new MBE system (Apollo). After successfully growing the InAs/AlSb MQWs, we will embed MQWs into Si:InAs/AlSb HMM structures. The strong coupling is expected to be observed in TM reflection spectrum as shown in Figure 6.3. The experiment will demonstrate the integration of semiconductor HMMs

and quantum wells. The coupling between quantum wells and HMMs will also provide us with information about the electric field distribution of VPP modes. It will lay a solid foundation for creating new optoelectronic devices such as highly sensitive quantum well infrared photodetectors.

6.2.2 Rainbow Trapping

Rainbow trapping refers to the phenomenon of strong absorption over a wide wavelength range, which could help improve the efficiency of light energy utilization. Sawtooth HMM-based rainbow trapping could lead to the tunable broadband super absorber [142–144].

The mechanism behind rainbow trapping of HMM is based on the slowlight mode, which is defined as light at a very low group velocity and could even reach a complete standstill state. Figure 6.4 explains how broadband absorption is realized in a sawtooth HMM. In the figure, we could see that the energy flow first propagates downwardly and then whirls into the sawtooth HMM, forming vortexes mode that was trapped in the structure. Also, different wavelengths were trapped in different parts of the absorber. Shorter wavelength accumulated at the upper part of the structure while longer wavelength was trapped at the lower part of the absorber [143].

Related work on the visible range has been carried out by other people but no work has been done in the infrared yet. We have successfully used wet etching, a cost-effective and efficient method, to etch Si:InAs/InAs HMM to a sawtooth shape and more work will be done on other material systems (Si:InGaAs/InAlAs HMM and Si:InAs/AlSb HMM). The most challenging part is to find the etching recipe that could etch different semiconductors at similar rates. If the etching solution has

dramatically different etch rates for different layers, the topper layers with a faster etch rate might be completely etched away before the bottom layers got etched.

The rainbow trapping from semiconductor HMMs will demonstrate the potential of HMMs for creating super broadband absorber devices in infrared. In the future, sawtooth HMMs could be integrated with other optoelectronic devices to improve the efficiency of light utilization in the infrared.

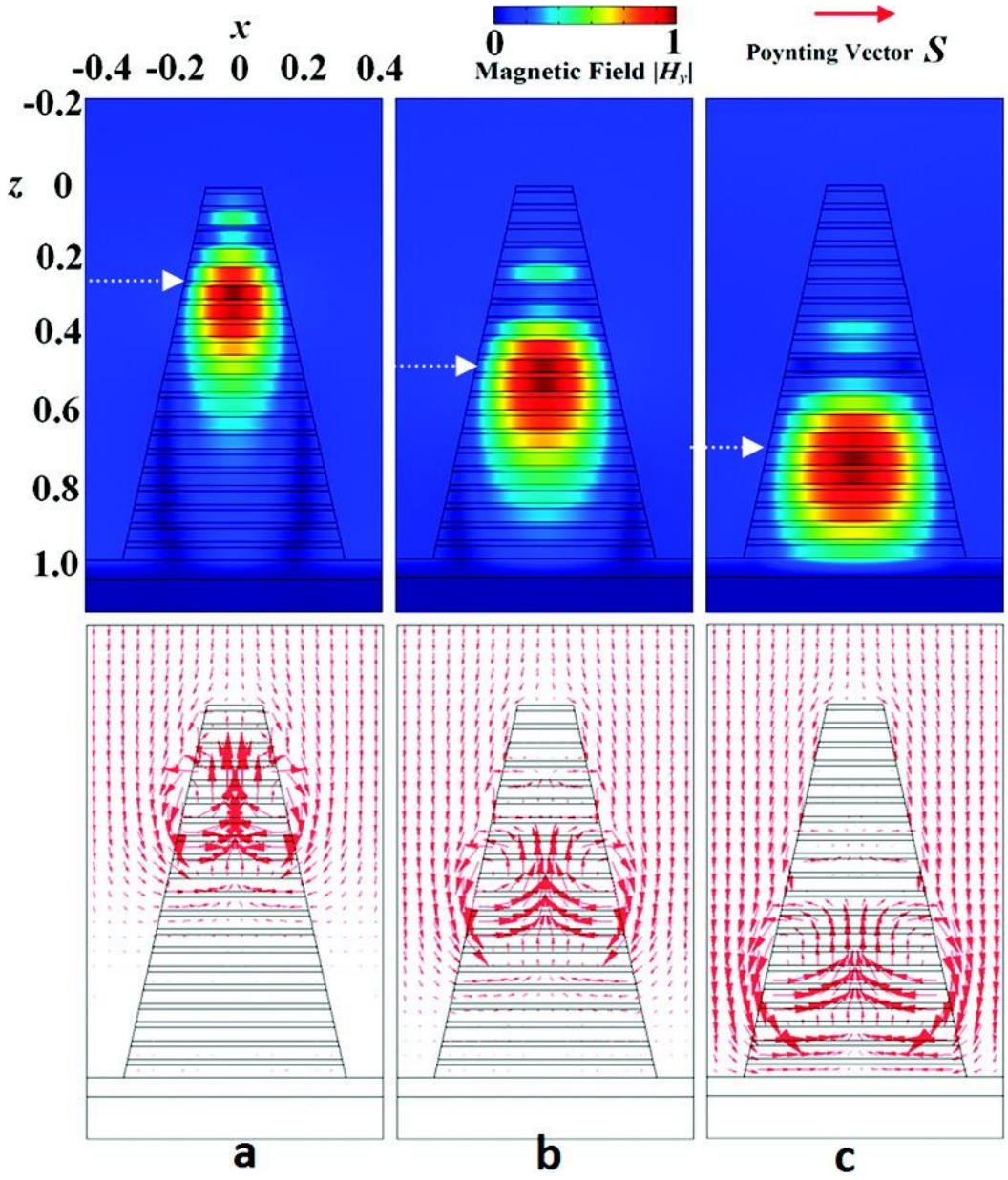

Figure 6.4: Distributions of magnetic field (color maps) and energy flow (arrow maps) for the sawtooth AMM absorber at different incident wavelengths: (a) λ_0 = 3.5 μm, (b) λ_0 = 4.5 μm, and (c) λ_0 = 5.5 μm. The vertical positions of field maxima are indicated with dotted arrows in the magnetic field plots [143]. Reuse permission obtained from the American Chemical Society.

REFERENCES

[1] Y. Liu and X. Zhang, Chem. Soc. Rev. **40**, 2494 (2011).

[2] P. Shekhar, J. Atkinson, and Z. Jacob, Nano Converg. **1**:14 (2014).

[3] N. I. Zheludev and Y. S. Kivshar, Nat. Mater. **11**, 917 (2012).

[4] V. M. Shalaev, Nat. Photonics **1**, 41 (2007).

[5] M. Kadic, G. W. Milton, M. van Hecke, and M. Wegener, Nat. Rev. Phys. **1**, 198 (2019).

[6] J. Yao, Z. Liu, Y. Liu, Y. Wang, C. Sun, G. Bartal, A. M. Stacy, and X. Zhang, Science **321**, 930 (2008).

[7] A. J. Hoffman, L. Alekseyev, S. S. Howard, K. J. Franz, D. Wasserman, V. a Podolskiy, E. E. Narimanov, D. L. Sivco, and C. Gmachl, Nat. Mater. **6**, 946 (2007).

[8] D. R. Smith, J. B. Pendry, and M. C. K. Wiltshire, Science (80-.). **305**, 788 LP (2004).

[9] J. B. Pendry, Phys. Rev. Lett. **85**, 3966 (2000).

[10] W. J. Padilla, D. N. Basov, and D. R. Smith, Mater. Today **9**, 28 (2006).

[11] A. J. Hoffman, V. A. Podolskiy, D. L. Sivco, and C. Gmachl, Opt. Express **16**, 16404 (2008).

[12] V. E. Babicheva, M. Y. Shalaginov, S. Ishii, A. Boltasseva, and A. V. Kildishev, Opt. Express **23**, 9681 (2015).

[13] Y. He, S. He, J. Gao, and X. Yang, J. Opt. Soc. Am. B **29**, 2559 (2012).

[14] J. Rho, Z. Ye, Y. Xiong, X. Yin, Z. Liu, H. Choi, G. Bartal, and X. Zhang, Nat. Commun. **1**, 143 (2010).

[15] Z. Jacob, L. V Alekseyev, and E. Narimanov, Opt. Express **14**, 8247 (2006).

[16] N. Fang and X. Zhang, Appl. Phys. Lett. **82**, 161 (2003).

[17] X. Huang, S. Xiao, D. Ye, J. Huangfu, Z. Wang, L. Ran, and L. Zhou, Opt. Express **18**, 10377 (2010).

[18] K. Feng, G. Harden, D. L. Sivco, and A. J. Hoffman, ACS Photonics **4**, 1621 (2017).

[19] I. Avrutsky, I. Salakhutdinov, J. Elser, and V. Podolskiy, Phys. Rev. B - Condens. Matter Mater. Phys. **75**, 2 (2007).

[20] L. Ferrari, D. Lu, D. Lepage, and Z. Liu, Opt. Express **22**, 4301 (2014).

[21] M. A. Noginov, H. Li, Y. A. Barnakov, D. Dryden, G. Nataraj, G. Zhu, C. E. Bonner, M. Mayy, Z. Jacob, and E. E. Narimanov, Opt. Lett. **35**, 1863 (2010).

[22] D. Lu, J. J. Kan, E. E. Fullerton, and Z. Liu, Nat. Nanotechnol. **9**, 48 (2014).

[23] P. Ginzburg, D. J. Roth, M. E. Nasir, P. Segovia, A. V Krasavin, J. Levitt, L. M. Hirvonen, B. Wells, K. Suhling, D. Richards, V. A. Podolskiy, and A. V Zayats, Light Sci. Appl. **6**, e16273 (2017).

[24] D. J. Roth, A. V Krasavin, A. Wade, W. Dickson, A. Murphy, S. Kéna-Cohen, R. Pollard, G. A. Wurtz, D. Richards, S. A. Maier, and A. V Zayats, ACS Photonics **4**, 2513 (2017).

[25] K. V. Sreekanth, Y. Alapan, M. ElKabbash, E. Ilker, M. Hinczewski, U. A. Gurkan, A. De Luca, and G. Strangi, Nat Mater **15**, 621 (2016).

[26] T. Chen, S. Li, and H. Sun, Sensors (Basel). **12**, 2742 (2012).

[27] M. A. Baqir, A. Farmani, T. Fatima, M. R. Raza, S. F. Shaukat, and A. Mir, Appl. Opt. **57**, 9447 (2018).

[28] A. A. Orlov, S. V. Zhukovsky, I. V. Iorsh, and P. A. Belov, Photonics Nanostructures - Fundam. Appl. **12**, 213 (2014).

[29] B. Wood, Comptes Rendus Phys. **10**, 379 (2009).

[30] A. a. Orlov, P. M. Voroshilov, P. a. Belov, and Y. S. Kivshar, Phys. Rev. B - Condens. Matter Mater. Phys. **84**, 1 (2011).

[31] V. Agranovich, Y. Shen, R. Baughman, and a. Zakhidov, Phys. Rev. B **69**, 1

(2004).

[32] B. Luk'yanchuk, N. I. Zheludev, S. a Maier, N. J. Halas, P. Nordlander, H. Giessen, and C. T. Chong, Nat Mater **9**, 707 (2010).

[33] N. Liu, H. Guo, L. Fu, S. Kaiser, H. Schweizer, and H. Giessen, Nat. Mater. **7**, 31 (2008).

[34] R. a Shelby, D. R. Smith, and S. Schultz, Science (80-.). **292**, 77 (2001).

[35] V. G. Veselago, Sov. Phys. Uspekhi **10**, 509 (1968).

[36] J. B. Pendry, a. J. Holden, D. J. Robbins, and W. J. Stewart, IEEE Trans. Microw. Theory Tech. **47**, 2075 (1999).

[37] D. Smith, W. Padilla, D. Vier, S. Nemat-Nasser, and S. Schultz, Phys. Rev. Lett. **84**, 4184 (2000).

[38] a. Movchan and S. Guenneau, Phys. Rev. B **70**, 125116 (2004).

[39] P. Gay-Balmaz and O. J. F. Martin, J. Appl. Phys. **92**, 2929 (2002).

[40] R. Marqués, J. Martel, F. Mesa, and F. Medina, Phys. Rev. Lett. **89**, 183901 (2002).

[41] N. Meinzer, M. Ruther, S. Linden, C. M. Soukoulis, G. Khitrova, J. Hendrickson, J. D. Olitzky, H. M. Gibbs, and M. Wegener, Opt. Express **18**, 24140 (2010).

[42] W. N. Hardy and L. A. Whitehead, Rev. Sci. Instrum. **52**, 213 (1981).

[43] K. B. Alici and E. Ozbay, J. Appl. Phys. **101**, 83104 (2007).

[44] H. O. Moser, B. D. F. Casse, O. Wilhelmi, and B. T. Saw, Phys. Rev. Lett. **94**, 63901 (2005).

[45] J. B. Pendry, Science **306**, 1353 (2004).

[46] V. Podolskiy and E. Narimanov, Phys. Rev. B **71**, 201101 (2005).

[47] Y. Guo, W. Newman, C. L. Cortes, and Z. Jacob, Adv. Optoelectron. **2012**, 1 (2012).

[48] C. L. Cortes, W. Newman, S. Molesky, and Z. Jacob, J. Opt. **14**, 063001 (2012).

[49] E. E. Narimanov and A. V Kildishev, Nat. Photonics **9**, 214 (2015).

[50] K. Korzeb, M. Gajc, and D. A. Pawlak, Opt. Express **23**, 25406 (2015).

[51] S. Guan, S. Y. Huang, Y. Yao, and S. A. Yang, Phys. Rev. B **95**, 165436 (2017).

[52] J. D. Caldwell, A. V Kretinin, Y. Chen, V. Giannini, M. M. Fogler, Y. Francescato, C. T. Ellis, J. G. Tischler, C. R. Woods, A. J. Giles, M. Hong, K. Watanabe, T. Taniguchi, S. A. Maier, and K. S. Novoselov, Nat. Commun. **5**, 5221 (2014).

[53] L. V Brown, M. Davanco, Z. Sun, A. Kretinin, Y. Chen, J. R. Matson, I. Vurgaftman, N. Sharac, A. J. Giles, M. M. Fogler, T. Taniguchi, K. Watanabe, K. S. Novoselov, S. A. Maier, A. Centrone, and J. D. Caldwell, Nano Lett. **18**, 1628 (2018).

[54] L. V. Alekseyev, V. Podolskiy, and E. E. Narimanov, *Homogeneous Hyperbolic Systems for Terahertz and Far-Infrared Frequencies* (2012).

[55] M. Esslinger, R. Vogelgesang, N. Talebi, W. Khunsin, P. Gehring, S. de Zuani, B. Gompf, and K. Kern, ACS Photonics **1**, 1285 (2014).

[56] O. Kidwai, S. V Zhukovsky, and J. E. Sipe, Phys. Rev. A **85**, 53842 (2012).

[57] J. Hao and L. Zhou, Phys. Rev. B - Condens. Matter Mater. Phys. **77**, 1 (2008).

[58] V. A. Podolskiy, J. Elser, I. Salakhutdinov, and I. Avrutsky, in *2007 Quantum Electron. Laser Sci. Conf.* (2007), pp. 1–2.

[59] X. Zhang and Y. Wu, Sci. Rep. **5**, 7892 (2015).

[60] P. Lalanne and D. Lemercier-lalanne, J. Mod. Opt. **43**, 2063 (1996).

[61] P. Lalanne and J.-P. Hugonin, J. Opt. Soc. Am. A **15**, 1843 (1998).

[62] G. T. Papadakis, P. Yeh, and H. A. Atwater, Phys. Rev. B **91**, 155406 (2015).

[63] I. I. Smolyaninov, Hyperbolic Metamaterials 2 (2018).

[64] Z. Liu, H. Lee, Y. Xiong, C. Sun, and X. Zhang, Science **315**, 1686 (2012).

[65] P. Huo, S. Zhang, Y. Liang, Y. Lu, and T. Xu, Adv. Opt. Mater. **7**, 1801616 (2019).

[66] Z. Jacob, J.-Y. Kim, G. V Naik, A. Boltasseva, E. E. Narimanov, and V. M. Shalaev, Appl. Phys. B **100**, 215 (2010).

[67] T. Tumkur, G. Zhu, P. Black, Y. A. Barnakov, C. E. Bonner, and M. A. Noginov, Appl. Phys. Lett. **99**, 151115 (2011).

[68] Y. J. Chabal, Surf. Sci. Rep. **8**, 211 (1988).

[69] B. Stuart, Kirk-Othmer Encycl. Chem. Technol. 1 (2015).

[70] G. D. Dereniak, E. L., Boreman, *Infrared Detectors and Systems* (1996).

[71] M. Vollmer and K.-P. Möllmann, *Infrared Thermal Imaging: Fundamentals, Research and Applications* (Wiley, 2017).

[72] Y. Liu, G. Bartal, and X. Zhang, Opt. Express **16**, 15439 (2008).

[73] Z. Liu, H. Lee, Y. Xiong, C. Sun, and X. Zhang, Science (80-.). **315**, 1686 (2007).

[74] A. V Chshelokova, P. V Kapitanova, A. N. Poddubny, D. S. Filonov, A. P. Slobozhanyuk, Y. S. Kivshar, and P. A. Belov, J. Appl. Phys. **112**, 73116 (2012).

[75] K. V Sreekanth, A. De Luca, and G. Strangi, J. Opt. **16**, 105103 (2014).

[76] S. Law, R. Liu, and D. Wasserman, J. Vac. Sci. Technol. B, Nanotechnol. Microelectron. Mater. Process. Meas. Phenom. **32**, 052601 (2014).

[77] S. Law, L. Yu, and D. Wasserman, J. Vac. Sci. Technol. B Microelectron. Nanom. Struct. **31**, 03C121 (2013).

[78] S. Law, V. Podolskiy, and D. Wasserman, Nanophotonics **2**, 103 (2013).

[79] S. Law, L. Yu, A. Rosenberg, and D. Wasserman, Nano Lett. **13**, 4569 (2013).

[80] M. Shahzad, G. Medhi, R. E. Peale, W. R. Buchwald, J. W. Cleary, R. Soref, G. D. Boreman, and O. Edwards, J. Appl. Phys. **110**, 123105 (2011).

[81] J. C. Ginn, R. L. Jarecki, E. a. Shaner, and P. S. Davids, J. Appl. Phys. **110**, 1 (2011).

[82] Y. Zhong, S. D. Malagari, T. Hamilton, and D. Wasserman, J. Nanophotonics **9**, 093791 (2015).

[83] K. Feng, D. L. Sivco, and A. J. Hoffman, Opt. Express **26**, 4382 (2018).

[84] P. Shekhar and Z. Jacob, Phys. Rev. B - Condens. Matter Mater. Phys. **90**, 1 (2014).

[85] M. A. Herman and H. Sitter, in edited by M. A. Herman and H. Sitter (Springer Berlin Heidelberg, Berlin, Heidelberg, 1989), pp. 1–28.

[86] R. A. Kubiak, S. M. Newstead, and P. Sullivan, in edited by R. F. C. B. T.-M. B. E. Farrow (William Andrew Publishing, Park Ridge, NJ, 1995), pp. 1–113.

[87] E. C. Larkins and J. S. Harris, in edited by R. F. C. B. T.-M. B. E. Farrow (William Andrew Publishing, Park Ridge, NJ, 1995), pp. 114–274.

[88] M. B. Panish and H. Temkin, in edited by R. F. C. B. T.-M. B. E. Farrow (William Andrew Publishing, Park Ridge, NJ, 1995), pp. 275–343.

[89] E. Tournié, A. Castellano, K. Madiomanana, G. Narcy, A. Garreau, F. Lelarge, J.-B. Rodriguez, and L. Cerutti, in edited by M. B. T.-M. B. E. (Second E. Henini (Elsevier, 2018), pp. 625–635.

[90] M. Guina, S. M. Wang, and A. Aho, in edited by M. B. T.-M. B. E. (Second E. Henini (Elsevier, 2018), pp. 73–94.

[91] S. Zhao and Z. Mi, in edited by M. B. T.-M. B. E. (Second E. Henini (Elsevier, 2018), pp. 115–133.

[92] D. J. As and K. Lischka, in edited by M. B. T.-M. B. E. (Second E. Henini (Elsevier, 2018), pp. 95–114.

[93] M. Myronov, in edited by M. B. T.-M. B. E. (Second E. Henini (Elsevier, 2018), pp. 37–54.

[94] T. Ginley, Y. Wang, and S. Law, Crystals **6**, 154 (2016).

[95] D. G. Schlom, APL Mater. **3**, 62403 (2015).

[96] O. Bierwagen, M. E. White, M.-Y. Tsai, and J. S. Speck, in edited by M. B. T.-M. B. E. Henini (Elsevier, Oxford, 2013), pp. 347–367.

[97] D. Wei, C. Harris, C. C. Bomberger, J. Zhang, J. Zide, and S. Law, Opt. Express **24**, 8735 (2016).

[98] M. Tschikin, S.-A. Biehs, R. Messina, and P. Ben-Abdallah, J. Opt. **15**, 105101 (2013).

[99] L. Sun, Z. Li, T. S. Luk, X. Yang, and J. Gao, Phys. Rev. B **91**, 195147 (2015).

[100] A. A. Krokhin, J. Arriaga, L. N. Gumen, and V. P. Drachev, Phys. Rev. B **93**, 075418 (2016).

[101] S. V Zhukovsky, O. Kidwai, and J. E. Sipe, Opt. Express **21**, 14982 (2013).

[102] N. Vasilantonakis, M. E. Nasir, W. Dickson, G. A. Wurtz, and A. V. Zayats, Laser Photonics Rev. **9**, 345 (2015).

[103] S. Ishii, A. V Kildishev, E. Narimanov, V. M. Shalaev, and V. P. Drachev, Laser Photon. Rev. **7**, 265 (2013).

[104] S. V Zhukovsky, A. A. Orlov, V. E. Babicheva, A. V Lavrinenko, and J. E. Sipe, Phys. Rev. A **90**, 13801 (2014).

[105] S. V. Zhukovsky, A. Andryieuski, J. E. Sipe, and A. V. Lavrinenko, Phys. Rev. B **90**, 155429 (2014).

[106] J. M. Pitarke, V. M. Silkin, E. V Chulkov, and P. M. Echenique, Reports Prog. Phys. **70**, 1 (2006).

[107] A. V Zayats, I. I. Smolyaninov, and A. A. Maradudin, Phys. Rep. **408**, 131 (2005).

[108] J. Zhang, L. Zhang, and W. Xu, J. Phys. D. Appl. Phys. **45**, 113001 (2012).

[109] K. V. Sreekanth, A. De Luca, and G. Strangi, Sci. Rep. **3**, 3291 (2013).

[110] D. Wei, C. Harris, and S. Law, Opt. Mater. Express **7**, 2672 (2017).

[111] S. Law, D. C. Adams, A. M. Taylor, and D. Wasserman, Opt. Express **20**, 12155 (2012).

[112] M. Cardona, Phys. Rev. **121**, 752 (1961).

[113] W. G. Spitzer and H. Y. Fan, Phys. Rev. **106**, 882 (1957).

[114] P. Sohr, D. Wei, S. Tomasulo, M. K. Yakes, and S. Law, ACS Photonics **5**, 4003 (2018).

[115] E. F. Schubert, G. H. Gilmer, R. F. Kopf, and H. S. Luftman, Phys. Rev. B **46**, 15078 (1992).

[116] A. Kawano, I. Konomi, H. Azuma, T. Hioki, and S. Noda, J. Appl. Phys. **74**,

4265 (1993).

[117] V. D. Dasika, E. M. Krivoy, H. P. Nair, S. J. Maddox, K. W. Park, D. Jung, M. L. Lee, E. T. Yu, and S. R. Bank, Appl. Phys. Lett. **105**, 253104 (2014).

[118] D. Fan, Z. Zeng, V. G. Dorogan, Y. Hirono, C. Li, Y. I. Mazur, S.-Q. Yu, S. R. Johnson, Z. M. Wang, and G. J. Salamo, J. Mater. Sci. Mater. Electron. **24**, 1635 (2013).

[119] M. R. Pillai, S.-S. Kim, S. T. Ho, and S. A. Barnett, J. Vac. Sci. Technol. B Microelectron. Nanom. Struct. Process. Meas. Phenom. **18**, 1232 (2000).

[120] E. M. Anderson, A. M. Lundquist, W. L. Sarney, S. P. Svensson, P. J. Carrington, C. Pearson, and J. M. Millunchick, J. Appl. Phys. **116**, 14901 (2014).

[121] P. T. Webster, A. J. Shalindar, N. A. Riordan, C. Gogineni, H. Liang, A. R. Sharma, and S. R. Johnson, J. Appl. Phys. **119**, 225701 (2016).

[122] E. C. Young, S. Tixier, and T. Tiedje, J. Cryst. Growth **279**, 316 (2005).

[123] R. Salas, S. Guchhait, K. M. McNicholas, S. D. Sifferman, V. D. Dasika, D. Jung, E. M. Krivoy, M. L. Lee, and S. R. Bank, Appl. Phys. Lett. **108**, 182102 (2016).

[124] S. Tixier, M. Adamcyk, E. C. Young, J. H. Schmid, and T. Tiedje, J. Cryst. Growth **251**, 449 (2003).

[125] A. J. Ptak, D. A. Beaton, and A. Mascarenhas, J. Cryst. Growth **351**, 122 (2012).

[126] T. Liu, S. Chandril, A. J. Ptak, D. Korakakis, and T. H. Myers, J. Cryst. Growth **304**, 402 (2007).

[127] Y. Zhong, P. B. Dongmo, J. P. Petropoulos, and J. M. O. Zide, Appl. Phys. Lett. **100**, 112110 (2012).

[128] G. Feng, K. Oe, and M. Yoshimoto, J. Cryst. Growth **301**–**302**, 121 (2007).

[129] S. Flores, D. F. Reyes, V. Braza, R. D. Richards, F. Bastiman, T. Ben, N. Ruiz-Marín, J. P. R. David, and D. González, Appl. Surf. Sci. **485**, 29 (2019).

[130] P. T. Webster, N. A. Riordan, C. Gogineni, S. Liu, J. Lu, X.-H. Zhao, D. J. Smith, Y.-H. Zhang, and S. R. Johnson, J. Vac. Sci. Technol. B **32**, 02C120 (2014).

[131] C. Domke, P. Ebert, M. Heinrich, and K. Urban, Phys. Rev. B **54**, 10288 (1996).

[132] S. Muto, S. Takeda, M. Hirata, K. Fujii, and K. Ibe, Philos. Mag. A **66**, 257 (1992).

[133] C. Domke, P. Ebert, M. Heinrich, and K. Urban, Phys. Rev. B **54**, 10288 (1996).

[134] J. Bellessa, C. Bonnand, J. C. Plenet, and J. Mugnier, Phys. Rev. Lett. **93**, 36404 (2004).

[135] P. Törmä and W. L. Barnes, Reports Prog. Phys. **78**, 013901 (2015).

[136] A. González-Tudela, P. A. Huidobro, L. Martín-Moreno, C. Tejedor, and F. J. García-Vidal, Phys. Rev. Lett. **110**, 126801 (2013).

[137] L. Novotny, Am. J. Phys. **78**, 1199 (2010).

[138] D. J. Shelton, I. Brener, J. C. Ginn, M. B. Sinclair, D. W. Peters, K. R. Coffey, and G. D. Boreman, Nano Lett. **11**, 2104 (2011).

[139] Y. C. Jun, J. Reno, T. Ribaudo, E. Shaner, J.-J. Greffet, S. Vassant, F. Marquier, M. Sinclair, and I. Brener, Nano Lett. **13**, 5391 (2013).

[140] S.-Q. Zhai, J.-Q. Liu, F.-Q. Liu, and Z.-G. Wang, Appl. Phys. Lett. **100**, (2012).

[141] Z. Jacob, I. I. Smolyaninov, and E. E. Narimanov, Appl. Phys. Lett. **100**, 8100 (2012).

[142] H. Hu, D. Ji, X. Zeng, K. Liu, and Q. Gan, Sci. Rep. **3**, 1249 (2013).

[143] Y. Cui, K. H. Fung, J. Xu, H. Ma, Y. Jin, S. He, and N. X. Fang, Nano Lett. **12**, 1443 (2012).

[144] D. Ji, H. Song, X. Zeng, H. Hu, K. Liu, N. Zhang, and Q. Gan, Sci. Rep. **4**, 4498 (2014).

Appendix

FIGURE REPRINT PERMISSIONS

Permission for Figure 1.1, 1.6, 1.7

Copyright information

© Shekhar et al.; licensee Springer 2014

This article is published under license to BioMed Central Ltd. This is an Open Access article distributed under the terms of the Creative Commons Attribution License (http://creativecommons.org/licenses/by/2.0), which permits unrestricted use, distribution, and reproduction in any medium, provided the original work is properly credited.

Permission for Figure 1.2

License Details

This Agreement between Dongxia Wei ("You") and The American Association for the Advancement of Science ("The American Association for the Advancement of Science") consists of your license details and the terms and conditions provided by The American Association for the Advancement of Science and Copyright Clearance Center.

Print Copy

License Number	4662760595593
License date	Sep 05, 2019
Licensed Content Publisher	The American Association for the Advancement of Science
Licensed Content Publication	Science
Licensed Content Title	Experimental Verification of a Negative Index of Refraction
Licensed Content Author	R. A. Shelby,D. R. Smith,S. Schultz
Licensed Content Date	Apr 6, 2001
Licensed Content Volume	292
Licensed Content Issue	5514
Volume number	292
Issue number	5514
Type of Use	Thesis / Dissertation
Requestor type	Scientist/individual at a research institution
Format	Print and electronic
Portion	Figure
Number of figures/tables	1
Order reference number	
Title of your thesis / dissertation	Semiconductor Hyperbolic Metamaterials for the Infrared
Expected completion date	Sep 2019
Estimated size(pages)	1
Requestor Location	Dongxia Wei 24 Marvin D8 Apt C7 NEWARK, DE 19713 United States Attn: Dongxia Wei
Total	**0.00 USD**

BACK

Permission for Figure 1.3 and Figure 3.13

Order Completed

Thank you for your order.

This Agreement between Dongxia Wei ("You") and Springer Nature ("Springer Nature") consists of your license details and the terms and conditions provided by Springer Nature and Copyright Clearance Center.

Your confirmation email will contain your order number for future reference.

printable details

License Number	4673921159976
License date	Sep 21, 2019
Licensed Content Publisher	Springer Nature
Licensed Content Publication	Nature Materials
Licensed Content Title	Negative refraction in semiconductor metamaterials
Licensed Content Author	Anthony J. Hoffman et al
Licensed Content Date	Oct 14, 2007
Licensed Content Volume	6
Licensed Content Issue	12
Type of Use	Thesis/Dissertation
Requestor type	academic/university or research institute
Format	print and electronic
Portion	figures/tables/illustrations
Number of figures/tables/illustrations	2
High-res required	no
Will you be translating?	no
Circulation/distribution	5000 - 9999
Author of this Springer Nature content	no
Title	Semiconductor Hyperbolic Metamaterials for the Infrared
Institution name	University of Delaware
Expected presentation date	Sep 2019
Portions	Figure 1 and Figure 3
Requestor Location	Dongxia Wei 24 Marvin D8 Apt C7 NEWARK, DE 19713 United States Attn: Dongxia Wei
Total	0.00 USD

ORDER MORE CLOSE WINDOW

Permission for Figure 1.4

American Physical Society Reuse and Permissions License

05-Sep-2019

This license agreement between the American Physical Society ("APS") and Dongxia Wei ("You") consists of your license details and the terms and conditions provided by the American Physical Society and SciPris.

Licensed Content Information

License Number:	**RNP/19/SEP/018503**
License date:	05-Sep-2019
DOI:	10.1103/PhysRevB.71.201101
Title:	Strongly anisotropic waveguide as a nonmagnetic left-handed system
Author:	Viktor A. Podolskiy and Evgenii E. Narimanov
Publication:	Physical Review B
Publisher:	American Physical Society
Cost:	USD $ 0.00

Request Details

Does your reuse require significant modifications: No

Specify intended distribution locations:	United States
Reuse Category:	Reuse in a thesis/dissertation
Requestor Type:	Student
Items for Reuse:	Figures/Tables
Number of Figure/Tables:	1
Figure/Tables Details:	Figure 1
Format for Reuse:	Print and Electronic
Total number of print copies:	Up to 1000

Information about New Publication:

University/Publisher:	University of Delaware
Title of dissertation/thesis:	Semiconductor hyperbolic metamaterials for infrared
Author(s):	Dongxia Wei
Expected completion date:	Nov. 2019

License Requestor Information

Name:	Dongxia Wei
Affiliation:	Individual
Email Id:	wdx@udel.edu
Country:	United States

Permission for Figure 1.8

License Details

This Agreement between Dongxia Wei ("You") and Springer Nature ("Springer Nature") consists of your license details and the terms and conditions provided by Springer Nature and Copyright Clearance Center.

Print Copy

License Number	4662791147726
License date	Sep 05, 2019
Licensed Content Publisher	Springer Nature
Licensed Content Publication	Nature Nanotechnology
Licensed Content Title	Enhancing spontaneous emission rates of molecules using nanopatterned multilayer hyperbolic metamaterials
Licensed Content Author	Dylan Lu, Jimmy J. Kan, Eric E. Fullerton, Zhaowei Liu
Licensed Content Date	Jan 6, 2014
Licensed Content Volume	9
Licensed Content Issue	1
Type of Use	Thesis/Dissertation
Requestor type	academic/university or research institute
Format	print and electronic
Portion	figures/tables/illustrations
Number of figures/tables/illustrations	1
High-res required	no
Will you be translating?	no
Circulation/distribution	5000 - 9999
Author of this Springer Nature content	no
Title	Semiconductor Hyperbolic Metamaterials for the Infrared
Institution name	University of Delaware
Expected presentation date	Sep 2019
Portions	Figure 2
Requestor Location	Dongxia Wei 24 Marvin D8 Apt C7 NEWARK, DE 19713 United States Attn: Dongxia Wei
Total	**0.00 USD**

Permission for Figure 1.9

AIP PUBLISHING LICENSE TERMS AND CONDITIONS

Sep 21, 2019

This Agreement between Dongxia Wei ("You") and AIP Publishing ("AIP Publishing") consists of your license details and the terms and conditions provided by AIP Publishing and Copyright Clearance Center.

License Number	4662640212994
License date	Sep 05, 2019
Licensed Content Publisher	AIP Publishing
Licensed Content Publication	Journal of Vacuum Science & Technology B
Licensed Content Title	Epitaxial growth of engineered metals for mid-infrared plasmonics
Licensed Content Author	Stephanie Law, Lan Yu, Daniel Wasserman
Licensed Content Date	May 1, 2013
Licensed Content Volume	31
Licensed Content Issue	3
Type of Use	Thesis/Dissertation
Requestor type	Student
Format	Print and electronic
Portion	Figure/Table
Number of figures/tables	1
Title of your thesis / dissertation	Semiconductor Hyperbolic Metamaterials for the Infrared
Expected completion date	Sep 2019
Estimated size (number of pages)	1
Requestor Location	Dongxia Wei 24 Marvin D8 Apt C7 NEWARK, DE 19713 United States Attn: Dongxia Wei
Total	**0.00 USD**

Permission for Figure 3.2, 3.3, 3.4, 3.5, 3.6, 3.7, 3.14, 3.15, 4.8, 4.9, 4.10, 4.11, 4.15 and Table 3.1

pubscopyright <copyright@osa.org> Thu, Mar 7, 2019 at 2:03 PM
To: Dongxia Wei <wdx@udel.edu>, pubscopyright <copyright@osa.org>

Dear Dongxia Wei,

Thank you for contacting The Optical Society.

For the use of material from **[1]** D. Wei, C. Harris, C. C. Bomberger, J. Zhang, J. Zide, and S. Law, "Single-material semiconductor hyperbolic metamaterials," Opt. Express 24, 8735-8745 (2016) and **[2]** Dongxia Wei, Christian Harris, and Stephanie Law, "Volume plasmon polaritons in semiconductor hyperbolic metamaterials," Opt. Mater. Express 7, 2672-2681 (2017):

> Because you are the author of the source paper from which you wish to reproduce material, OSA considers your requested use of its copyrighted materials to be permissible within the author rights granted in the Copyright Transfer Agreement submitted by the requester on acceptance for publication of his/her manuscript. If the entire article is being included, it is requested that the **Author Accepted Manuscript** (or preprint) version be the version included within the thesis and that a complete citation of the original material be included in any publication. This permission assumes that the material was not reproduced from another source when published in the original publication.

The **Author Accepted Manuscript** version is the preprint version of the article that was accepted for publication but not yet prepared and/or formatted by The Optical Society or its vendors.

Permission for Figure 4.2

THE AMERICAN ASSOCIATION FOR THE ADVANCEMENT OF SCIENCE LICENSE TERMS AND CONDITIONS

Sep 21, 2019

This Agreement between Dongxia Wei ("You") and The American Association for the Advancement of Science ("The American Association for the Advancement of Science") consists of your license details and the terms and conditions provided by The American Association for the Advancement of Science and Copyright Clearance Center.

License Number	4673930920815
License date	Sep 21, 2019
Licensed Content Publisher	The American Association for the Advancement of Science
Licensed Content Publication	Science
Licensed Content Title	Far-Field Optical Hyperlens Magnifying Sub-Diffraction-Limited Objects
Licensed Content Author	Zhaowei Liu,Hyesog Lee,Yi Xiong,Cheng Sun,Xiang Zhang
Licensed Content Date	Mar 23, 2007
Licensed Content Volume	315
Licensed Content Issue	5819
Volume number	315
Issue number	5819
Type of Use	Thesis / Dissertation
Requestor type	Scientist/individual at a research institution
Format	Print and electronic
Portion	Figure
Number of figures/tables	1
Order reference number	
Title of your thesis / dissertation	Semiconductor Hyperbolic Metamaterials for the Infrared
Expected completion date	Sep 2019
Estimated size(pages)	1
Requestor Location	Dongxia Wei 28 Marvin Drive Apt C7 NEWARK, DE 19713 United States Attn: Dongxia Wei
Total	0.00 USD

Permission for Figure 4.3

American Physical Society Reuse and Permissions License

21-Sep-2019

This license agreement between the American Physical Society ("APS") and Dongxia Wei ("You") consists of your license details and the terms and conditions provided by the American Physical Society and SciPris.

Licensed Content Information

License Number:	**RNP/19/SEP/018936**
License date:	21-Sep-2019
DOI:	10.1103/PhysRevB.90.045313
Title:	Strong coupling in hyperbolic metamaterials
Author:	Prashant Shekhar and Zubin Jacob
Publication:	Physical Review B
Publisher:	American Physical Society
Cost:	USD $ 0.00

Request Details

Does your reuse require significant modifications: No

Specify intended distribution locations:	United States
Reuse Category:	Reuse in a thesis/dissertation
Requestor Type:	Student
Items for Reuse:	Figures/Tables
Number of Figure/Tables:	2
Figure/Tables Details:	Figure 1 and Figure 5
Format for Reuse:	Print and Electronic
Total number of print copies:	Up to 1000

Information about New Publication:

University/Publisher:	University of Delaware
Title of dissertation/thesis:	Semiconductor Hyperbolic Metamaterials for the Infrared
Author(s):	Dongxia Wei
Expected completion date:	Nov. 2019

License Requestor Information

Name:	Dongxia Wei
Affiliation:	Individual
Email Id:	wdx@udel.edu
Country:	United States

Permission for Figure 4.4

Journal of Physics D : Applied Physics

Billing Status: **N/A**

Order detail ID:	72015006
ISSN:	0022-3727
Publication Type:	Journal
Volume:	
Issue:	
Start page:	
Publisher:	IOP Publishing
Author/Editor:	Institute of Physics and the Physical Society ; Institute of Physics (Great Britain)

Permission Status: **Granted**

Permission type: Republish or display content

Type of use: Thesis/Dissertation

Order License Id: 4674260031074

Hide details

Requestor type	Academic institution
Format	Print, Electronic
Portion	image/photo
Number of images/photos requested	2
The requesting person/organization	Dongxia Wei
Title or numeric reference of the portion(s)	Figure 2 and Figure 3
Title of the article or chapter the portion is from	Surface plasmon polaritons: physics and applications
Editor of portion(s)	N/A
Author of portion(s)	Junxi Zhang, Lide Zhang and Wei Xu
Volume of serial or monograph	45
Page range of portion	3-4
Publication date of portion	27 February 2012
Rights for	Main product
Duration of use	Life of current edition
Creation of copies for the disabled	no
With minor editing privileges	no
For distribution to	Worldwide
In the following language(s)	Original language of publication
With incidental promotional use	no
Lifetime unit quantity of new product	Up to 499
Title	Semiconductor Hyperbolic Metamaterials for the Infrared
Institution name	University of Delaware
Expected presentation date	Sep 2019

Permission for Figure 4.5 and Figure 4.6

American Physical Society Reuse and Permissions License

15-Mar-2019

This license agreement between the American Physical Society ("APS") and Dongxia Wei ("You") consists of your license details and the terms and conditions provided by the American Physical Society and SciPris.

Licensed Content Information

License Number:	**RNP/19/MAR/012929**
License date:	15-Mar-2019
DOI:	10.1103/PhysRevB.75.241402
Title:	Highly confined optical modes in nanoscale metal-dielectric multilayers
Author:	Ivan Avrutsky et al.
Publication:	Physical Review B
Publisher:	American Physical Society
Cost:	USD $ 0.00

Request Details

Does your reuse require significant modifications: No

Specify intended distribution locations:	United States
Reuse Category:	Reuse in a thesis/dissertation
Requestor Type:	Student
Items for Reuse:	Figures/Tables
Number of Figure/Tables:	4
Figure/Tables Details:	Figure 1,2,3,4
Format for Reuse:	Print and Electronic
Total number of print copies:	Up to 1000

Information about New Publication:

University/Publisher:	University of Delaware
Title of dissertation/thesis:	Semiconductor Hyperbolic Metamaterials for the Infrared
Author(s):	Dongxia Wei
Expected completion date:	Jun. 2019

License Requestor Information

Name:	Dongxia Wei
Affiliation:	Individual
Email Id:	wdx@udel.edu
Country:	United States

Permission for Figure 4.16 and Figure 4.17

Copyright Clearance Center RightsLink®

Home | Account Info | Help

ACS Publications
Most Trusted. Most Cited. Most Read.

Title: Simultaneous Large Mode Index and High Quality Factor in Infrared Hyperbolic Metamaterials

Author: Patrick Sohr, Dongxia Wei, Stephanie Tomasulo, et al

Publication: ACS Photonics

Publisher: American Chemical Society

Date: Oct 1, 2018

Copyright © 2018, American Chemical Society

Logged in as:
Dongxia Wei
Account #:
3001058898
LOGOUT

PERMISSION/LICENSE IS GRANTED FOR YOUR ORDER AT NO CHARGE

This type of permission/license, instead of the standard Terms & Conditions, is sent to you because no fee is being charged for your order. Please note the following:

- Permission is granted for your request in both print and electronic formats, and translations.
- If figures and/or tables were requested, they may be adapted or used in part.
- Please print this page for your records and send a copy of it to your publisher/graduate school.
- Appropriate credit for the requested material should be given as follows: "Reprinted (adapted) with permission from (COMPLETE REFERENCE CITATION). Copyright (YEAR) American Chemical Society." Insert appropriate information in place of the capitalized words.
- One-time permission is granted only for the use specified in your request. No additional uses are granted (such as derivative works or other editions). For any other uses, please submit a new request.

If credit is given to another source for the material you requested, permission must be obtained from that source.

Permission for Figure 6.1

American Physical Society Reuse and Permissions License

26-Aug-2019

This license agreement between the American Physical Society ("APS") and Dongxia Wei ("You") consists of your license details and the terms and conditions provided by the American Physical Society and SciPris.

Licensed Content Information

License Number:	**RNP/19/AUG/018125**
License date:	26-Aug-2019
DOI:	10.1103/PhysRevLett.93.036404
Title:	Strong Coupling between Surface Plasmons and Excitons in an Organic Semiconductor
Author:	J. Bellessa et al.
Publication:	Physical Review Letters
Publisher:	American Physical Society
Cost:	USD $ 0.00

Request Details

Does your reuse require significant modifications: No

Specify intended distribution locations:	Worldwide
Reuse Category:	Reuse in a thesis/dissertation
Requestor Type:	Student
Items for Reuse:	Figures/Tables
Number of Figure/Tables:	1
Figure/Tables Details:	Figure 4
Format for Reuse:	Print and Electronic
Total number of print copies:	Up to 1000

Information about New Publication:

University/Publisher:	University of Delaware
Title of dissertation/thesis:	Semiconductor Hyperbolic metamaterials for the infrared
Author(s):	Dongxia Wei
Expected completion date:	Nov. 2019

License Requestor Information

Name:	Dongxia Wei
Affiliation:	Individual
Email Id:	wdx@udel.edu
Country:	United States

Reports on Progress in Physics

Billing Status: **N/A**

Order detail ID: 71993163
ISSN: 0034-4885
Publication Type: Journal
Volume:
Issue:
Start page:
Publisher: IOP Publishing
Author/Editor: Institute of Physics Publishing ; et al

Permission Status: Granted
Permission type: Republish or display content
Type of use: Thesis/Dissertation
Order License Id: 4656541440852

Hide details

Requestor type	Academic institution
Format	Print, Electronic
Portion	chart/graph/table/figure
Number of charts/graphs/tables/figures	1
The requesting person/organization	Dongxia Wei
Title or numeric reference of the portion(s)	Figure 2
Title of the article or chapter the portion is from	Strong coupling between surface plasmon polaritons and emitters: a review
Editor of portion(s)	N/A
Author of portion(s)	N/A
Volume of serial or monograph	N/A
Page range of portion	page 3
Publication date of portion	23 December 2014
Rights for	Main product
Duration of use	Life of current edition
Creation of copies for the disabled	no
With minor editing privileges	no
For distribution to	Worldwide
In the following language(s)	Original language of publication
With incidental promotional use	no
Lifetime unit quantity of new product	Up to 999
Title	Semiconductor Hyperbolic Metamaterials for the Infrared
Institution name	University of Delaware
Expected presentation date	Sep 2019

Permission for Figure 6.4

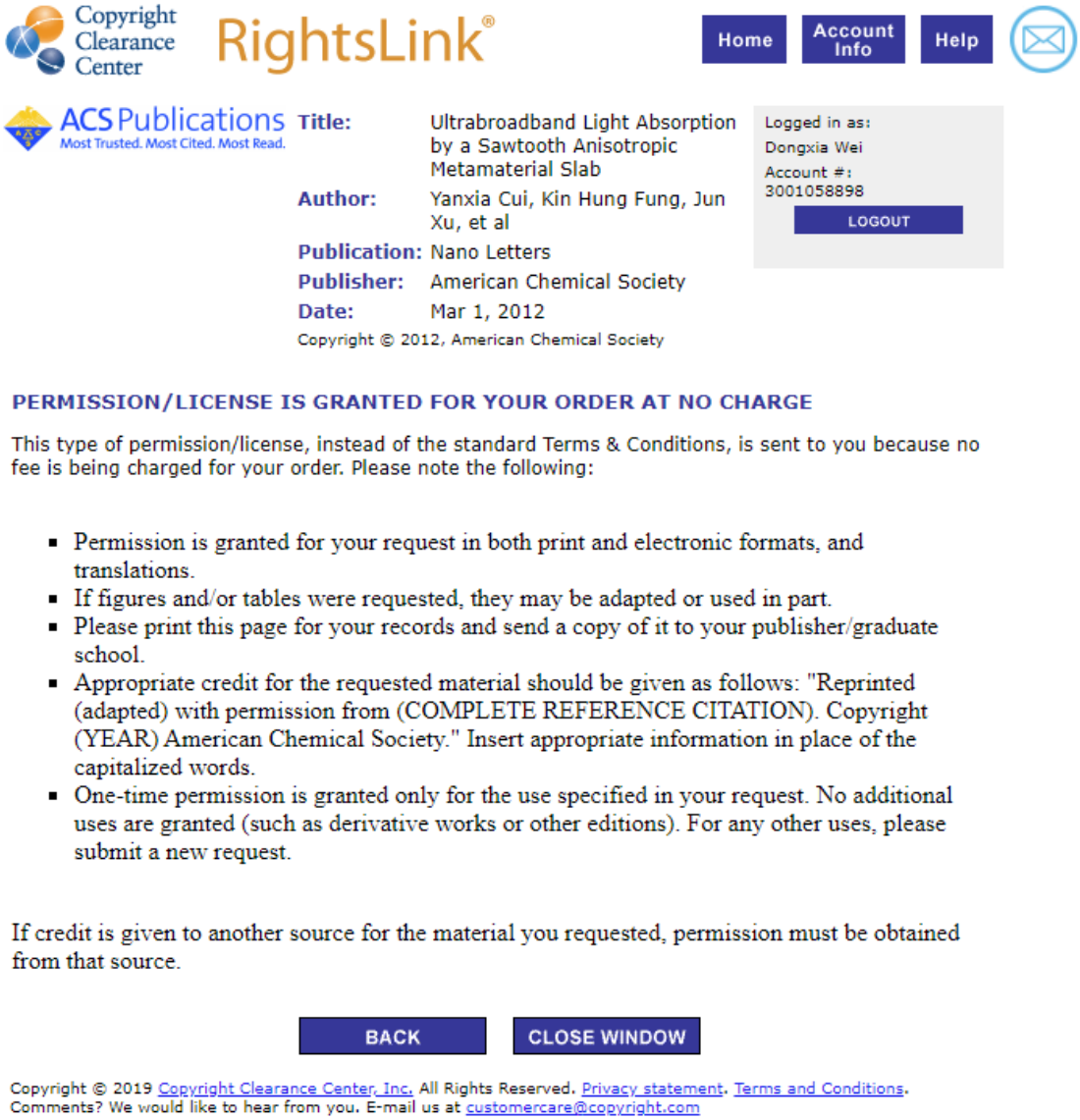

Copyright Clearance Center RightsLink®

Home | Account Info | Help

ACS Publications
Most Trusted. Most Cited. Most Read.

Title: Ultrabroadband Light Absorption by a Sawtooth Anisotropic Metamaterial Slab
Author: Yanxia Cui, Kin Hung Fung, Jun Xu, et al
Publication: Nano Letters
Publisher: American Chemical Society
Date: Mar 1, 2012
Copyright © 2012, American Chemical Society

Logged in as:
Dongxia Wei
Account #:
3001058898
LOGOUT

PERMISSION/LICENSE IS GRANTED FOR YOUR ORDER AT NO CHARGE

This type of permission/license, instead of the standard Terms & Conditions, is sent to you because no fee is being charged for your order. Please note the following:

- Permission is granted for your request in both print and electronic formats, and translations.
- If figures and/or tables were requested, they may be adapted or used in part.
- Please print this page for your records and send a copy of it to your publisher/graduate school.
- Appropriate credit for the requested material should be given as follows: "Reprinted (adapted) with permission from (COMPLETE REFERENCE CITATION). Copyright (YEAR) American Chemical Society." Insert appropriate information in place of the capitalized words.
- One-time permission is granted only for the use specified in your request. No additional uses are granted (such as derivative works or other editions). For any other uses, please submit a new request.

If credit is given to another source for the material you requested, permission must be obtained from that source.

BACK | CLOSE WINDOW

Copyright © 2019 Copyright Clearance Center, Inc. All Rights Reserved. Privacy statement. Terms and Conditions.
Comments? We would like to hear from you. E-mail us at customercare@copyright.com